AD-A183 213 USE OF LANDSAT DIGITAL DATA FOR SNOW COVER MAPPING IN THE UPPER SAINT JOH.. (U) COLD REGIONS RESEARCH AND ENGINEERING LAB HANOVER NH C J MERRY ET AL. JUN 87 1/1

UNCLASSIFIED CRREL-87-8 F/G 8/12 NL

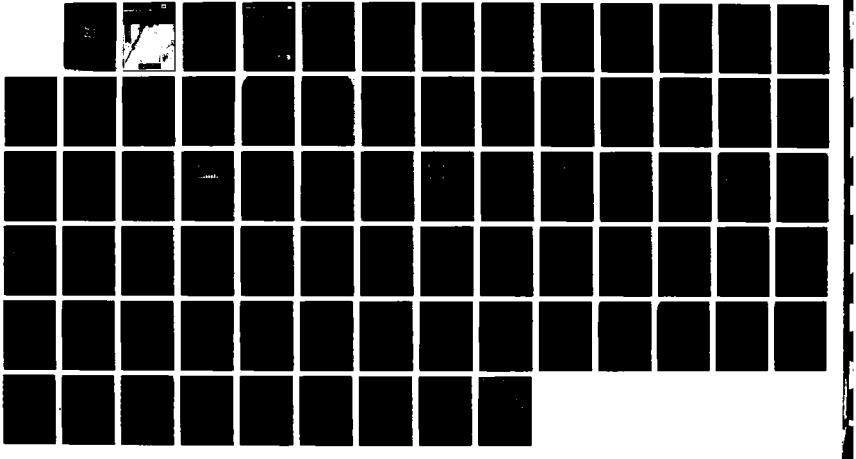

1.0
2.8
3.2
3.6
4.0
2.2
2.0
1.8
1.1
1.25
1.4
1.6

# CRREL
# REPORT 87-8



US Army Corps of Engineers
Cold Regions Research & Engineering Laboratory

# *Use of Landsat digital data for snow cover mapping in the Upper Saint John River Basin, Maine*

*For conversion of SI metric units to U.S./British customary units of measurement consult ASTM Standard E380,* Metric Practice Guide, *published by the American Society for Testing and Materials, 1916 Race St., Philadelphia, Pa. 19103.*

*Cover: Landsat MSS image (scene ID E-30672-14443-5) acquired during the 1979–80 season for the Upper St. John River Basin.*

# CRREL Report 87-8

June 1987

# *Use of Landsat digital data for snow cover mapping in the Upper Saint John River Basin, Maine*

Carolyn J. Merry and Michael S. Miller



Prepared for
OFFICE OF THE CHIEF OF ENGINEERS

| 6a. NAME OF PERFORMING ORGANIZATION | 6b. OFFICE SYMBOL (If applicable) | 7a. NAME OF MONITORING ORGANIZATION |
|---|---|---|
| U.S. Army Cold Regions Research and Engineering Laboratory | CRREL | Office of the Chief of Engineers |

| 6c. ADDRESS (City, State, and ZIP Code) | 7b. ADDRESS (City, State, and ZIP Code) |
|---|---|
| Hanover, New Hampshire 03755-1290 | Washington, D.C. 20314-1000 |

| 8a. NAME OF FUNDING/SPONSORING ORGANIZATION | 8b. OFFICE SYMBOL (If applicable) | 9. PROCUREMENT INSTRUMENT IDENTIFICATION NUMBER |
|---|---|---|
| | | |

| 8c. ADDRESS (City, State, and ZIP Code) | 10. SOURCE OF FUNDING NUMBERS | | | |
|---|---|---|---|---|
| | PROGRAM ELEMENT NO. | PROJECT NO. | TASK NO. | WORK UNIT ACCESSION NO |
| | | | | CWIS 31584 |

11. TITLE (Include Security Classification)

Use of Landsat Digital Data for Snow Cover Mapping in the Upper Saint John River Basin, Maine

12. PERSONAL AUTHOR(S)

Merry, Carolyn J. and Miller, Michael S.

| 13a. TYPE OF REPORT | 13b. TIME COVERED FROM _____ TO _____ | 14. DATE OF REPORT (Year, Month, Day) | 15. PAGE COUNT |
|---|---|---|---|
| | | June 1987 | 74 |

16. SUPPLEMENTARY NOTATION

| 17. COSATI CODES | | |
|---|---|---|
| FIELD | GROUP | SUB-GROUP |
| | | |
| | | |

18. SUBJECT TERMS (Continue on reverse if necessary and identify by block number)

| | |
|---|---|
| Hydrologic modeling | Runoff |
| Landsat | Snow cover |
| Remote sensing | Snow water equivalent |

19. ABSTRACT (Continue on reverse if necessary and identify by block number)

Measurements of snow depth and its water equivalent were obtained at 11 snow courses in the Allagash, Maine, area in conjunction with the acquisition of five Landsat-2 and -3 images during the 1977–78 and 1978–79 winters. To test a hypothesis that Landsat reflected radiance values on a regional scale do change, histograms of the Landsat MSS band 7 reflected radiance values for a 300- x 300-pixel (420 km$^2$) area near Allagash were evaluated to quantify the change. A statistical description (skewness and kurtosis) of the histogram for each scene was developed and then correlated with ground measurements of snow depth. A snow index based on skewness and modal population was found to correlate well with snow depth. Following these initial results, the Landsat data were re-examined and corrections were made for solar elevation and MSS sensor calibration. The reflected radiance from open areas showed a consistent increase in intensity with increasing snow depth. The forested land cover classes did not change with snow depth. Digital imagery data acquired on 31 May 1978 when the land was snow-free was used to classify land cover categories. Ground truth measurements of water equivalent of the snow cover were area-weighted using the land cover classification to derive regional values on each of the five Landsat winter scenes. The

| 20. DISTRIBUTION/AVAILABILITY OF ABSTRACT | 21. ABSTRACT SECURITY CLASSIFICATION |
|---|---|
| ☒ UNCLASSIFIED/UNLIMITED ☐ SAME AS RPT ☐ DTIC USERS | Unclassified |

| 22a. NAME OF RESPONSIBLE INDIVIDUAL | 22b TELEPHONE (Include Area Code) | 22c OFFICE SYMBOL |
|---|---|---|
| Merry, Carolyn J. | 603-646-4100 | CRREL-RE |

19. Abstract (cont'd)

1 March 1978 snow measurement of 19.46 cm of water equivalent was used as an input value to the SSARR model. The SSARR prediction for the 1 March–31 May 1978 ~~time~~ period was within 78% of the measured runoff for the initial baseflow period and within 66% measured for the spring melt recession period. However, the timing of six observed runoff peaks was off by 2 to 9 days. The magnitude of five of the predicted runoff peaks was within 75% of the recorded streamflow. Additional work on calibrating the basin peak timing and melt rate factors is required.

Keywords: Hydrologic modeling.

## PREFACE

This report was prepared by Carolyn J. Merry, Research Physical Scientist, Geological Sciences Branch, Research Division, U.S. Army Cold Regions Research and Engineering Laboratory, and Michael S. Miller, M/A-COM Sigma Data Inc., Goddard Institute for Space Studies.

The study was sponsored under the Corps of Engineers Civil Works Remote Sensing Research Program, CWIS 31584, *Snow Cover Analysis Using Landsat Digital Data.*

The authors express their appreciation to Dr. Harlan L. McKim for his support and helpful technical discussions on the project; to Saul Cooper (formerly Chief, Water Control Branch, U.S. Army Engineer Division–New England) and Dr. Jerry Brown for their support throughout the project; to Roy Bates (CRREL), to Mary-Lynn Brown (CRREL) and Lenora Wong (formerly with U.S. Air Force Academy) for assistance in reduction of the meteorological and snow course data; to Judy Karen (formerly with Dartmouth College) and Nancy H. Humiston (CRREL) for computer input of certain data files; to Roy Gardner for his invaluable assistance in making the snow courses in conjunction with the Landsat satellite overpasses; to Roy Bates and Harold O'Brien (CRREL) for their assistance in selecting the snow course sites and for technical review of this report; to Gary DeCoff (CRREL) and Jeffrey W. Doyle (Dartmouth College) for their work in adapting the SSARR model to run on a PRIME 400 computer; to Timothy Pangburn for his technical assistance when running the SSARR model; to Lawrence W. Gatto and Richard K. Haugen for technical review of earlier results from this project; and to Dr. Stephen G. Ungar (NASA GISS) and the GISS programming staff for development of the Landsat computer algorithms used in the analysis of the Landsat digital data.

## CONTENTS



## ILLUSTRATIONS

Figure

## TABLES

# Use of Landsat Digital Data for Snow Cover Mapping in the Upper Saint John River Basin, Maine

CAROLYN J. MERRY AND MICHAEL S. MILLER

## INTRODUCTION

The U.S. Army Cold Regions Research and Engineering Laboratory (CRREL), along with the U.S. Army Engineer Division, New England (NED), have been involved in the Landsat data collection system and Landsat imagery analysis since the launch of ERTS-1, now known as Landsat-1, in July 1972 (Cooper et al. 1975). During the Landsat-1 experiment, CRREL participated in the data collection system studies by developing sensor interfaces for the Landsat data collection platforms (DCPs) and evaluating the system performance of various DCP installations. During the Landsat-2 program (1975–77), CRREL was involved in the digital processing of the Landsat computer-compatible tapes (CCTs) and in DCP sensor and software interface development. The hydrologic parameters selected for Landsat digital analysis were snow cover and delineation of wetlands and flooded areas (Merry and McKim 1978). This report summarizes the continuation of the Landsat program, with funding from the Office of the Chief of Engineers, from the winter of 1977–78 through the 1979–80 winter season.

Each spring the SSARR (Streamflow Synthesis and Reservoir Regulation) model is used to forecast snowmelt and precipitation runoff in the Upper Saint John River Basin in northern Maine. There are two ways to input snow to the SSARR model: one is to input the percentage of the watershed area covered by snow, and the second is to input a basinwide average value of water equivalent. However, present methods of using point snow course measurements to calculate a basinwide mean snow-water equivalent value can provide erroneous data because of nonrepresentative snow courses and inappropriate extrapolation methods. Because of the remoteness of the area, it would be very costly to establish a data collection network for evaluating the water equivalent of the snowpack each year. However, estimates of the amount of water available in the snowpack are required for flood control during spring runoff.

There were two objectives for this study. The first objective was to analyze the Landsat digital data to determine if there is a correlation between snow depth and the measured intensities in the four spectral bands. The second objective was to determine how satellite multispectral data can be used in the SSARR model. The areal distribution of mapped land cover categories was area-weighted using snow course measurements that allowed a basinwide value of water equivalent to be calculated for each land-cover category. This estimate of snow-cover water equivalent was input to the SSARR model and compared to recorded stream flow measurements.

## BACKGROUND

### Literature review for remote sensing of snow cover

Barry (1983) conducted a survey of recent advances in selected areas of snow and ice research from 1979 to 1982. Results obtained by new measurement techniques and the application of remote sensing methods were described.

Manual methods have been used to delineate the areal extent of snow and the mean altitude of the snowline from Landsat Multispectral Scanner Subsystem (MSS) photographic data products (Meier 1973, 1975a; Barnes and Bowley 1974; Rasmussen and Ffolliott 1979, Bowley et al. 1981). The Landsat MSS imagery is available for a

185-km square area in four spectral regions (two visible bands of 0.5–0.6 μm and 0.6–0.7 μm, and two near-infrared bands of 0.7–0.8 μm and 0.8–1.1 μm). Attempts were made to estimate the snow depth from Landsat MSS visible band imagery. Snow depths of 2.5 cm or more can be mapped reliably: it was found that the brightness level increases with an increase of the snow thickness to 15 cm (Barnes and Bowley 1974). Beyond this snow depth, however, changes in brightness do not normally occur. The snow line can be mapped to an accuracy of 20 km. A set of techniques for satellite snow mapping are covered in Barnes and Bowley (1974).

Three regions were isolated on the TIROS (Television Infrared Observation Satellite) ESSA (Environmental Sciences Services Administration) and Soviet Meteor-10 system satellite imagery. They included: 1) a snow depth of less than 2.5 cm, 2) snow depth from 2.5 to 10.2 cm, and 3) snow depth greater than 10.2 cm (Kurilova 1975, Kurilova et al. 1976). Snow depths greater than 10.2 cm were approximated only when climatic information on snow depth and weather conditions was available. The Meteor-10 satellite data are somewhat limited because of the low spatial resolution (1.25 km) of the photographs used in Kurilova's studies.

Percent snow-covered area maps of water basins in the southwestern U.S., the Sierra Nevada in California, the Pacific Northwest, and the northeastern U.S. are prepared weekly by NOAA/NESS (National Oceanic and Atmospheric Administration/National Environmental Satellite Service) starting on 1 November and ending when the snowpack is depleted (McGinnis et al. 1979). Since the 1977–78 winter season, operational coverage has been maintained for 30 basins, with the data supplied within 30 hr of a satellite overpass. The satellite images used for the snow mapping are from the VHRR (Very High Resolution Radiometer) sensor on the NOAA satellite and the VISSR (Visible and Infrared Spin-Scan Radiometer) on GOES (Geostationary Operational Environmental Satellite). The VHRR provides daily coverage over the U.S. in the visible wavelengths (0.6–0.7 μm) and twice-daily coverage in the thermal infrared wavelength (10.5–12.5 μm) band at a spatial resolution of 1 km for 256 energy levels. The VISSR imagery is available approximately every half hour over the United States at several resolutions in the visible and thermal infrared regions. The best resolution is 0.8 km for the visible band and 8 km for the thermal band. The 1-km resolution available with the VHRR permits positioning of the snow limit to within 10 km (McGinnis 1975). Snow depth estimates have been found to correlate well with snow brightness for snow depth measurements less than 25 cm, although there is insufficient ground snow depth observations to conclude that satellite brightness values are a reliable indicator of snow depth (McGinnis 1975).

McGinnis (1975) examined a single NOAA-2 VHRR visible wavelength image over the southeast U.S. following a major snow storm. The satellite data was gridded into 32- × 32-pixel areas, corresponding to 1024 sq km on the ground. The greatest snow depth within each cell, as reported in the Department of Commerce climatological summaries, was paired with the highest brightness value. A power curve was found to describe the resulting plot. Small increases in depth caused brightness increases much larger than comparable increases at higher depths. McGinnis (1975) found that "once the snow accumulates to about 25 cm, most small plants are covered, only the larger shrubs and plants (corn stalks to trees) remain visible and in most cases will remain uncovered except in some mountainous areas where extremely heavy snows occur."

Matson and Wiesnet (1981) developed a monitoring program for the routine global mapping of snow cover using visible-channel imagery from the NOAA satellites. The interannual variability of regional snow cover can be described.

Lillesand et al. (1982) evaluated digital GOES visible data for four snow-covered days in Minnesota. Brightness values were compared against 13 rural nonforested sites located near National Weather Service snow depth measurement sites. Linear and second-order regression fits for the individual days resulted in variable $R^2$ results. Similar analysis for forested sites was not reported. They did find that subtraction of non-snow brightness values for an October image from the snow image brightness values might have value in digitally determining the presence of snow in forested regions.

Imagery from the ESSA-9 camera system operating in the visible wavelengths was used to interpret snow conditions in the Quebec–Labrador region (Parry and Grey 1975). The imagery has a spatial resolution of approximately 5 km and a relative brightness scale of 64 levels. It was found that terrain factors, in particular the vegetation type, had a significant effect on the reflection values and, under similar snow conditions, physio-

graphic regions of the same type exhibit comparable brightness values.

A series of five-day composite minimum brightness (CMB) charts were used in the analysis. Reflection values were measured on a scale of 0–10% reflection when using a Densichron densitometer. A frequency–density analysis of the histograms of reflection values was used to see if regional snow conditions could be determined. "A distribution with high values and a moderate right skew represents a fresh snowfall over the greater part of the area, whereas a bimodal distribution indicates that the snowfall was restricted to particular parts of the region. With the same range of values and a left skew, the snow conditions can be interpreted as intermediate, which suggests settling, redistribution, ageing and compaction. A strongly unimodal, left-skew distribution indicates that the melt stage had been reached, and the subsequent shift of the modal class toward lower values reflects the progressive expansion of the snowfree areas" (Parry and Grey 1975).

There was a general consistency in the relative brightness of individual vegetation zones (in the range and the mean of each group) at all stages of the snow cover with the exception of the final melt period. The differences between the vegetation zones were particularly noticeable after periods of extensive snowfall.

The High Resolution Infrared Radiometer (HRIR) provides for 24-hr mapping of the Earth at an 8.5-km resolution. Nighttime infrared measurements of the Earth's surface and cloud top temperatures are provided in the 3.6- to 4.2-$\mu$m wavelength range; during the daytime the HRIR measures reflected shortwave radiation in the 0.7-to 1.3-$\mu$m range. The Image Dissector Camera System (IDCS) provides television coverage in the 0.5- to 0.7-$\mu$m range at a 4.1-km resolution. Imagery from these two sensor systems was acquired over the Lake Winnipeg and the Sierra Nevada areas. It was found that "use of the near infrared data in combination with the visible imagery appears to permit the detection of thawing snow" (Strong et al. 1971). An explanation for the near-infrared brightness reversal was that "surface melting of the lake or snowpack caused the surface to absorb in the infrared while still reflecting in the visible" (Strong et al. 1971).

Melting snow could also be distinguished from snow that had not reached melting temperatures by using the visible and near-infrared bands of the Landsat MSS (Golding 1974). "Under clear skies, fresh or dry snow has a reflectivity of about 90% in the visible part of the spectrum, and just slightly less in the near infrared. Such snow, therefore, appears light toned on both visible and near-infrared imagery. The surface of melting snow is covered by a thin film of water that absorbs most of the infrared radiation and therefore melting snow appears dark on the infrared imagery" (Golding 1974). However, ice is quite absorptive also. Old or refrozen snow would probably appear dark-toned in the near infrared region, too.

The Nimbus-7 satellite, launched on 24 October 1978, carries a multifrequency, dual-polarized microwave imager called the Scanning Multichannel Microwave Radiometer (SMMR). The goal of Kunzi et al. (1982) was "to show that the three snow-cover parameters: extent, snow water equivalent, and onset of snow melt can be determined using scanning multichannel microwave radiometer (SMMR) data... . Snow extent is determined for dry snow cover with depth $\geq$ 5 cm, snow water equivalent can be determined on a regional basis with $\approx$ 2 g/cm$^2$ rms accuracy, and the onset of snow melt is clearly visible by the detection of melt and refreeze cycles prior to snow runoff" (Kunzi et al. 1982). However, the main limitation of the satellite passive microwave data is the coarse spatial resolution, varying from 30 to 60 km depending on the frequency range (18–37 GHz). Kunzi et al. (1982) distinguished three classes of snow with the SMMR data, including 1) no snow, 2) dry snow, and 3) snow undergoing melt and refreeze cycles. Two algorithms were developed to determine snow depth and snow water equivalent to an accuracy of 6 cm for snow depth and 2 g/cm$^2$ for snow water equivalent based on the climatic regimes of Finland, southern Russia, and Canada (Kunzi et al. 1982).

"Microwave instruments, such as the SMMR, are the only remote sensors providing subsurface snow data. ...The SMMR is a very promising sensor for the detection of the onset of snow melt. This information is of great interest in snow hydrology and meteorology, it allows estimation of the time of runoff from a basin, and combined with the snow water equivalent information, allows prediction of the total water runoff" (Kunzi et al. 1982).

Landsat MSS (Multispectral Scanner Subsystem) band 5 (0.6–0.7 $\mu$m) has been the most useful for detecting and mapping mountain snow cover (Barnes and Bowley 1973). Changes in snowline elevation on two different dates ranging from 60 to 1220 m were mapped from the satellite imagery. The snow observed in MSS band 7 (0.8–1.1 $\mu$m)

would normally be a high-elevation dry snow, whereas the dry and lower-elevation wet snow surfaces are seen in the MSS band 5 imagery (Barnes and Bowley 1974).

Barnes and Bowley (1974) discuss the problems of using satellite data to map snow. One problem is cloud cover obscuration for the visible and infrared systems. Passive and active microwave sensor systems may be a means to overcome this. Interpretation of the satellite data is another problem and includes distinguishing between snow and clouds, identifying snow in densely forested areas and in areas within mountain shadows, distinguishing between snow and highly reflective rock types, and mapping irregular, gatchy snowlines.

Landsat digital data for an alpine basin in Switzerland were classified, using a supervised parallelepiped discriminant classifier, into three classes: 1) terrain totally covered by snow, 2) the transition zone—a mixture of melting snow patches and snowfree parts, and 3) snowfree terrain (Lichtenegger et al. 1981). In high mountainous areas, climatic changes with elevation play an important role in snowmelt. The alpine basin was separated into three elevation zones of 500 m intervals and then digitized. The areal extent of snow cover was calculated in terms of percentage for each elevation zone and used as input to a runoff model.

In another test site, located in the Upper Rhine, Lichtenegger et al. (1981) used the elevation data that was registered to a Landsat image to generate four additional channels that included an elevation zone, exposure angle, slope angle, and a lambertian brightness or reflectance map. During the classification process, the shadowed area could be detected and radiometric corrections with respect to the incident radiation angle could be carried out. It then becomes possible to extrapolate the snow coverage within a climatologically similar region when clouds are encountered on Landsat imagery.

A digital terrain model (DTM) was matched with two Landsat MSS scenes for a 1500-km$^2$ catchment area in eastern Switzerland (Seidel et al. 1983). A snow signature was developed from a scattergram of Landsat MSS band 5 versus 7 for mapping snow and snow-free areas. The DTM data were used to map the snow-cover distribution in percent with respect to slope and aspect for a given elevation zone. This provides a promising tool to extrapolate the snow cover from a cloud-free area to other parts of the subbasin that may be cloud-covered.

A quantitative measure of the water equivalent of the snowpack has not been obtained from Landsat photographic data products. Normally Landsat data has been used in a number of snowmelt runoff studies, principally to map the areal extent of snow for use in predicting snowmelt-derived streamflow (Anderson et al. 1974; Meier 1975c; Rango 1975, 1978, 1981; Rango et al. 1975; Thompson 1975; Rango and Itten 1976; Rango and Salomonson 1976; Shunying et al. 1980; Shafer et al. 1981; Dey et al. 1983). For example, Landsat satellite data have been used to monitor the disappearance of the snow cover throughout the melting period (Rango 1980a, b; Martinec and Rango 1981; Rango and Martinec 1981; Martinec 1982). Martinec (1975) developed a simple rainfall runoff model that incorporates the snowmelt runoff portion. The model takes into account the variability of the degree-day factor, discharge recession coefficients, and the areal extent of snow. The depletion curves relating the areal extent of snow cover to elapsed time were modified to relate snow coverage to accumulated temperature thawing degree-days. The total discharge volume from a drainage basin during the snowmelt season was simulated by using these depletion curves of the snow coverage (Rango and Martinec 1979; Rango 1980a,b, 1983). Rango and Martinec (1982) suggested that the depletion curves that normally relate the areal extent of the snow cover to elapsed time be modified to relate the snow coverage to the accumulated thawing degree-days to forecast runoff. It was then possible to estimate the total snow accumulation of the basin compared to previous years by observing the course of the modified depletion curve during the first few weeks of the snowmelt season. The water equivalent of the snow at the beginning of snowmelt was estimated, and an appropriate modified depletion curve was selected to use in the snowmelt runoff model (Rango and Martinec 1982, Rango 1983). Precipitation and air temperature are other input data required in the model. (The effect of solar radiation is automatically included in the degree-day factor in Martinec's model.) When the first satellite images are available for analysis, the results from the runoff model can be compared with the initial modified snow cover depletion curves. An updated, modified depletion curve can be prepared that will more closely match the actual mapped snow cover to be used in runoff forecasting. A more detailed description of the model can be found in Martinec et al. (1983).

The Applications Systems Verification and Transfer (ASVT) program for using operational applications of satellite snow-cover observations was conducted over four sites in the western United States from 1976 to 1978. Based upon the Colorado ASVT operational forecasting experience, a projected 6–10% relative improvement in forecasting occurred, with a benefit-to-cost ratio of 72:1, principally in the areas of hydroelectric energy and irrigation (Castruccio et al. 1981). Operational application of Landsat imagery was limited due to lack of data that was cloud-free and received in real time. The infrequency of Landsat coverage (every 18 days) magnified these problems.

Digital processing techniques have been used to map the areal extent of snow. Meier and Evans (1975) compared in a qualitative manner seven methods for estimating snow cover from Landsat imagery for several basins in Oregon and Washington. The seven methods were grouped into three categories: manual, interactive computer analysis, and digital pattern recognition techniques. The precision of the digital pattern recognition technique on a pixel-by-pixel analysis was found to be excellent, but at high cost and with slow to average speed. The analysis normally produces supplemental data. The technique is good for recognizing snow in trees or in shadow. The satellite images can be used to determine the mean altitude of the snow line or the percent of snow-covered area as a function of altitude (Meier 1975a). In addition, the calculated areal extent of snow has been found to be in good agreement with data on snow-covered areas from satellite images. Snow-covered area from Landsat images is obtained by radiance slicing (selecting the appropriate shade of gray to define the snow/no snow boundary), radiance-gradient slicing, time-lapse comparison (for instance, comparing portions of the same image in a snow-free and snow-covered condition, or successive snow-covered images), and by multispectral analysis (Meier and Evans 1975). The Landsat data offers additional advantages of high resolution, accurate map projection, and multispectral data allowing use of pattern recognition techniques (Meier 1974, 1975a).

Landsat data were found to be unsuitable for mapping the snowline in rolling forested terrain (Langham and Power 1977). Electronic density slicing techniques were performed on the satellite image. The resolution resulted in too great a sampling density in the transition regions since multiple minima were observed in the histograms. Langham and Power would prefer to use areally averaged radiances at a resolution similar to NOAA satellites (1 km). However, a multispectral or pattern recognition analysis may be used to detect areas that combine the signatures of forest and snow cover (Meier and Evans 1975).

Single-band radiance thresholding of Landsat MSS band 5 data was the principal technique used in determining snow coverage for three Columbia River subbasins (Wiegman et al. 1975). The technique was supplemented by an editing procedure that involved reference to hand-generated elevation contours. A thematic map showing snow cover was documented by: 1) photography, 2) a numerical pixel count representative of the total area of snow in the scene and within the basin boundary, and 3) an array of single-digit numbers depicting tenths of snow cover for 2.5-km$^2$ grid cells within the basin.

The changes in the areal extent of snow cover measured on Landsat imagery have been found to correlate with changes in water equivalent recorded by a snow pillow (Anderson et al. 1974). As the water equivalent of snow increased, the areal extent of snow observed for the Caribou–Poker Creek watershed also increased. Another Landsat manual interpretation method used a coded snow cover classification scheme to account for vegetation cover, density, aspect, elevation, and slope to map the extent of snow (Katibah 1975a, b). Sequential aerial photography, Landsat imagery, and ground data on elevation, slope, aspect, and vegetation type were used to develop a subjective image interpretation key for a study conducted in the Feather River Watershed in Northern California (Draeger and Lauer 1974; Katibah 1975a, b; Sharp and Thomas 1975). A rapid and relatively simple manual interpretation technique was used to estimate acreages and extent of snow cover on satellite imagery by comparing no-snow Landsat images with corresponding snow-covered Landsat images.

Dallam and Foster (1975) used a snow-free Landsat scene to map the cover types and to serve as a reference base. Snow-covered Landsat scenes were then registered to the base image, so that any given point could be referenced to a cover type. Training sites were chosen visually to represent different snow cover classes. A supervised classification was used to produce a map of snow distribution versus cover type. Alföldi (1976) also used these basic concepts in a digital classification of a snow-covered Landsat scene. An enhancement of

the Landsat scene and subsequent classification was accomplished. A histogram analysis was used to make relative judgments about the snow cover. Alföldi (1976) suggested a simple technique for monitoring the presence of snow by developing a library of reference histograms with known snow characteristics and comparing an unknown histogram to estimate a best match. Prerequisites include identical areal coverage, cloud-free test and reference images, and no major changes in the land use/vegetative cover of the area. Alföldi (1976) indicated that total pixel brightness assumed a greater degree of importance for snow mapping when compared to the techniques of level slicing and band ratioing for digital image analysis of snow. He also indicated that snow cover mapping should be done on the basis of environmental factors affecting snowmelt rather than an arbitrary spatial grid. Ground visibility of snow through foliage and elevation were two suggested parameters.

Average snowpack characteristics, as well as the variability of these characteristics, were found to relate mainly to vegetation cover (FitzGibbon and Dunne 1979). In many small- to medium-size drainage basins in lowland areas, average snowpack characteristics are uniform and are a product of the regional climate (FitzGibbon and Dunne 1979). They found that variation of snow-cover properties was due to small-scale terrain interactions, which include local topography and vegetation, and the processes of snow-cover formation. FitzGibbon and Dunne demonstrated that snow-cover properties in a small, lowland subarctic drainage basin may be characterized according to vegetation cover as it controls snow redistribution through drifting. It is important that the extent and nature of the snow cover during the snowmelt be known, since the extent of snow cover partially determines the production of meltwater and reserves of water held in the pack (FitzGibbon and Dunne 1979).

Thomsen and Striffler (1980) classified the fractional snow-covered area of a Landsat pixel by detecting changes (differences in radiance) between a snowfree scene and snow-covered Landsat scenes. The water equivalent of the snow cover was inferred from the classified Landsat image, taking pixel elevation, aspect, and the image acquisition date into consideration. A watershed information system was developed to include a snowmelt runoff simulation that uses a spatial data format to drive snowmelt and lateral flow models for routing snowmelt through the soil profile to the nearest channel.

Anderson and Pagenhart (1957) did a multiple regression analysis and found that elevation, solar energy, and vegetation were important parameters influencing snow accumulation. An extensive review of the effects of elevation, aspect, and forest canopy on snow was accomplished by Meiman (1970). He concluded that differences resulting from canopy influences tend to be smaller than those associated with elevation changes. On the other hand, Anderson (1969) concluded that storm characteristics explain the longest variation in snow accumulation. Patch (1981) found that forest cover type may have the widest application in the utility of forest parameters in determining snow accumulation. He indicated that the forest cover could be of primary importance, as it can be and is altered by man, affecting spatial snowpack patterns and ultimately water yield and regime.

A snow mapping experiment comparing the identification of six snow-cover types was accomplished using three image processing systems—LARSYS Version 3, STANSORT-2, and General Electric IMAGE-100 (Itten 1975). In addition, other studies have focused on digital analyses of Landsat data in defining various snow-cover types (Bartolucci et al. 1975, Dallam and Foster 1975, Luther et al. 1975, Alföldi 1976). In these studies a quantitative estimate of water equivalent content associated with snow-cover types was not made. In one case it was suggested that spectral variations within the snowpack area could not be reliably determined because of detector saturation problems (Bartolucci et al. 1975).

Saturation of the MSS detector proved a problem for a study conducted over the American River Basin in California (McMillan and McGinnis 1975). A multiple regression equation was developed to predict the average snowpack density using the variables of MSS 7 radiance values, solar declination, sum of average daily air temperature above freezing since snowfall (thawing degree days), and snow course elevation. The results were not totally acceptable for immediate use in the Sierra Nevada. The average snowpack density was estimated from in situ albedo measurements obtained with two pyrheliometers (0.3–4.0 $\mu$m) for given site and storm data (McMillan and Smith 1975).

Another study used simulated infrared Landsat color composites and snow course data to estimate water equivalent related to the snowpack (Sharp

1975). Sampling units on the Landsat image were mapped to determine the areal extent of snow. An estimation of a snow water equivalent index was calculated using a linear regression equation relating the imagery to ground truth data.

Several researchers have reported techniques for estimating snow depth with aerial surveys. Steinhoff and Barnes (1976) used aerial remote sensing to determine by photogrammetric means the snow depth over a limited number of ground control targets. First, they photogrammetrically determined the ground surface elevation from aerial photography before snowfall. Using photography after a snow event, comparable ground elevations were determined. The difference between the two elevations would give an estimate of the snow depth. Multiple regression equations were developed for a given area relating snow depth to elevation, aspect, degree of slope, melt date, and vegetation density at various times during the melt season. Ideally, once a regression equation was developed for an area, the snow depth and water equivalent could be predicted by measuring the melt date and environmental variables. However, a uniform prediction of snow depth for an entire watershed from a single point measurement was not possible.

Blyth et al. (1974) discussed a similar technique using terrestrial-based stereopairs for determining depth differences for pre- and post-snow dates. They found the estimates of depth to be within 10% of the actual for 3-hectare study sites.

Warskow et al. (1975) conducted aerial surveys over a western hydrologic basin. They made visual estimates of snow depth, using the interactions of snow cover and the surrounding features of the landscape. It was estimated that dark rocks would be obscured by snow depths of 0–15 cm; grass stems would no longer be visible when the depth reached 15–20 cm; and half-shrubs were used as indices for the range 15–30 cm. Logs, fences, or markers were required for estimating snow depths greater than 30 cm. It was found that estimates were accurate within ±5 cm, which was sufficient for their runoff volume forecasts.

Nicholson (1975) collected a temporal series of air photos to document the areal extent of snowpack duration throughout the melt season in a subarctic area of eastern Canada. Contours of duration, derived from the photographs, were related to maximum depth contours.

Ferguson and Lapczak (1977a,b) examined a portion of a NOAA-4 image over the Souris River basin in Saskatchewan, Manitoba, and North Dakota. They compared brightness values to ground measurements of snow depth. A good correlation was found between the two variables. They caution, however, that the region is mostly flat, grass-covered terrain. The relationship between depth and brightness, they conclude, would not be evident for complex forested landscapes.

Mellor (1965) stated that remote sensing of the snow cover may have useful applications since the magnitude and wavelength of reflectance vary with snow types. The albedo for a layer of new snow can be quite high, approaching 91%; as the new snow grains coalesce and coarsen in texture the albedo falls steadily towards levels of 60 to 70% (Bergen 1975). In addition, the spectral reflectance declines from the combination of densification and increased particle size associated with aging (O'Brien and Munis 1975).

The albedo of a snow surface varies depending on the state of the surface. Fresh, undisturbed snow commonly reflects more than 70% of incoming solar radiation (Kondratyev 1969, Budyko 1974). A typical curve of reflectance as a function of wavelength shows a uniform high value greater than 0.8 at wavelengths between 0.35 and 0.90 $\mu$m (Fig. 1). A marked drop in reflectance occurs in the near-infrared wavelengths, to a value less than 0.1, between 1.4 and 1.6 $\mu$m. High reflectance was found in the visible portion with a sharp decrease in reflectance between 0.7 to 1.5 $\mu$m (O'Brien and Munis 1975). This drop in near-infrared reflectance has been useful in discriminating snow surfaces from clouds in satellite imagery (Barnes and Smallwood 1975, Bartolucci et al. 1975).

Several aging processes decrease the reflectivity of a snow surface. Drifting, compaction, melt/freeze cycles, and micro-structure are so interrelated as to make it difficult to assess the precise role of each in changing reflectivity (O'Brien and Munis 1975). They also report that for a snowpack that had been naturally aged for about 40 hours, a ratio of about 0.8 spectral reflectance occurred for fresh to aged snow over the visible and near-infrared portions of the spectrum. This was for a specific case, so different natural aging conditions could result in different findings (H.W. O'Brien, pers. comm., 1984).

Using in situ measurements, McMillan and Smith (1975) found the square of albedo to be a good predictor of the average snowpack density. Bergen (1975) found that for snow grains greater than 1.5 mm in diameter, albedo variations are

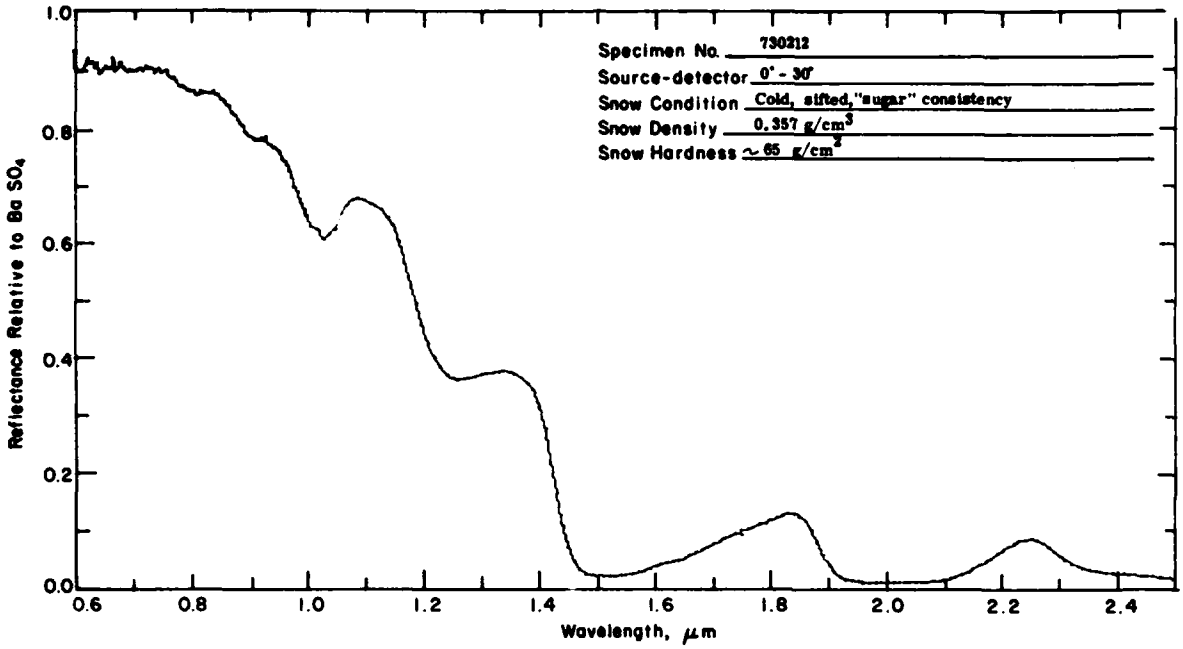


*Figure 1. Typical spectral reflectance curve for snow (after O'Brien and Munis 1975).*

primarily associated with density rather than grain size. In contrast, Bohren and Beschte (1979) reported no statistically significant change in albedo following artificial compaction by a snowmobile.

For shallow snow cover, the reflective properties of the underlying surfaces affect the surface albedo. Multiple reflections within the snow allow penetration of solar radiation to shallow depths. Giddings and La Chapelle (1961) show the extinction coefficient of snow to be a function of depth. With an underlying black surface, they showed albedo to increase rapidly with increasing depth, leveling off sharply as depth increased beyond 20 cm. O'Neill and Gray (1973) showed virtual independence of albedo from snow depth beyond depths of approximately 10 cm. Wiscombe and Warren (1980) indicated that the depth at which background influences occur depends on density and/or grain size.

These observations are based on measurements of surfaces composed of pure snow. It may be expected that the introduction of vegetation canopies would complicate the relationship of snow cover and albedo.

In natural landscapes, the reflectivity of an area during the winter will be determined by the unique properties of the surface components. "The regional albedo values during the winter months are dependent mainly on two factors, snow albedo and the darkness of the nearly black bodies (i.e., trees and buildings, etc.)" (Kung et al. 1964). Thus, the structure of the vegetation canopy greatly influences the overall reflectivity. In their airplane measurements of surface beam albedo over Wisconsin, Kung et al. (1964) found agricultural lands under deep snow cover displayed albedos in the range of 50 to 70%. "When the ground snow cover is rather shallow, i.e., the snow depth is less than 5 in., the value of surface albedo is apparently related to the depth of snow and in turn probably to the area of patches covered by the snow, though further accumulation of snow does not seem obviously to increase the albedo" (Kung et al. 1964). Forested areas with deep snow reflected between 20 and 50% of the incoming solar radiation. Species composition of the forest accounted for considerable variability, for example, aspen and birch forests had albedos ranging from 38 to 50%; pine forests ranged from 19 to 37%; oak 32 to 42%; northern hardwood 19 to 36%; and swamp conifer 25 to 38%.

McFadden and Ragotzkie (1967) presented hemispheric albedo data for a variety of snow-covered regions observed with hemispheric solarimeters in flights over the boreal region of central Canada. Snow-covered tundra areas with frozen lakes had albedos in the range 70 to 92%, while forested lands with frozen lakes were in the range

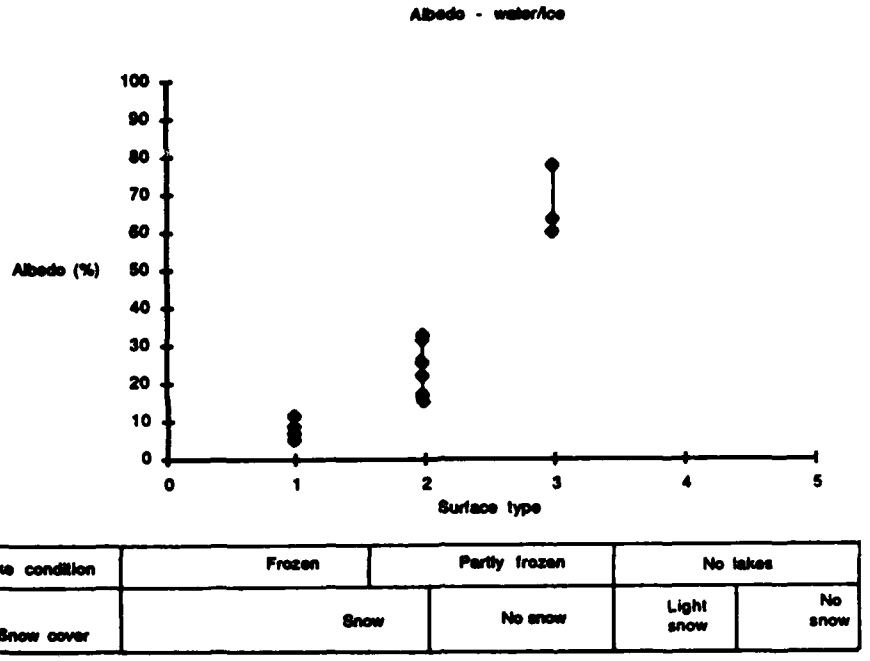


*Figure 2. Albedo ranges for tundra and boreal forest regions (after McFadden and Ragotzkie 1967).*

30 to 68% (Fig. 2). With lakes only partly frozen, snow-covered forests had albedos of 23 to 55%. It was found that the presence of frozen lakes raises regional albedos by a factor of at least 2 above that of forests without lakes. Additional albedo data for other regions are shown in Figure 3 for selected conditions ranging from water to ice- and snow-covered lakes. The more snow and ice cover on a lake, the higher the albedo.

The mechanics of obtaining hemispheric and beam albedo are different. "Beam albedo is calculated from the output of an upward-facing hemisphere radiometer and a radiometer with a downward-facing parabolic mirror that intercepts energy from a small area with a 4° beam width and focuses this energy on the radiometer. Hemispheric albedo, on the other hand, is determined from the records from the same type of upward-facing radiometer and down-facing solarimeter that has a full $2\pi$ steradian field of view. At an altitude of 500 ft the beam albedo system will instantaneously sample an area 35 ft in diameter, while the hemisphere system samples over the entire solid angle" (McFadden and Ragotzkie 1967). The values from the two different systems can be compared using a calibration factor of

(beam albedo × 1.294) = hemispheric albedo

that was developed by Bauer and Dutton (1962), Dutton (1962), Kung et al. (1964), and McFadden and Ragotzkie (1967).

Leonard and Eschner (1968) conducted albedo measurements over a red pine plantation in northern New York State. On the morning following a snowfall of approximately 300 mm (30 mm water equivalent), an estimated 100 mm (10 mm water equivalent) had been retained by the forest canopy. At this time, mean albedo as measured by a tramway elevated solarimeter was about 18%. As the day progressed, a progressive decline in albedo was observed. Increasing temperature caused the dropping of clumps of snow, as well as some melt dripping. Most of the forest canopy was snow-free by 1300 hr. Albedo fell to approximately 15% and stayed fairly constant throughout the day. The reflectivity and canopy conditions during the afternoon were similar to measurements obtained immediately after a rainstorm. Leonard and Eschner suggest a value of 20% be used for albedo of snow-covered coniferous forest, although this may be conservatively high.

Using paired silicon cells above hardwood forests, Federer (1971) measured albedo at three northern sites in New York State and New Hampshire. Without snow, the canopy albedo was found to be about 10%. With ground snow cover,

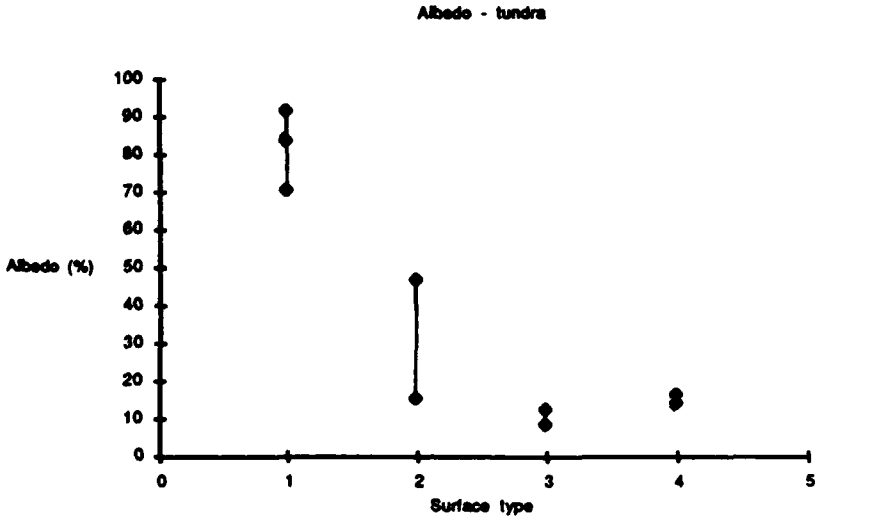


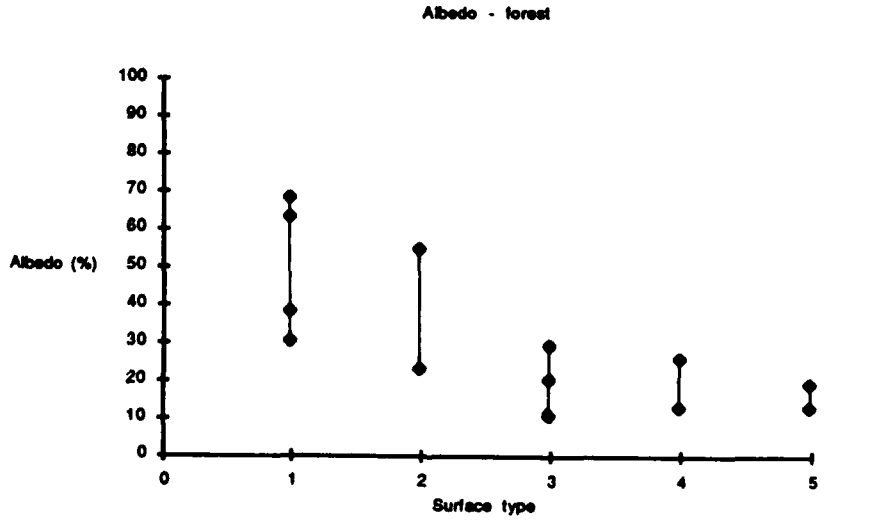


*Figure 3. Typical albedos for selected conditions ranging from water to ice- and snow-covered lakes (data from McFadden and Ragotzkie 1967).*

the albedo increased to values of 20% to 30% (Federer 1971).

Choudhury (1982) used Kung's aircraft albedo measurements (1964) to develop a model for the effective albedo of partially snow-covered areas. An equation for the fractional snow-covered area, dependent upon the snowpack thickness, was developed using Kung's data. These data were then compared to NOAA-2 VHRR data of McGinnis et al. (1975) for the southeastern United States. The predictions of the effective albedo model were in qualitative agreement with McGinnis's observations; for a given snow depth, the calculated brightness value was somewhat higher than the observed mean value (Choudhury 1982).

Spectral reflectance decreases with increasing particle size (Dunkle and Bevans 1956). Natural aging of the snow with normal settling and densification and th' metamorphism of the snow cover or refreezing of partially melted snow on the surface and within the snowpack also cause a decrease in reflectance (Dirmhirn and Eaton 1975, O'Brien and Munis 1975). Hoarfrost formation on the surface could also raise the reflectance (H.W. O'Brien, pers. comm., 1984). The albedo measurement of the snow cover changes with the varying contribution of specular reflection from the snow surface with solar angle (Dirmhirn and Eaton 1975).

The reflectance of fine-grained snow is not greatly dependent on wavelength in the visible region, since surface reflectivity is high and single backscattering from the first layer of grains is apparently not very selective with respect to wavelength (Mellor 1965). However, as grain size increases, reflectance and surface reflectivity decrease. A relatively large proportion of the reflected light is backscattered from beneath the surface so that reflectance becomes inversely dependent on wavelength (Mellor 1965). The magnitude and wavelength dependence of reflectance will vary with snow type (Mellor 1965). The reflectance of snow is determined by the illumination conditions, by the surface characteristics, and by the subsurface backscattering (Mellor 1977).

Warren (1982) reviewed the optical properties of snow in the solar ($0.3 \leq \lambda \leq 5$ $\mu$m) and thermal infrared ($5 \leq \lambda \leq 40$ $\mu$m) wavelength regions, which are important for determining the climatic role of snow and for affecting snowmelt. He states that the bidirectional reflectance distribution function, which is unevenly distributed among the reflection angles, must be known to interpret individual satellite measurements. The function has been measured at the snow surface and at the top of the atmosphere, but its dependence on wavelength, snow grain size, and surface roughness is unknown (Warren 1982). Warren recommends that angular detailed measurements of the bidirectional reflectance for various wavelengths, grain sizes, and surface conditions should be given a high priority for remote sensing applications.

> "Dozier et al. (1981) have used a model of Wiscombe and Warren (1980) to calculate snow albedos integrated over channels 1 and 2 (0.5–0.7 $\mu$m and 0.7–1.0 $\mu$m, respectively) of the NOAA TIROS-N satellite. The hope is to deduce grain size from a near-infrared channel, where depth and contaminants have no effect on albedo, and then use the deduced grain size together with the channel 1 data to infer snow water equivalent depth below some threshold value around 100 mm. Among the difficulties in this approach are (1) the conversion of bidirectional reflectance to albedo, (2) the poor location of channel 2 for this purpose (an ideal channel would be located in the region 1.0–1.2 $\mu$m, where the sensitivity of albedo to grain size is greatest), and (3) the fact that visible albedo reduction can be due to impurities as well as to thinning of the snowpack. Dozier et al. (1981) were apparently able to detect the thinning of the snowpack at the end of the melting season on some Canadian lakes" (Warren 1982).

Other research indicates that the 1.25- to 1.35-$\mu$m spectral region would be an even better choice due to the sensitivity of albedo to grain size (H.W. O'Brien, pers. comm., 1984).

O'Brien and Koh (1981) observed the change in spectral reflectance with a few narrow-band filters as a thick snow cover decayed. They documented in a qualitative manner the transition of the spectral reflectance of snow to the spectral reflectance of grass.

Several investigators reported that snow accumulation is unique for specific vegetative and landscape units (Steppuhn and Dyck 1974, Adams 1976, Steppuhn 1976, Adams and Barr 1979, Fitz-Gibbon and Dunne 1979, Mathers 1980, Adams and Roulet 1981). As discussed earlier, when considering an open, undisturbed snowpack, snow depths greater than about 13 cm will not display greater reflectivity with increasing accumulation. However, when the snow is found intermixed with a vegetation canopy, the interactions are more complex. It could be hypothesized that as the bright snow increases in depth, the darker extent

of the plant cover (both horizontal and vertical) becomes obscured. The reflectance might increase, ideally, until the uppermost crown of the vegetation is completely overlain by about 13 to 25 cm of snow (McGinnis et al. 1975).

Snow cover in different roughness zones shows systematic differences in snow water equivalent, average density, and depth (Granberg 1975). Average water equivalent was found to be largely independent of roughness zone, except for boundary zones (Granberg 1975). Surface roughness comprised topographic and vegetation roughness. The height-to-width ratio of topographic roughness is considerably less than unity, and vegetation roughness has a height-to-width ratio considerably greater than unity. The effect of roughness changes through winter has shown that snow accumulation results in a progressive reduction in surface roughness (Granberg 1972). Six roughness zones were selected in Granberg's study and included closed woodland, open woodland, regenerating burn, recent burn, bog, and lake.

Warren (1982) and NASA (1982) listed the snow parameters affecting the visible, near-infrared, thermal infrared, and microwave wavelength regions (Table 1). "To detect individual snow parameters unambiguously from satellite, one must *therefore examine the snow* at several wavelengths simultaneously. For remote sensing applications, angularly detailed measurements of the bidirectional reflectance for various wavelengths, grain sizes, and surface conditions should be given high priority" (Warren 1982).

**The Landsat CCTs**

The Landsat satellites (Landsat-1 through -4) circle the earth in a 920-km, near-polar orbit once every 103 minutes, each completing approximately 14 orbits per day. The multispectral scanner (MSS) on each satellite is a line-scanning device that uses an oscillating mirror to continuously scan perpendicular to the spacecraft (USGS and NASA 1979). Six lines are scanned simultaneously in each of four spectral bands for each mirror sweep, and radiation is sensed simultaneously by an array of six detectors in each of four spectral bands from 0.5 to 1.1 $\mu$m (USGS and NASA 1979). During image data processing, a black and white photographic data product can be produced of an area approximately 185 km on a side for the following spectral regions: MSS band 4 (0.5–0.6 $\mu$m), MSS band 5 (0.6–0.7 $\mu$m), MSS band 6 (0.7–0.8 $\mu$m) and MSS band 7 (0.8–1.1 $\mu$m). This information is also available in digital form on a CCT. Landsat data products can be obtained from the EROS Data Center, Sioux Falls, South Dakota.

The standard Landsat CCT was computer-processed to produce a geometrically corrected tape with the pixels transformed to a UTM (Universal Transverse Mercator) projection. This geometrically corrected CCT comprises 2432 scan lines, with each scan line covering 3200 pixels. Each pixel represents an area on the ground having dimensions of 61 × 76 m. Differing levels of radiant energy for each pixel within the scene are registered on a scale from 0 to 127 (minimum [black] to maximum [white]) for bands 4, 5, and 6 and 0 to 63 for band 7 (Thomas 1975).

**Table 1. Parameters affecting albedo and emissivity of snow (after Warren 1982 and NASA 1982).**

| *Snow property* | *Visible solar albedo* | *Thermal infrared emissivity* | *Microwave emissivity* |
|---|---|---|---|
| Grain (or crystal) size | Yes* | Yes | Yes |
| Zenith (or nadir) angle | Yes* | Yes | Yes |
| Snow depth | Yes† | | Yes |
| Contaminants | Yes | | |
| Liquid water content | Yes | Yes | Yes |
| Surface roughness | Yes | | Yes |
| Density | | | Yes |
| Temperature | | Yes | Yes |
| Stratification | | | Yes |
| Soil state, moisture, roughness, vegetation | | | Yes |

* If snowpack is thin or impurities are present.
† Shallow, up to a few centimeters.

Figure 4 shows the Landsat orbital tracks over northern New England. The ideal path and rows for Landsat coverage over the Upper Saint John River Basin were path 13, rows 27 and 28. However, side lap does occur with the adjacent paths of 12 and 14. Table 2 shows the available Landsat coverage over the Upper Saint John River Basin for the 1977–78, 1978–79, and 1979–80 winter seasons.

**The computer algorithm**

The geometric correction of the digital data and the computer classification algorithms used in the analyses were developed at the NASA Goddard Institute for Space Studies (GISS) (Ungar 1977). The geometric correction provides for a 1:24,000 scale computer print-out, which enables one to locate test sites more accurately. The classification algorithms used were part of the GISS-MAP1 (Multispectral Image Analysis Package) program. In this package, digital count values for the four Landsat MSS bands are converted to radiances (measured in mW $cm^{-2}/sr$) using calibration-derived gains and offsets. The MAP1 algorithm developed for analysis of the digital data allows for both components of the data—one of the four wavelength bands and the associated radiance value for each pixel—to be evaluated when classifying the Landsat data in various categories. Color differences consider the direction of the pixel vectors relative to the four-band axes. Brightness differences are based on the summation of the four bands.

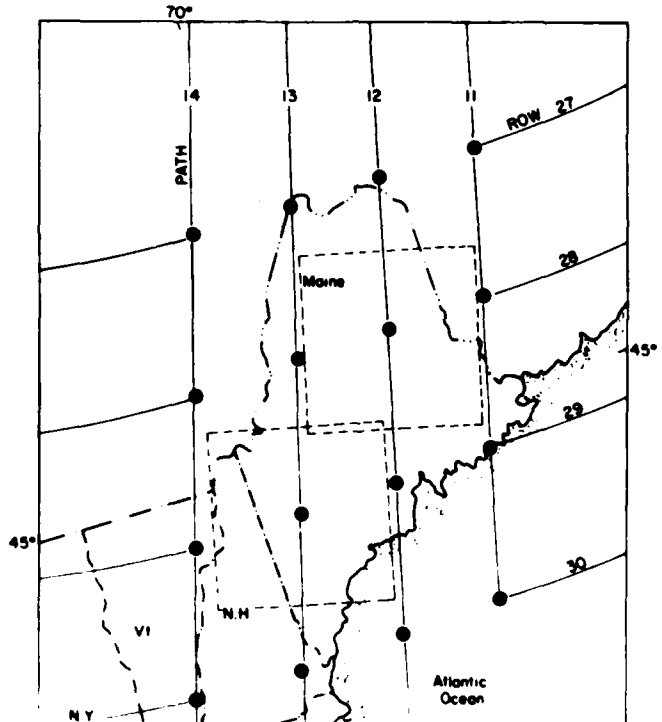


*Figure 4. Landsat orbital tracks over the northern Maine area. Image centers are indicated by the solid circles; the dashed outlines show ground coverage per frame and image overlap and sidelap.*

## Table 2. Landsat satellite overpasses for the Upper Saint John River Basin.

### a. 1977-78 winter season.

| Date | NASA scene ID | Path/row | Cloud (%) |
|---|---|---|---|
| 1 Dec 77 | 6044-14125 | 12/27 | 90 |
| 1 Dec 77 | 6044-14132 | 12/28 | 90 |
| 3 Dec 77 | 6046-14243 | 14/27 | 80 |
| 19 Dec 77 | 6062-14122* | 12/27 | 70 |
| 19 Dec 77 | 6062-14125* | 12/28 | 90 |
| 20 Dec 77 | 6063-14180* | 13/27 | 20 |
| 20 Dec 77 | 6063-14183* | 13/28 | 80 |
| 21 Dec 77 | 6064-14235* | 14/27 | 80 |
| 21 Dec 77 | 6064-14241* | 14/28 | 90 |
| 6 Jan 78 | 21080-14121* | 12/27 | 10 |
| 6 Jan 78 | 21080-14124* | 12/28 | 10 |
| 7 Jan 78 | 21081-14128* | 13/28 | 60 |
| 8 Jan 78 | 21082-14234* | 14/27 | 80 |
| 8 Jan 78 | 21082-14241* | 14/28 | 90 |
| 24 Jan 77 | 21098-14123 | 12/27 | 80 |
| 24 Jan 77 | 21098-14130 | 12/28 | 60 |
| 25 Jan 77 | 21099-14182 | 13/27 | 90 |
| 25 Jan 77 | 21099-14184 | 13/28 | 90 |
| 26 Jan 77 | 21100-14243 | 14/28 | 90 |
| 11 Feb 77 | 21116-14133* | 12/27 | 10 |
| 11 Feb 77 | 21116-14140* | 12/28 | 20 |
| 12 Feb 77 | 21117-14192* | 13/27 | 70 |
| 12 Feb 77 | 21117-14195* | 13/28 | 70 |
| 13 Feb 77 | 21117-14251* | 14/27 | 30 |
| 13 Feb 77 | 21118-14253* | 14/28 | 30 |
| 1 Mar 78 | 21134-14144* | 12/27 | 30 |
| 1 Mar 78 | 21134-14150* | 12/28 | 0 |
| 2 Mar 78 | 21135-14203* | 13/27 | 30 |
| 2 Mar 78 | 21135-14205* | 13/28 | 10 |
| 3 Mar 78 | 21136-14264 | 14/28 | 50 |
| 9 Mar 78 | 30004-14421 | 12/27 | 10 |
| 9 Mar 78 | 30004-14423 | 12/28 | 10 |
| 28 Mar 78 | 30023-14414 | 12/27 | 90 |
| 28 Mar 78 | 30023-14420 | 12/28 | 90 |
| 29 Mar 78 | 30024-14472 | 13/27 | 80 |
| 29 Mar 78 | 30024-14475 | 13/28 | 80 |
| 30 Mar 78 | 30025-14533 | 14/28 | 90 |
| 15 Apr 78 | 30041-14415 | 12/27 | 90 |
| 15 Apr 78 | 30041-14422 | 12/28 | 80 |
| 17 Apr 78 | 30043-14534 | 14/28 | 70 |
| 25 Apr 78 | 21189-14235* | 13/28 | 90 |
| 26 Apr 78 | 21190-14294* | 14/28 | 10 |

* Landsat CCTs available at CRREL.

### b. 1978-79 winter season.

| Date | NASA scene ID | Path/row | Cloud (%) |
|---|---|---|---|
| 5 Dec 78 | 30275-14433 | 12/27 | 90 |
| 5 Dec 78 | 30275-14440 | 12/28 | 80 |
| 6 Dec 78 | 30276-14491 | 13/27 | 40 |
| 6 Dec 78 | 30276-14494 | 13/28 | 70 |
| 7 Dec 78 | 30277-14552 | 14/28 | 40 |
| 23 Dec 78 | 30293-14432 | 12/27 | 80 |
| 23 Dec 78 | 30293-14435 | 12/28 | 80 |
| 24 Dec 78 | 30294-14491* | 13/27 | 10 |
| 24 Dec 78 | 30294-14493* | 13/28 | 0 |
| 25 Dec 78 | 30295-14552 | 14/28 | 90 |
| 10 Jan 79 | 30311-14433 | 12/27 | 10 |
| 10 Jan 79 | 30311-14435 | 12/28 | 10 |
| 11 Jan 79 | 30312-14491* | 13/27 | 10 |
| 11 Jan 79 | 30312-14494* | 13/28 | 0 |
| 12 Jan 70 | 30313-14552 | 14/28 | 10 |
| 19 Jan 79 | 21458-14295 | 12/27 | 0 |
| 19 Jan 79 | 21458-14301 | 12/28 | 0 |
| 28 Jan 79 | 30329-14433 | 12/27 | 90 |
| 28 Jan 79 | 30329-14435 | 12/28 | 90 |
| 29 Jan 79 | 30330-14491 | 13/27 | 90 |
| 29 Jan 79 | 30330-14494 | 13/28 | 90 |
| 15 Feb 79 | 30347-14432 | 12/27 | 10 |
| 15 Feb 79 | 30347-14435 | 12/28 | 0 |
| 16 Feb 79 | 30348-14491 | 13/27 | 80 |
| 16 Feb 79 | 30348-14493 | 13/28 | 60 |
| 17 Feb 79 | 30349-14551 | 14/28 | 10 |
| 17 Feb 79 | 30349-14545* | 14/29 | |
| 5 Mar 79 | 30365-14431 | 12/27 | 90 |
| 5 Mar 79 | 30365-14434 | 12/28 | 90 |
| 6 Mar 79 | 30366-14485 | 13/27 | 90 |
| 7 Mar 79 | 30367-14550 | 14/28 | 90 |
| 23 Mar 79 | 30383-14430 | 12/27 | 30 |
| 23 Mar 79 | 30383-14432 | 12/28 | 10 |
| 29 Apr 79 | 30420-14485 | 13/27 | 90 |
| 29 Apr 79 | 30420-14492 | 13/28 | 90 |

**Table 2 (cont'd).**

c. 1979–80 winter season.

| Date | NASA scene ID | Path/row | Cloud (%) |
|---|---|---|---|
| 1 Dec 79 | 30636-14454 | 13/27 | 90 |
| 1 Dec 79 | 30636-14460 | 13/28 | 70 |
| 2 Dec 79 | 30637-14514 | 14/28 | 90 |
| 18 Dec 79 | 30653-14393 | 12/27 | 20 |
| 18 Dec 79 | 30653-14395 | 12/28 | 10 |
| 19 Dec 79 | 30654-14451* | 13/27 | 10 |
| 19 Dec 79 | 30654-14453* | 13/28 | 10 |
| 20 Dec 79 | 30655-14512 | 14/28 | 10 |
| 5 Jan 80 | 30671-14385 | 12/27 | 10 |
| 5 Jan 80 | 30671-14391 | 12/28 | 50 |
| 6 Jan 80 | 30672-14443* | 13/27 | 0 |
| 6 Jan 80 | 30672-14450* | 13/28 | 10 |
| 23 Jan 80 | 30689-14385 | 12/27 | 90 |
| 23 Jan 80 | 30689-14392 | 12/28 | 90 |
| 24 Jan 80 | 30690-14444 | 13/27 | 80 |
| 24 Jan 80 | 30690-14450 | 13/28 | 70 |
| 10 Feb 80 | 30707-14383 | 12/27 | 10 |
| 10 Feb 80 | 30707-14390 | 12/28 | 10 |
| 11 Feb 80 | 30708-14441* | 13/27 | 0 |
| 11 Feb 80 | 30708-14444 | 13/28 | 40 |
| 12 Feb 80 | 30709-14502 | 14/28 | 90 |
| 29 Feb 80 | 30726-14434 | 13/27 | 40 |
| 29 Feb 80 | 30726-14440 | 13/28 | 90 |
| 17 Mar 80 | 30743-14372 | 12/27 | 70 |
| 17 Mar 80 | 30743-14374 | 12/28 | 70 |
| 18 Mar 80 | 30744-14430 | 13/27 | 90 |
| 18 Mar 80 | 30744-14433 | 13/28 | 90 |
| 19 Mar 80 | 30745-14491 | 14/28 | 20 |
| 4 Apr 80 | 30761-14364 | 12/27 | 70 |
| 4 Apr 80 | 30761-14370 | 12/28 | 90 |
| 5 Apr 80 | 30762-14422 | 13/27 | 90 |
| 5 Apr 80 | 30762-14424 | 13/28 | 90 |
| 23 Apr 80 | 30780-14414 | 13/27 | 90 |
| 23 Apr 80 | 30780-14420 | 13/28 | 90 |
| 24 Apr 80 | 30781-14475 | 14/28 | 90 |

* Landsat CCTs available at CRREL.

The Landsat MSS observation (pixel) may be thought of as a point in a four-dimensional "color" space, where the values along each axis represent the radiant energy received by the satellite in one of the four bands (Fig. 5a). Observations that lie in a similar direction from the origin in this four-dimensional color space are said to be similar in color regardless of their total radiant energy. The distance (length) of an observation from the origin is a measure of the total radiance associated with that point. The algorithm is primarily designed to combine observations that are similar in color into the same classification category. There is provision for evaluating brightness differences between pixels and for weighting these differences in with the color discriminant when constructing the classification categories.

Discrimination based solely on color is obtained when the difference in direction between the solar vectors (observations) is examined. If the angle between the observations is smaller than some user-defined criterion, the vectors are considered to be lying in the same direction and, therefore, the observations are placed in the same category.

In addition to discrimination based solely on color, the GISS algorithm provides the capability of weighting total radiance differences into the discriminant equation for classification. The percent difference in brightness between two observations is computed. The calculated normalized difference is then combined with the color difference angle (expressed in steradians) by performing a weighted average in the RMS (root mean square) sense. This brightness-weighted quantity is now compared with the user-defined criterion ($\delta_{max}$). Thus, in the classification process, a relatively small weighting of brightness allows very large brightness differences to disqualify observations that are similar in color from membership in the same category, thereby adding a second level of discrimination.

There are two modes in which this classification scheme may be used: supervised and unsupervised. In the supervised mode the user specifies a signature, here shown as $\hat{B}$, the energy distribution in the four Landsat bands. If an observation lies within a solid angle smaller than the user-defined criterion, $\delta_{max}$, it is said to belong to the category represented by the multispectral signature, $\hat{B}$ (Fig. 5b). Therefore, all vectors lying within a cone of angle $\delta_{max}$ about signature $\hat{B}$, which represents category $X$, belong to category $X$.

In the unsupervised classification a maximum value of $\delta_{max}$ is specified by the user for the combined color-brightness difference. If the color-brightness difference is less than or equal to $\delta_{max}$, then pixels $i$ and $j$ are grouped into the same category.

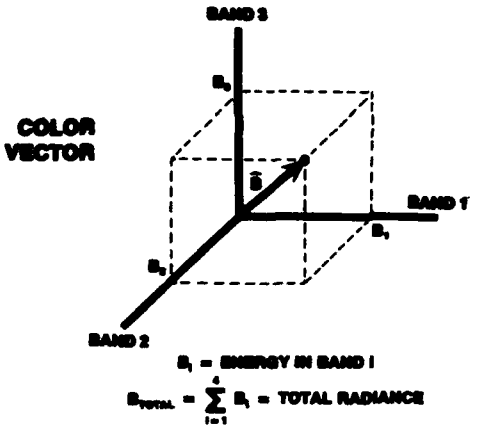


*a. A color vector illustrated for three-dimensional space, but all four Landsat bands are used in the classification process.*

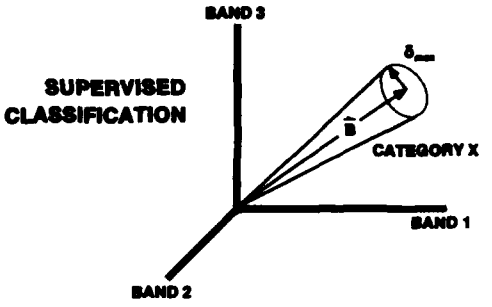


*b. Supervised mode. The user-defined criterion, $\delta_{max}$, defines category X about the signature B. Any color vector that lies within this cone belongs to category X. This is illustrated for three bands; however, all four Landsat bands are used in the computer classification algorithm.*

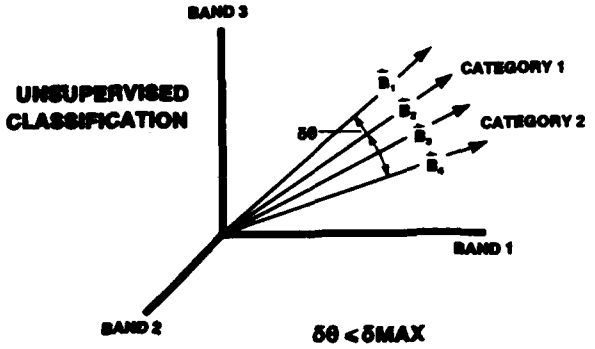


*c. Unsupervised mode. $\hat{B}_1$ is similar in direction to $\hat{B}_2$ ($\delta\phi \leq \delta_{max}$) and is placed in category 1. $\hat{B}_4$ is similar in direction to $\hat{B}_3$ and is placed in category 2. However, $\hat{B}_3$ is also similar in direction to $\hat{B}_2$ (category 1), so category 1 is merged with category 2.*

*Figure 5. The concept of the four-dimensional "color" space used in the computer classification algorithm (after Merry et al. 1977).*

To illustrate this in terms of equations used in the computer analysis, each pixel's signature is represented by a real vector in the four-dimensional space. The signature is the sum of the four components and is defined as the real vector represented by the following equation:

$$\hat{S} = (S_1, S_2, S_3, S_4). \quad (1)$$

The unit vector is used to define the direction of the pixel. The magnitude of $S$ is defined as the square root of the sum of the squares of the four components:

$$|S| = \sqrt{S_1^2 + S_2^2 + S_3^2 + S_4^2} \quad (2)$$

The unit vector is then defined as:

$$S = \frac{\hat{S}}{|S|} \quad (3)$$

Note that the magnitude of unit vector $S$ will always equal 1. The unit vector and real vector are calculated for each pixel.

Each pixel $i$ and $j$ is compared with every other pixel in terms of color difference and brightness difference. The color difference is the absolute value of the difference in the unit vectors:

$$\delta_c = |S_i - S_j|. \quad (4)$$

The brightness difference is the sum of the total radiance or brightness divided by two. This number is divided into the absolute value of the difference in the total radiances between two pixels:

$$\delta_B = \frac{|B_i - B_j|}{(B_i + B_j)/2} \quad (5)$$

The differences in color and brightness between pixels $i$ and $j$ are then combined to calculate an overall signature difference between the two pixels. $W$ is a parameter for specifying the relative weighting given to the color and brightness differences. The overall signature difference is defined as:

$$\Delta_{ij} = \sqrt{W\delta_C^2 + (1-W)\delta_B^2} \quad (6)$$

If one suspects that the ground categories display greater brightness differences than color differences, one may wish to increase the importance of brightness differences when using the $W$ parameter to better differentiate among the ground categories. If $W$ equals 0, then only the brightness difference is used. If $W$ is set to 1, then the color difference is used for the signature difference between two pixels.

In the unsupervised mode the color vector corresponding to the first observation is compared to all subsequent observations. If color vector 1 is similar in direction to color vector 2 (i.e. $\delta\theta \leq \delta_{max}$), observation 2 is placed in the same category as the first observation (Fig. 5c). In a similar fashion, observations subsequent to observation 2 are compared to the second observation and so on, right up to the last observation. If in the process of constructing categories a member is found that belongs to a previous category, the new category is chained (or linked) to the original classification category, forming one joint category (Ungar 1977). In effect the unsupervised classification will form several categories based on a criterion specifying maximum color difference permissible between members of the same category:

$$\Delta_{ij} \leq \delta_{max} \quad \text{or} \quad \delta\theta \leq \delta_{max} \quad (7)$$

As shown, $\hat{B}_3$ is similar in direction to $\hat{B}_1$ (cone of angle $\delta\theta \leq \delta_{max}$) and is placed in category 1 (Fig. 3). $\hat{B}_4$ is similar in direction to $\hat{B}_2$ and is placed in category 2. $\hat{B}_4$ is also similar in direction to vector $\hat{B}_3$ (category 1). Therefore, category 1 is merged with category 2.

When the pixels are chained together in clusters, a cluster represents a category defined by two extreme signatures. This hypothesis is due to the fact that pixels within certain ground cover classes display a continuous variation in signature over space between the two extreme signatures, for example, mixtures of vegetation and urban areas. The computer program searches for the pixel in a category for which the color-brightness difference is largest, say $\hat{S}_i$, and this pixel is called the first pure type. Next the program determines the second pixel in that category that is furthest in terms of signature from the first pure-type pixel. This pixel is then the second pure type, say $\hat{S}_j$.

Once these two pure-type pixels are found, then each pixel in that category can be expressed as a linear combination of the two pure types. Therefore, the vector signature for an observed pixel, $\hat{S}$, is defined by the following equation, with $\hat{S}_i$ and $\hat{S}_j$ representing the two pure types (a two-component mixture) with $\eta$ to define the fraction between the two extremes:

$$\hat{S}_{obs} = \eta\hat{S}_i + (1-\eta)\hat{S}_j. \quad (8)$$

The digital processing of the Landsat CCTs was accomplished through a cooperative agreement with NASA GISS. Computer algorithms for the analysis of the digital data were developed at GISS (Ungar 1977). These algorithms were accessed using the CRREL remote entry terminal to the main computer facility (IBM 4341), located at GISS in New York City.

**Physical setting**

The Upper Saint John River Basin was selected because the SSARR model is used for operational flood forecasting by the New Brunswick Flood Forecast Centre. The subbasins evaluated included the Allagash (3240 km²), Dickey (7410 km²), and Ninemile Bridge (3340 km²) (Fig. 6).

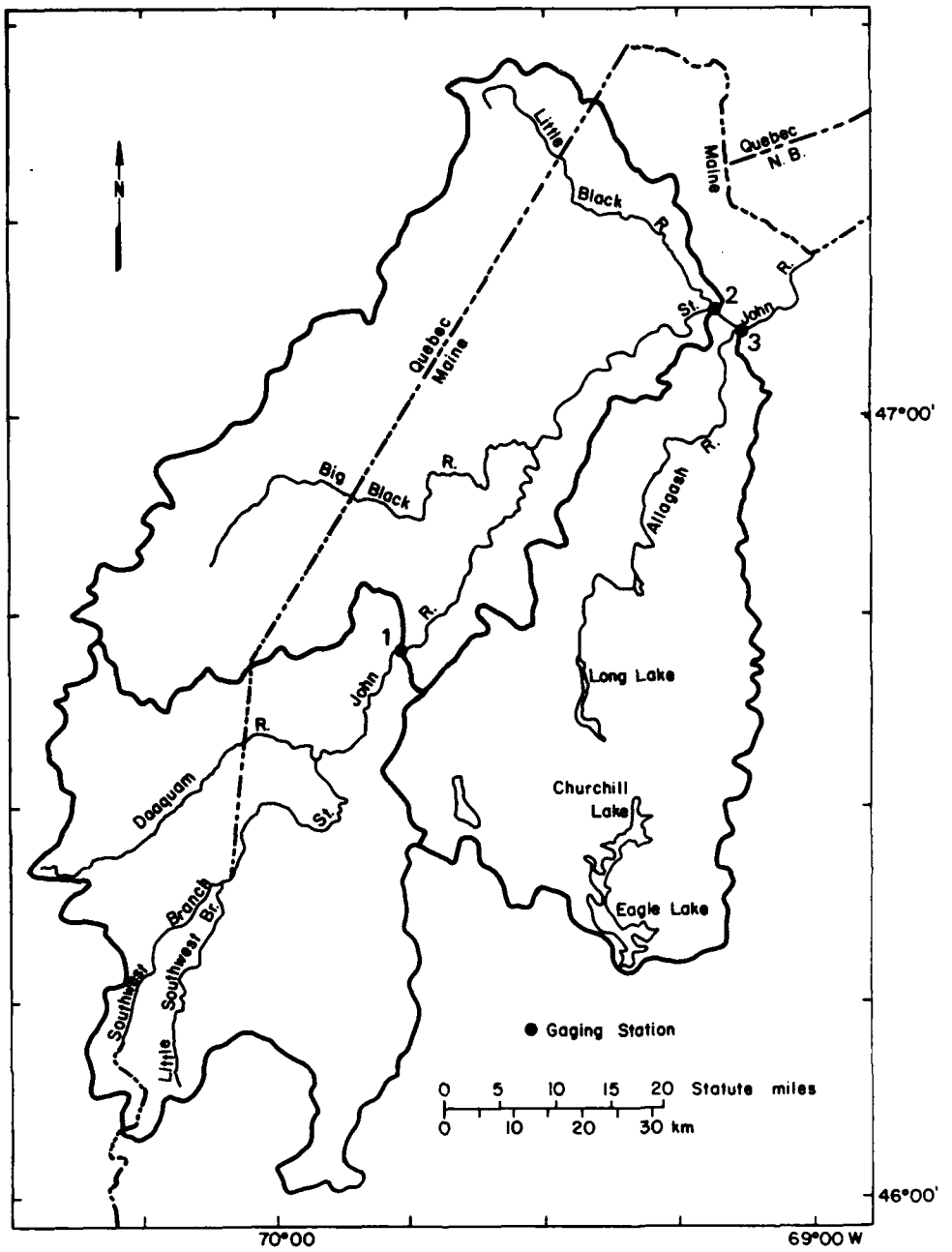


*Figure 6. Location of the outflow points for the Ninemile Bridge (1), Dickey (2) and Allagash (3) subbasins of the Upper Saint John River Basin.*

The climate of this region is humid continental. The average annual precipitation is approximately 91 cm and occurs uniformly throughout the year, with about 30% in the form of snow. Average snow depth ranges between 51 and 102 cm, with the upper limit exceeding 127 cm (New England Division, Corps of Engineers 1967). Water equivalent of the snowpack reaches a maximum in late March and usually exceeds 25 cm.

The geology and vegetation of the area were previously mapped and served as a data base of site characteristics in this study (McKim 1975, McKim and Merry 1975, Environmental Research and Technology, Inc. 1977). Elevations within the subbasin range from 150 to 600 m, and forest cover varies from 76 to 93%.

The snowpack in the Saint John River Basin is of shallow to medium depths of less than 30 cm of

water equivalent for an overall accumulation (Hansen 1975). There are rare maximum accumulations of 32 cm of water equivalent. The snowpack melts and contributes to runoff in a time period of less than 5 weeks. Coincident rainfall at the time of snowmelt normally occurs during the spring runoff. Ice movement also complicates the runoff process.

Most (85%) of the watershed is covered by a dense forest with predominantly coniferous forests in the valleys and lower slopes. Hardwood forests cover the hilltops of minor relief. Mixed forests occur principally along the valley sides. Forestry operations create new areas of clearcuts. The region of study lies in the physiographic province of the Chaleur Upland. The mean elevation of the upland province is 250 to 300 m.

**The SSARR model**

The SSARR model was developed for use in the North Pacific Division of the U.S. Army Corps of Engineers (U.S. Army Engineer Division, North Pacific 1975). The model is used for operational river forecasting and river management activities in connection with the Cooperative Columbia River Forecasting Unit, sponsored by the National Weather Service, U.S. Army Corps of Engineers, and the Bonneville Power Administration. The SSARR model was previously calibrated for the Saint John River Basin by the New Brunswick Flood Forecast Centre, Canada, to forecast runoff due to snowmelt and precipitation (Power et al. 1980).

The SSARR model is a continuous deterministic simulation model of the river basin system (Fig. 7). Streamflow is synthesized by evaluating snowmelt and rainfall. There are three basic components in the SSARR model:

1) A generalized watershed model for synthesizing runoff from snowmelt, rainfall, or a combination of the two.
2) A river system model for routing streamflows from upstream to downstream points through channel and lake storage.
3) A reservoir regulation model in which reservoir outflow and contents may be analyzed along with synthesized inflow and free flow or any of several modes of operation (U.S. Army Engineer Division, North Pacific 1975).

In this study only the generalized watershed portion of SSARR was used to predict outflow from the three gauging stations (Fig. 6).

Snowmelt is calculated in the SSARR model by use of the temperature index method or a generalized snowmelt equation with additional options of subroutines for a snow-cover depletion approach or the elevation band approach. Because meteorological data were available from a station near the Allagash gauging station, the temperature index

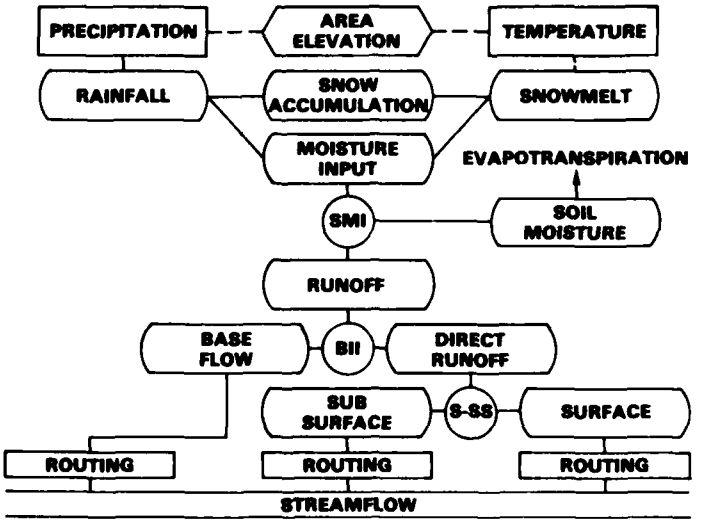


*Figure 7. Schematic of the SSARR (Streamflow Synthesis and Reservoir Regulation) model (after U.S. Army Engineer Division, North Pacific 1975).*

method was selected. Precipitation and air temperature values were used from this site. The watershed elevation distribution versus percent area data were input as a table to the SSARR model. This table is used to relate freezing level elevations to percentage of snow-covered area and is required only for the snowmelt computations. The elevation band subroutine was selected so that the snow water equivalent data could be used as input. An inventory of snow water equivalent is then maintained on each elevation band.

Flood forecasting models have been developed for the Saint John River Basin. The New Brunswick Electric Power Commission and the New Brunswick Department of the Environment have cooperated to adapt the SSARR program to the Saint John River Basin (Smith 1980, Hansen 1975). Ground truth maps of the snow survey data have been combined with the satellite image interpretation of the snow-covered area for input to the SSARR model.

Snow cover was first mapped in the Saint John River Basin by the Earth Satellite Corporation for the 1974 melt period. Numerical estimates of snow-covered area were accomplished for nine zones using NOAA visible band imagery (Hansen 1975). In 1975 NOAA/NESS supplied snow-covered area estimates as backup to the River Forecast Center. Landsat image interpretation was also accomplished in 1975 in conjunction with low-level infrared photography obtained over 10 snow survey locations (Ferguson and Lapczak 1977a,b). Snow-cover measurements have since been coordiated with overflights of the Landsat satellite.

## APPROACH

In northeastern North America snow accumulation has been found to be specific for vegetative and landscape units (Steppuhn and Dyck 1974, Adams 1976, Adams and Barr 1979, FitzGibbon and Dunne 1979, Adams and Roulet 1982). Because of this phenomenon, 11 snow courses were established based on vegetative type, slope, aspect, and elevation (Table 5, Fig. 8). The sites were selected primarily on the basis of four vegetation classes: mixed, hardwoods, softwoods, and cleared land. When possible, various elevations (from 180 to 450 m) and aspects (north, south, east, and west) within an 8-km radius of Allagash were selected for each vegetation type.

A meteorological station was installed at Allagash, Maine, to obtain background data on local climatic conditions. The instrumentation included a rain gauge, maximum and minimum thermometers, a hygrothermograph, and an anemometer. In addition, a Landsat data collection platform was installed at site 13 to measure air and ground temperatures and wind passage during the 1978–79 winter season.

Measurements of snow depth and water equivalent were obtained at the 11 snow courses in conjunction with the Landsat-2 and -3 imagery for the 1977–78, 1978–79, and 1979–80 winter seasons. Snow pit studies were conducted at three of the 11 sites (sites 1, 9, and 13) during each Landsat pass to characterize snow properties. Weekly snow course and snow pit measurements were performed at the meteorological station (site 1).

**Table 3. Snow course site characteristics in the Allagash area, Maine.**

| *Site number* | *Latitude/longitude* | *Elevation (ft)* | *Elevation (m)* | *Aspect* | *Vegetation* | *Other site characteristics* |
|---|---|---|---|---|---|---|
| 1 | 47°05'14"N/69°01'30"W | 610 | 190 | Level | Cleared | Adjacent to met station |
| 3 | 47°06'17"N/69°09'30"W | 1000 | 300 | North | Softwoods | 9% slope, sheltered, closed canopy |
| 4 | 47°07'19"N/69°06'40"W | 650 | 200 | Level | Softwoods | Sheltered, 90% canopy cover |
| 5 | 47°08'03"N/69°07'26"W | 840 | 250 | Northeast | Mixed | 50% open/50% hardwoods, unsheltered |
| 7 | 47°09'31"N/69°05'17"W | 840 | 250 | Southeast | Hardwoods | 15–30% slope |
| 9 | 47°08'38"N/69°02'49"W | 900 | 270 | Level | Cleared | Old burn scar, swampy area |
| 10 | 47°03'49"N/69°08'56"W | 1240 | 380 | Southeast | Mixed | 7–8% slope |
| 11 | 47°03'47"N/69°09'52"W | 1300 | 400 | North | Hardwoods | 3–4% slope, 50% open/50% hardwoods |
| 12 | 47°04'04"N/69°11'06"W | 1140 | 350 | Level | Softwoods | Sheltered |
| 13 | 47°04'44"N/69°10'28"W | 880 | 270 | Level | Cleared | Steep slope with 200–250 ft (60–75 m) rise directly east of site, sheltered from east wind |
| 15 | 47°07'30"N/69°04'08"W | 1450 | 440 | Level | Mixed | Highest elevation |

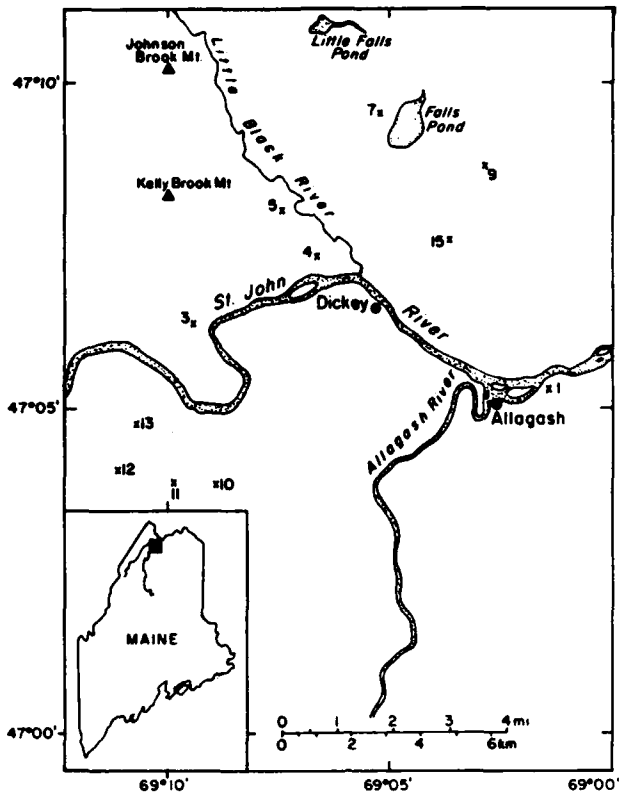


*Figure 8. Locations of the 11 snow courses in the Allagash, Maine, area.*

Figure 9 shows the maximum, minimum, and average values for snow depth and water equivalent for the 11 snow course sites at the time of the Landsat satellite overpasses. Detailed tables on the snow depth and water equivalent data for each snow course site are shown in Appendix A. Appendix B is a computerized listing of the daily meteorological data that was obtained during 1977–80 at the Allagash site in support of the snow cover mapping project. Additional meteorological information can be found in Bates (1983).

The Landsat MSS digital data were analyzed to determine whether a correlation existed between snow depth and the measured intensities in the four spectral bands. The five snow-covered Landsat scenes used in the analysis were the only ones available that were relatively cloud-free: 6 January 1978, 11 February 1978, 1 March 1978, 24 December 1978, and 11 January 1979. Histograms of the brightness values in MSS band 7 for a 300- × 300-pixel (420 km²) area located near Allagash, Maine, were investigated. The data for the five winter scenes were registered with the assistance of a Ramtek image display unit. The 11 snow course sites were identified within the 300- × 300-pixel area. Individual band count values, band ratios, and band summations were evaluated. A solar elevation correction was also applied to account for differences in insolation for the different Landsat dates.

A scene from 31 May 1978 was used to classify the three subbasins using the GISS-MAP1 algorithm. During this season the forest types could easily be separated due to the phenological state of the deciduous trees. The young leaves of these trees showed a high near-infrared reflectance (MSS 7) in comparison with that of the evergreen forest. The land cover types classified included water, open areas, softwoods, hardwoods, and mixed forest. The selection of training sites for classification of vegetation types was aided by the use of aerial photography.

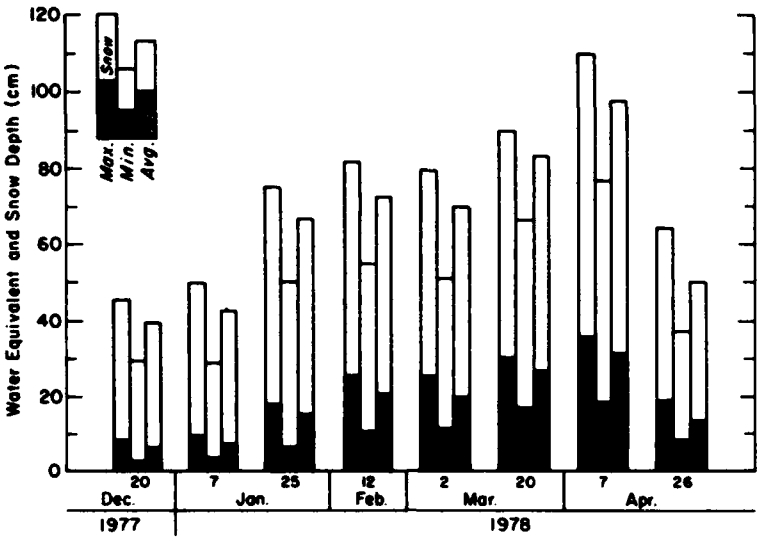


*a. 1977–78 winter season.*

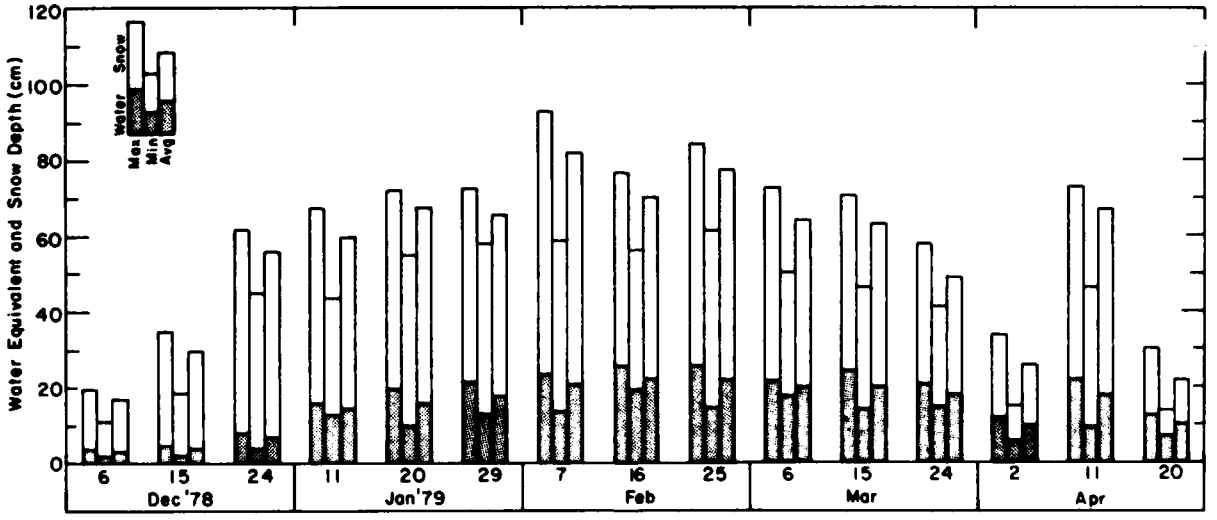


*b. 1978–79 winter season.*

***Figure 9. Snow depth and water equivalent values during the Landsat overpasses.***

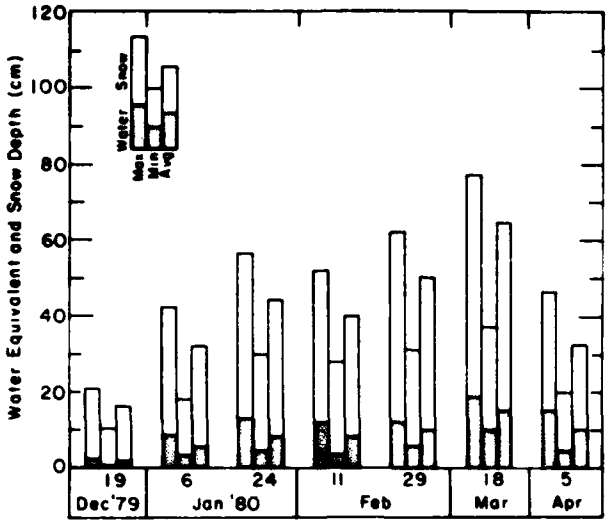


*c. 1979–80 winter season.*

*Figure 9 (cont'd).*

## RESULTS AND DISCUSSION

### Histogram analysis—uncorrected Landsat data

The statistical analysis of the uncorrected Landsat data indicated that a direct correlation did not exist between snow depth and the measured intensities in the four MSS spectral bands. This was true in the comparison among the various snow course sites for a single Landsat scene and among the various Landsat scenes for individual snow course sites.

Although the Landsat reflected-radiance values measured for a single pixel (0.45 hectare) did not increase (or decrease) uniformly with increasing snow depth, it was hypothesized that on a regional scale ($> 26$ km$^2$) changes in overall brightness might occur. To test this hypothesis, histograms of the MSS 5 and 7 data were examined for the five winter scenes, the 31 May 78 scene, and an autumn scene from 27 October 1977.

The MSS bands 5 and 7 count histograms for the five land-cover classes and the total area for each of the six Landsat scenes are shown in Figures 10. The count values for MSS 5 range from 0 to 127 and for MSS 7 range from 0 to 63. Although the number of pixels varies from class to class due to the nature of the study site, the number of pixels within any class remains constant from one observation date to another. Much of the skewness observed in the regional histograms appears to result from the water and open area pixels. This is particularly noticeable for water surfaces because the absorption characteristic of water is replaced by an open expanse of highly reflective ice and snow cover.

For the forest cover classes, the shift in histogram shape is less dramatic. For the softwoods class there is little noticeable change in the shape or dimensions of the histogram between the Landsat winter scenes and the 27 Oct 77 scene. Albedo investigations have shown that the more complete closure of the softwood canopy precludes significant reflectivity changes with a snowpack (Leonard and Eschner 1968). The histograms for the hardwoods and mixed forest show a decrease in kurtosis and a change of the histogram mode to the brighter count values as the snow depth increases.

The MSS band 7 data were used to avoid the saturation of the MSS sensor that occurred in the other multispectral bands under snow conditions. In addition, the use of MSS 7 avoided the effects resulting from the decompression of MSS bands 4, 5, and 6 that is applied during ground image processing of the Landsat data. The vegetation and

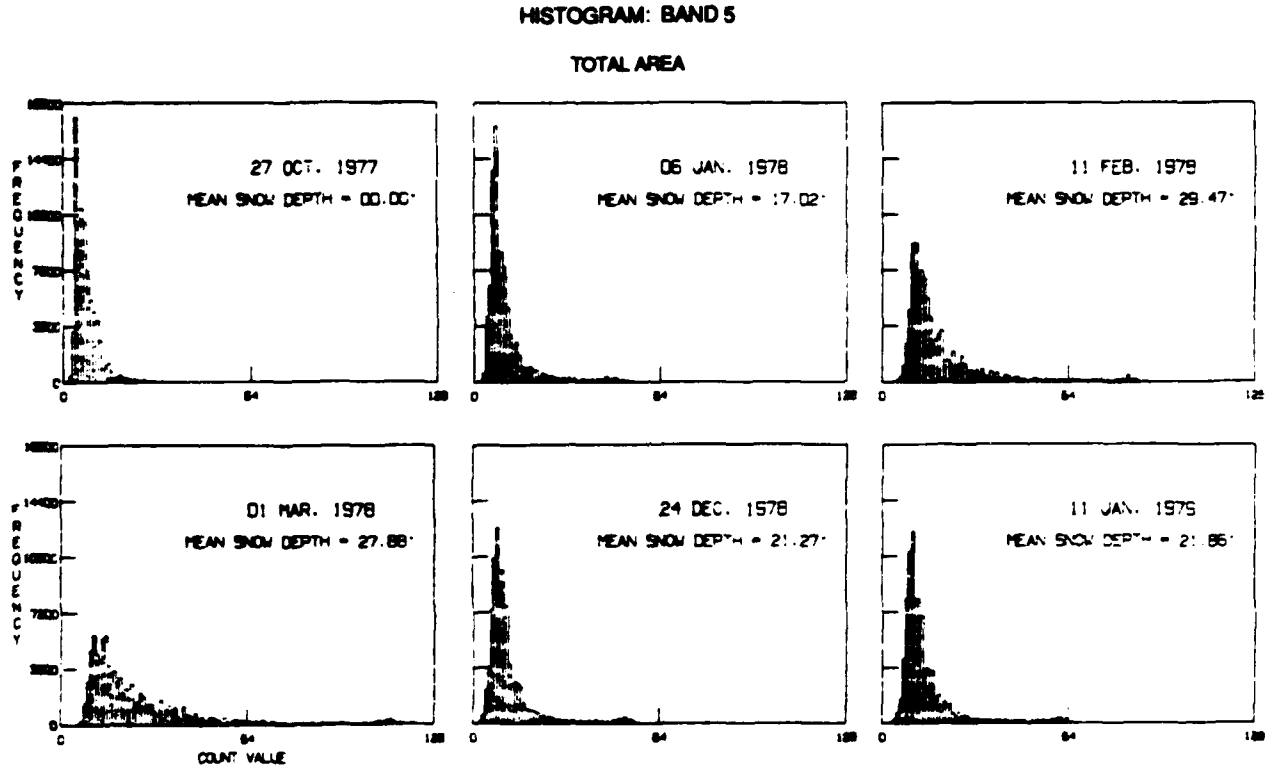


*a. MSS band 5.*

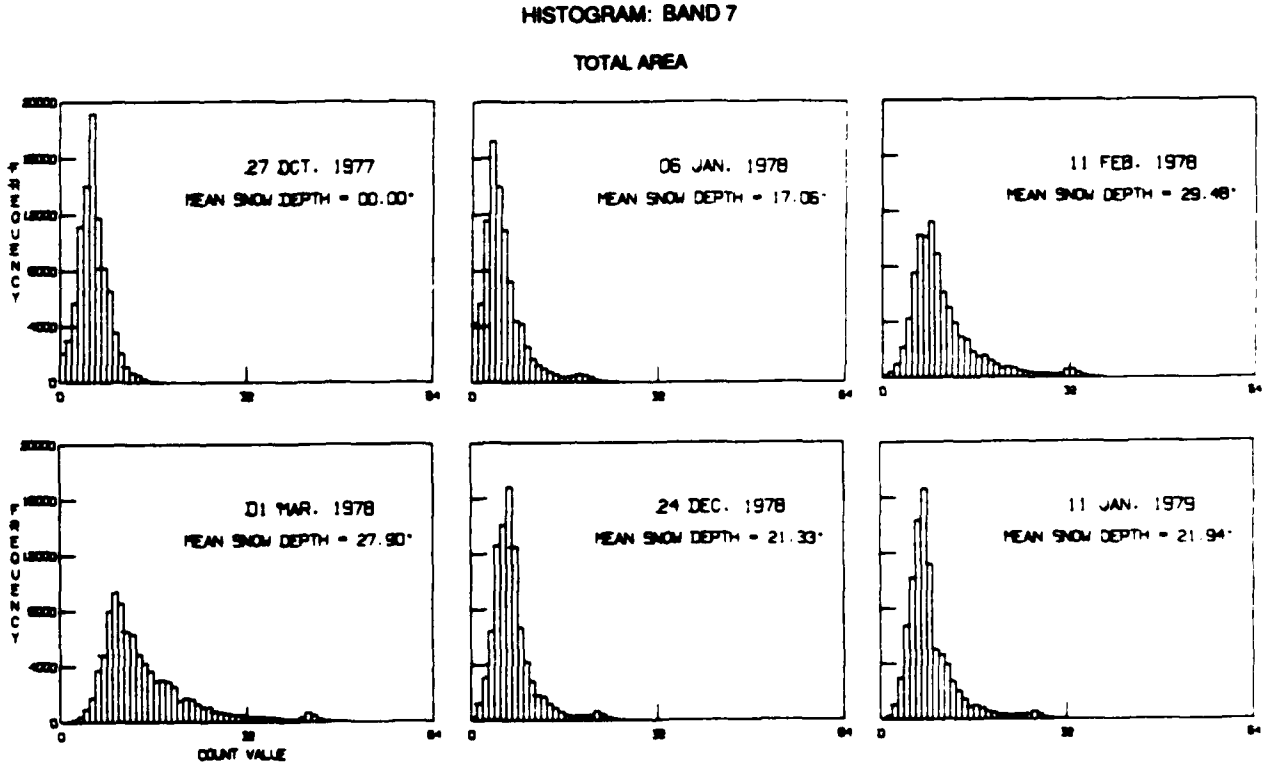


*b. MSS band 7.*

***Figure 10. Landsat histograms for the total area of the 300- × 300-pixel area located near Allagash, Maine.***

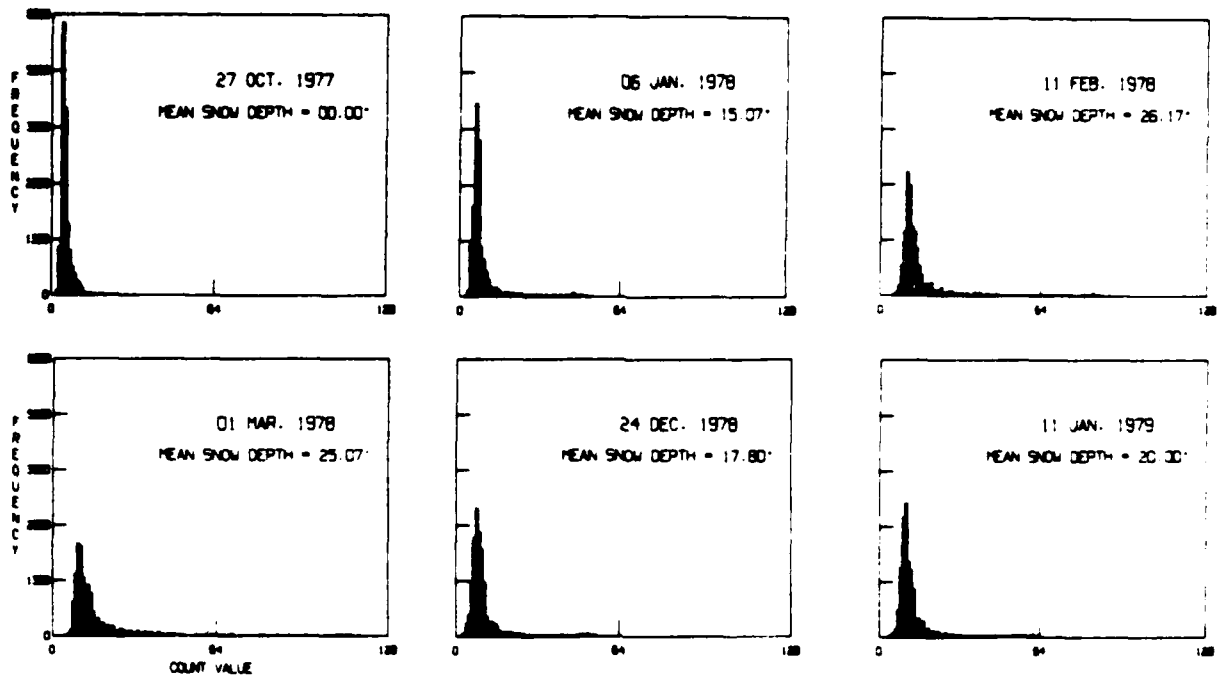


*a. MSS band 5.*

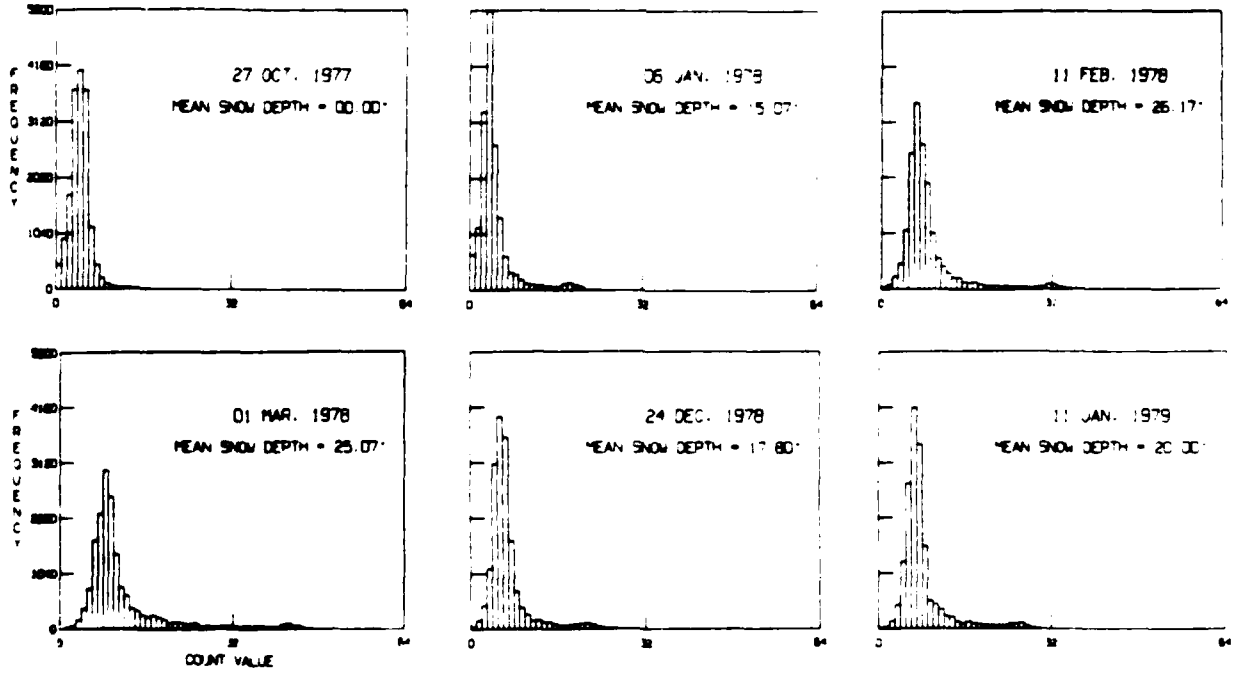


*b. MSS band 7.*

***Figure 11. Landsat histograms for the softwoods class.***

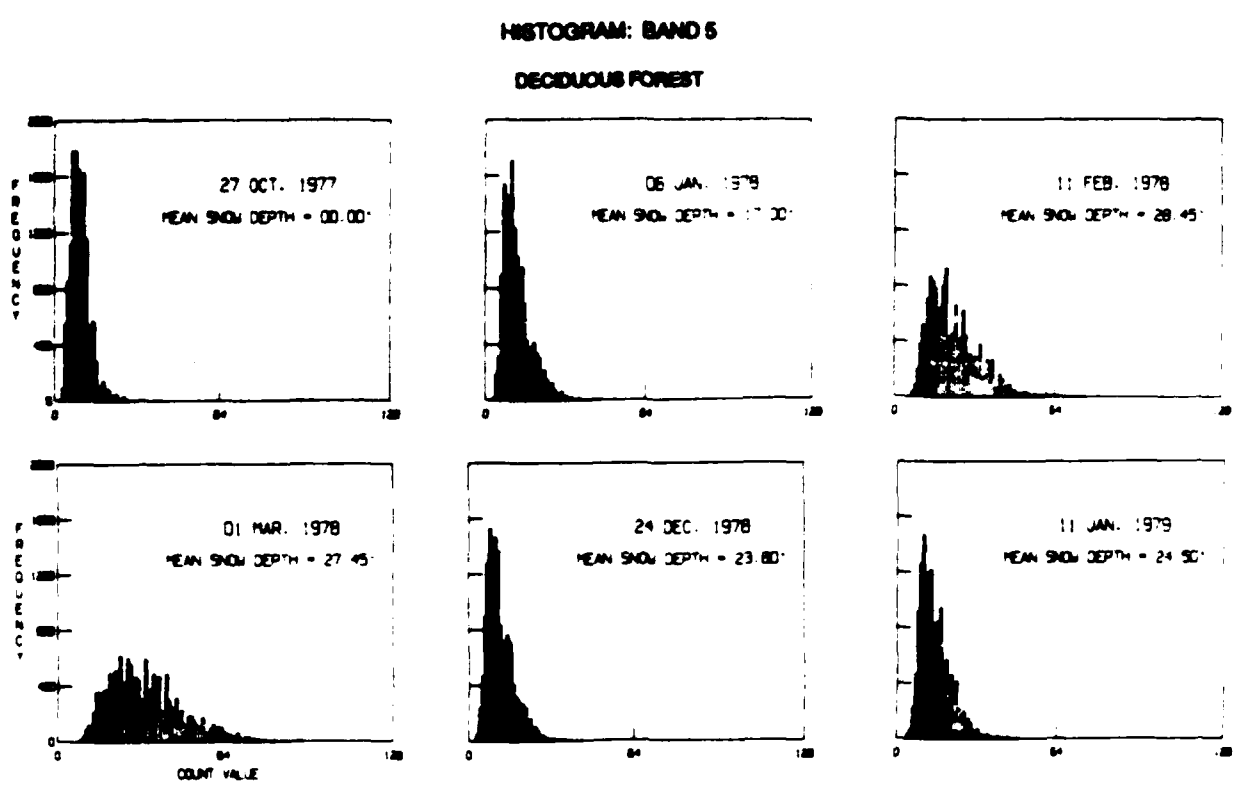


*a. MSS band 5.*

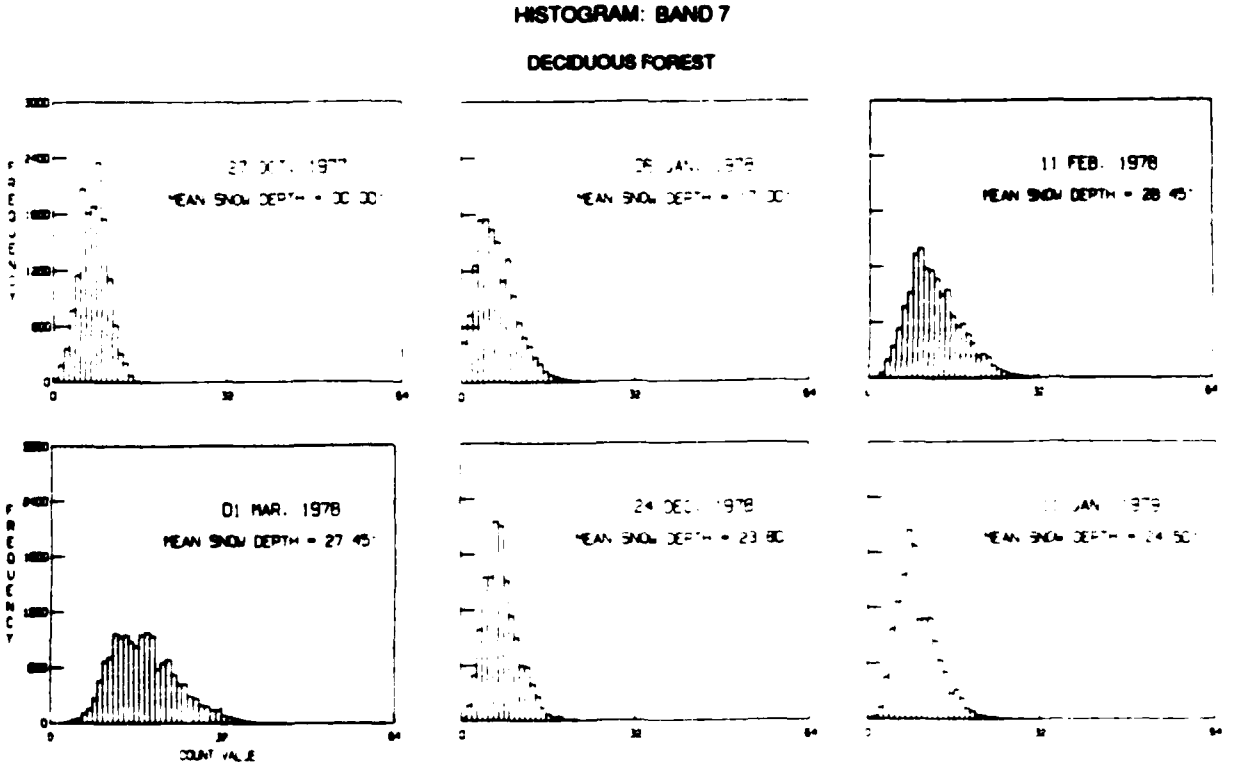


*b. MSS band 7.*

***Figure 12. Landsat histograms for the hardwoods class.***

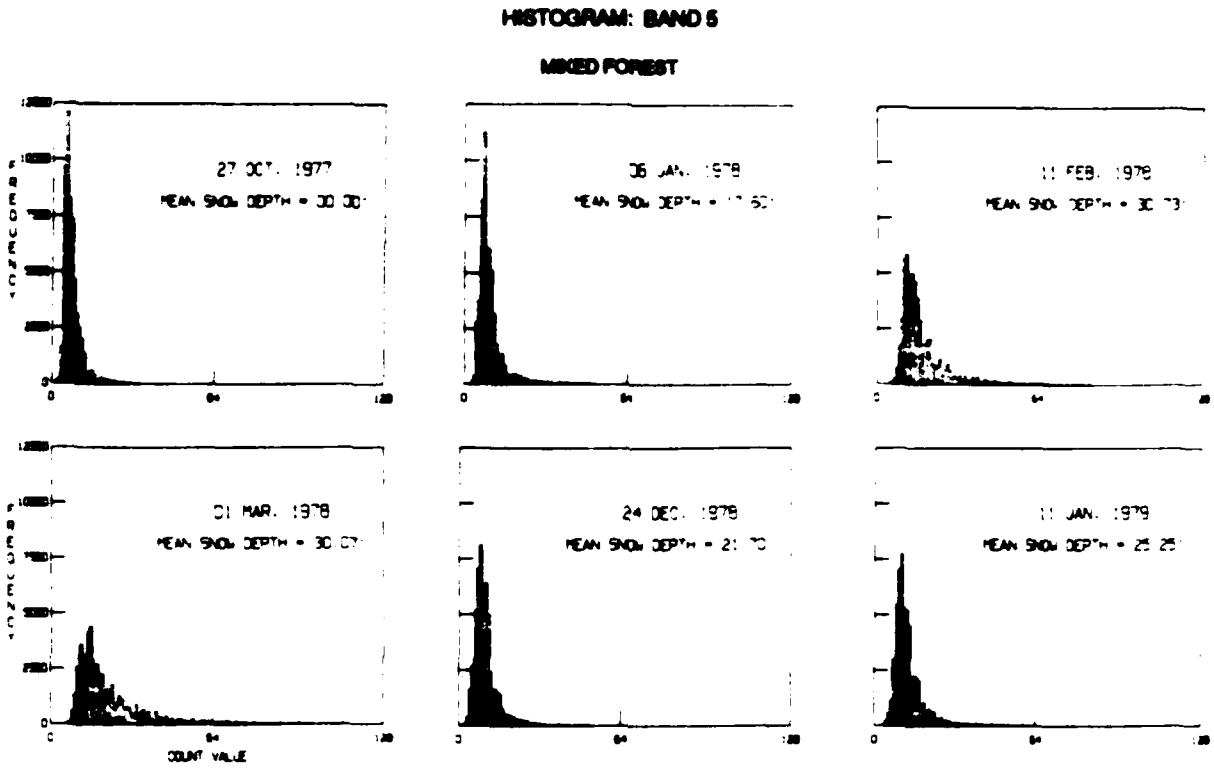


*a. MSS band 5.*

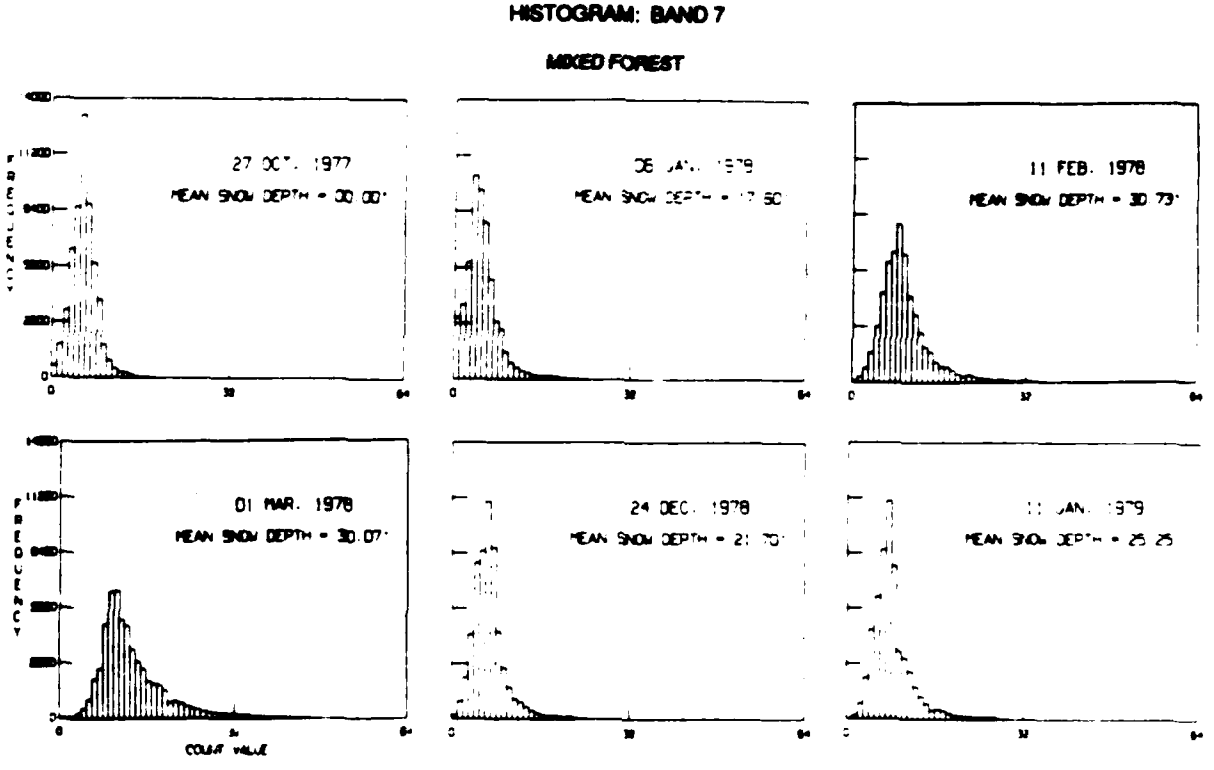


*b. MSS band 7.*

***Figure 13. Landsat histograms for the mixed forest class.***

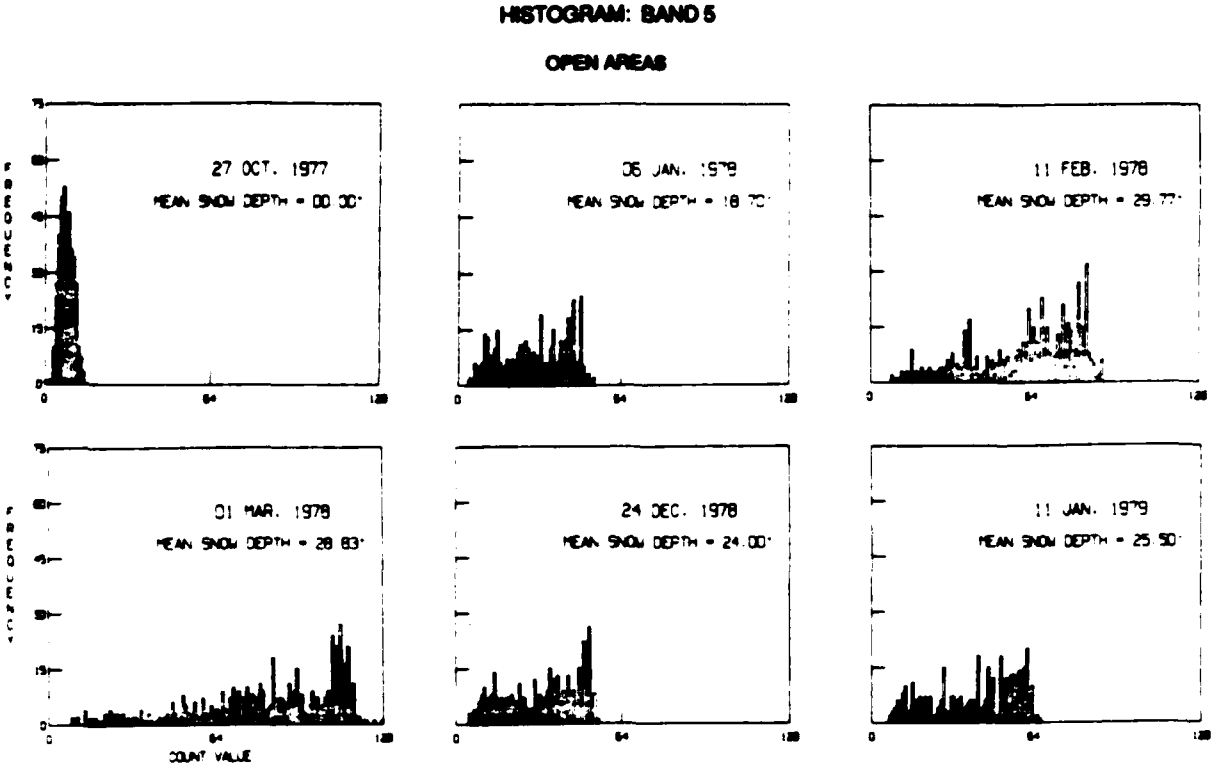


*a. MSS band 5.*

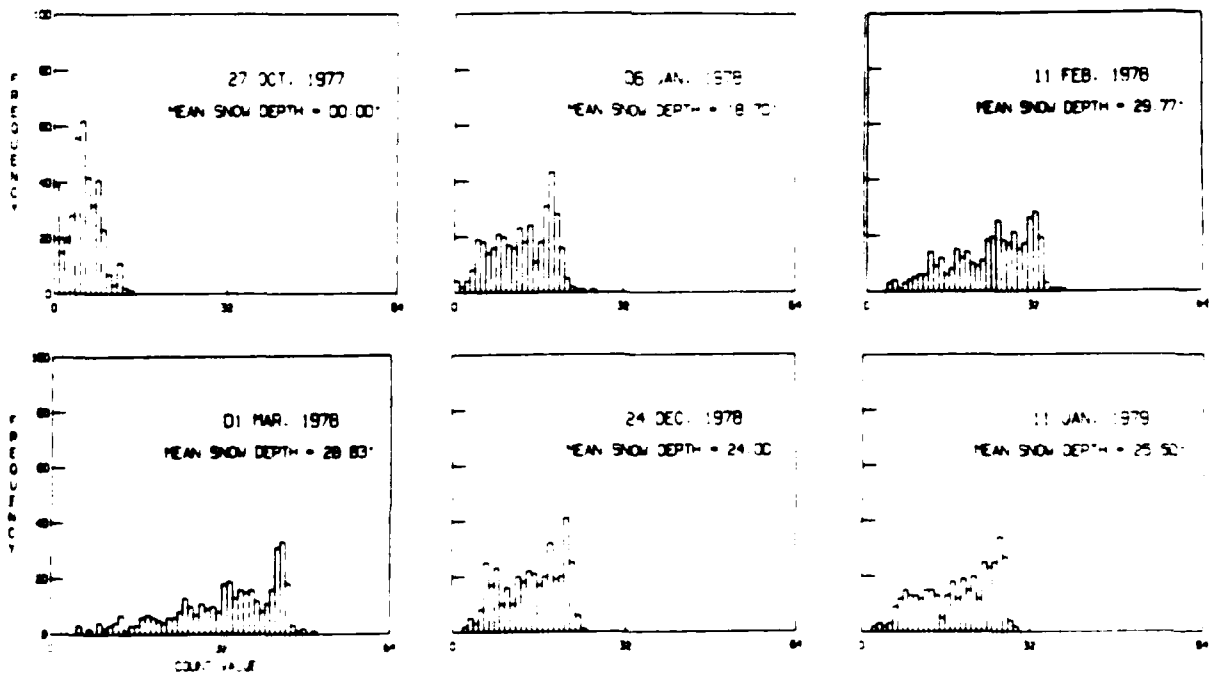


*b. MSS band 7.*

***Figure 14. Landsat histograms for the open areas class.***

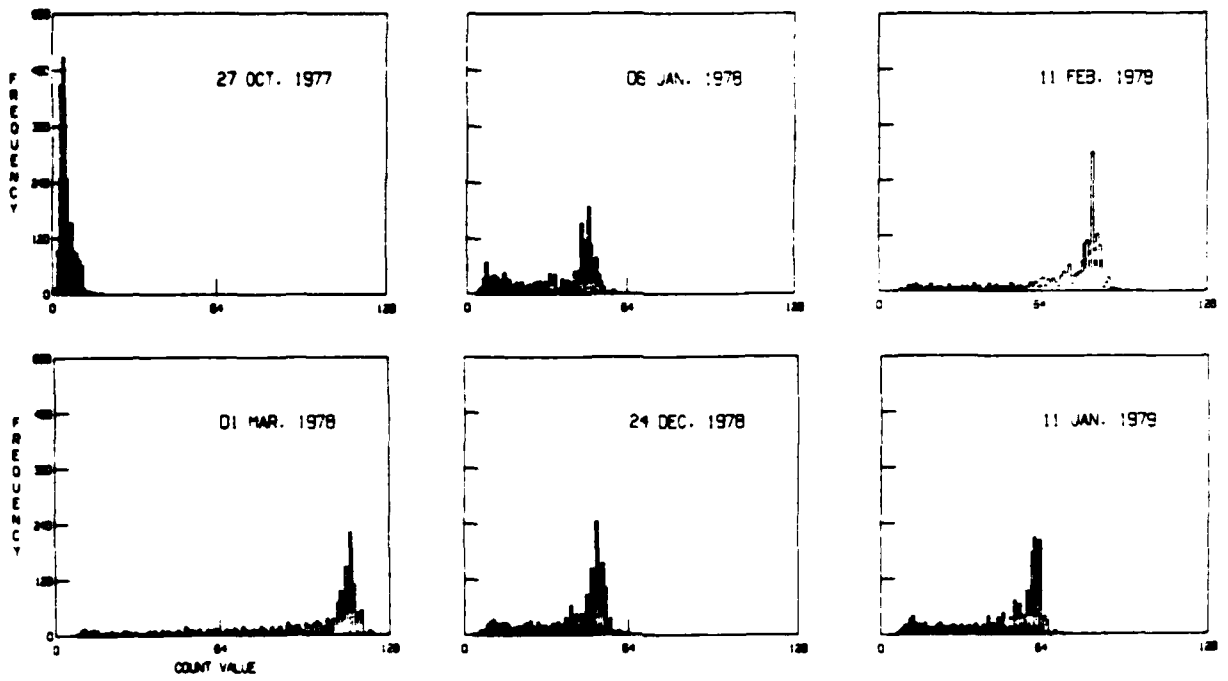


*a. MSS band 5.*

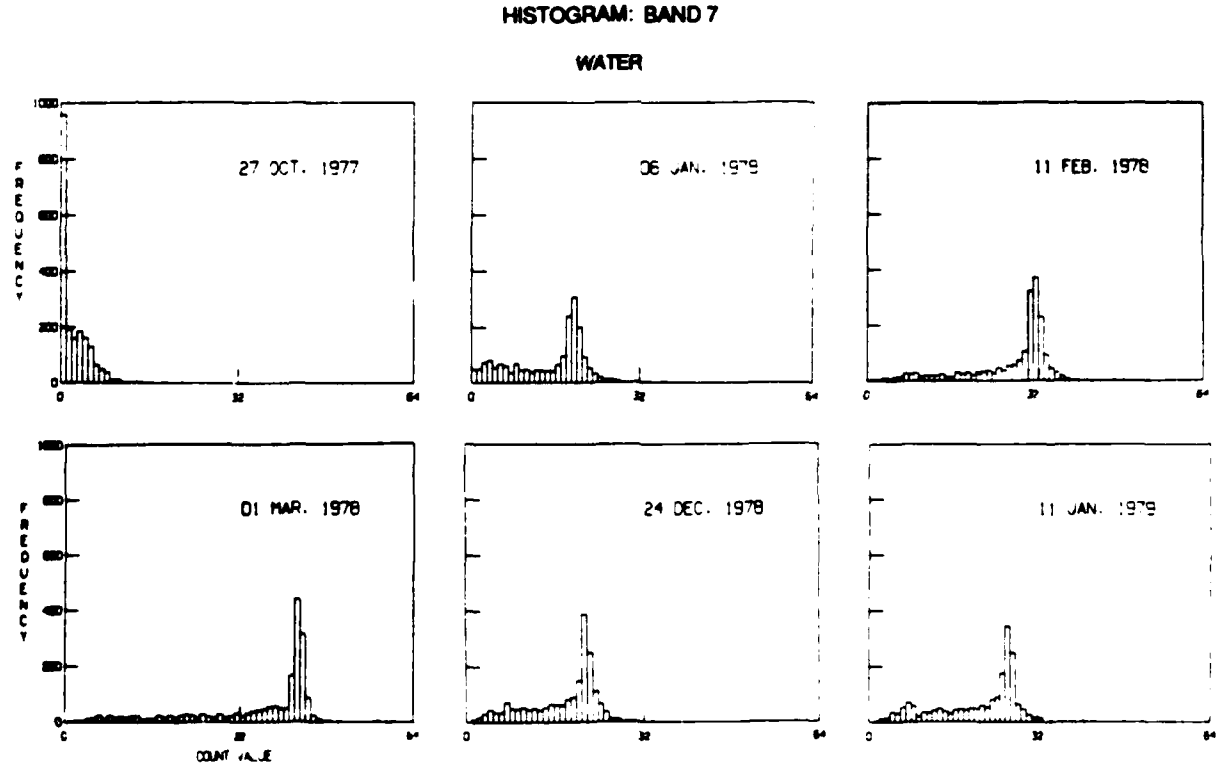


*b. MSS band 7.*

***Figure 15. Landsat histograms for the water class.***

low sun elevation of the 27 Oct 77 scene made it similar to winter conditions, but without snow. The histogram of the 27 Oct 77 Landsat scene exhibits a unimodal distribution with low variance (Fig. 12). As snow depth increases over the total landscape, there is a decrease in kurtosis and a corresponding increase of skewness toward the bright end of the histogram. One explanation is that as snow depth in a landscape increases throughout a snow season, the reflectance within a pixel increases with additional accumulations of snow. This results in a migration of the regional histogram from the snowless vegetation cluster of 27 Oct 77 to the brighter snow intensities observed in the Landsat winter scenes.

To quantify this observed change in histogram shape, a snow index ($I_s$) was developed based on examining the various indices of skewness and kurtosis for each histogram. The equation developed was defined as:

$$I_s = a_3 * \frac{\text{pop(total)}}{\text{pop(mode)}} * \cos(E) \qquad (9)$$

in which $I_s$ is the snow index, $a_3$ is the moment coefficient of skewness, pop(mode) is the pixel population of the histogram mode, pop(total) is the total pixel population, and cos($E$) is the cosine of the solar elevation angle.

A linear regression analysis was performed with the snow index and the mean regional snow depth for the five winter scenes. The following equation was derived:

$$\text{Snow depth} = 2.079 * (I_s) - 1.111 \qquad (10)$$

in which snow depth is measured in inches. The snow index, $I_s$, was found to predict mean snow depth with a standard error of estimate of ±2.08 in.

Present techniques used by the Corps of Engineers, New England Division, consist of selecting representative snow courses within watersheds for Corps reservoir project areas. The data from these snow courses are used to determine an arithmetic mean of snow depth and water equivalent for that particular watershed. An error cannot be attributed to these watershed snow estimates as there is not a good data base to compare with the estimated data values. Therefore, it is assumed that the standard error of estimate of ±2 in. would be comparable to conventional methods.

To test the snow depth analysis procedure, two additional Landsat scenes from other winter seasons were used. Table 4 compares the Landsat estimate of snow depth with available ground measurements of snow depth taken around the Landsat pass.

**Table 4. Landsat estimates of regional snow depth compared to available ground measurements.**

| *Landsat estimate* | | *Ground measurements* | |
|---|---|---|---|
| *Date* | *Depth (cm)* | *Date* | *Depth (cm)* |
| 11 Feb 73 | 90.2 | 1 Feb 73 | 84.6 |
| | | 19 Feb 73 | 96.3 |
| 19 Apr 74 | 40.4 | 16 Apr 74 | 60.2 |
| | | 7 May 74 | 28.7 |

**Histogram analysis—corrected and resampled Landsat data**

The initial results of the uncorrected Landsat data indicated that a relationship did exist between the shape of the MSS 7 histogram for an area and the depth of snow on the ground. To verify whether this effect was real or an artifact of the data, a closer examination was made of the data.

In comparing satellite observations, factors other than surface reflectivity may influence the Landsat count values used in the evaluation. In particular, atmospheric parameters (such as cloud cover), the effect of solar position, and satellite sensor characteristics may be important.

Clear sky winter conditions prevailed during all the Landsat passes. To account for variations between the three Landsat satellites and the differences in solar elevation, a transformation of Landsat counts to energy values was applied to the data:

$$\text{energy} = [(\text{count} * \text{gain}) + \text{offset}]/\cos(\text{zenith}) \qquad (11)$$

where energy is measured in mW cm$^{-2}$/sr, gain is the difference between the maximum and minimum sensitivities divided by the number of count intervals (63 or 127), offset is the minimum radiance sensitivity of the sensor and cos(zenith) is the cosine of the solar zenith angle. Table 5 shows the values of these parameters for each of the Landsat scenes.

Figures 16 through 21 are the corrected histograms for the total area and the five land cover classes for MSS bands 5 and 7. The unequal zenith

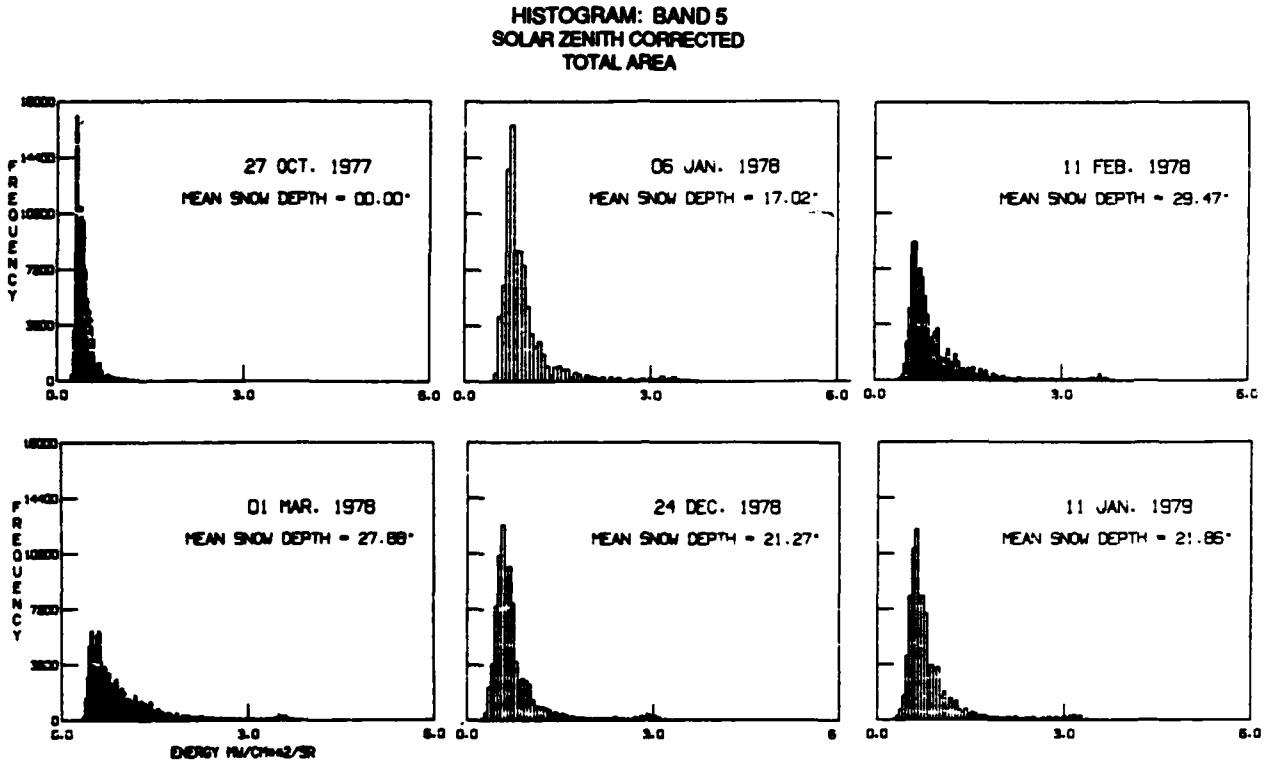


*a. MSS band 5.*

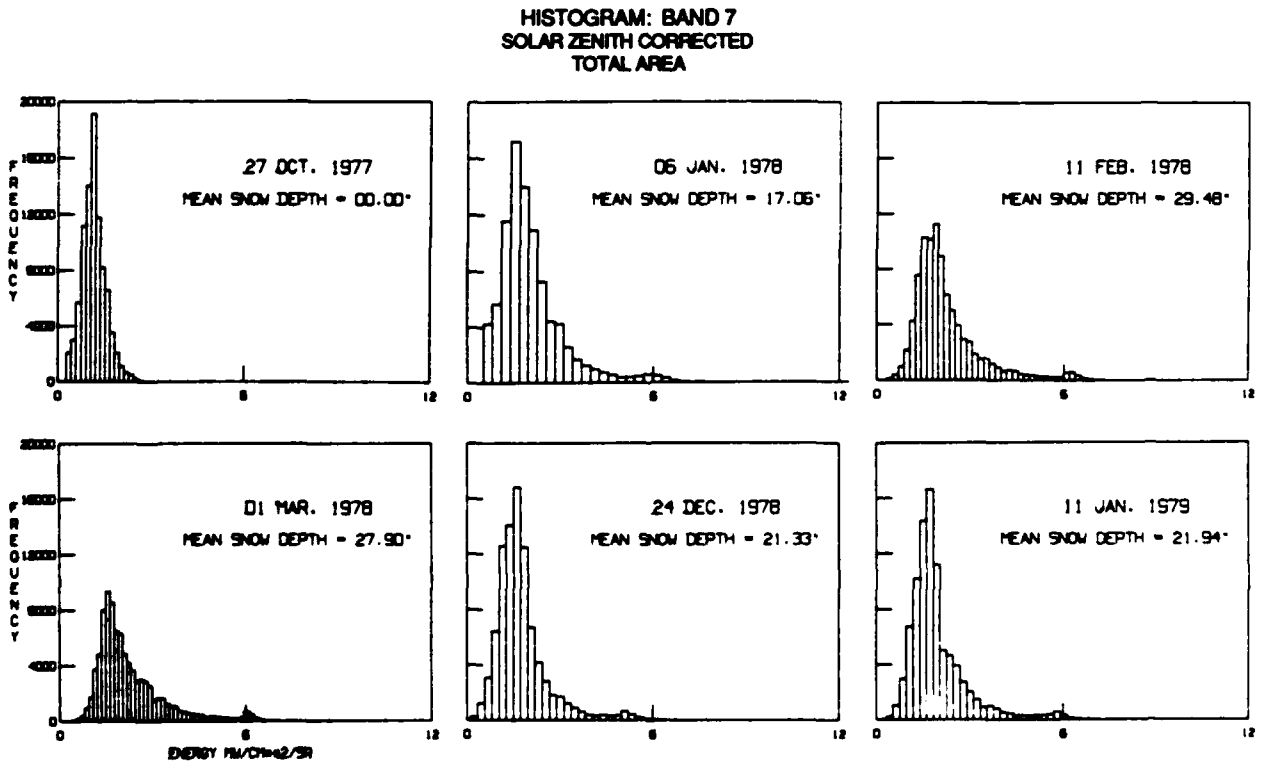


*b. MSS band 7.*

***Figure 16. Landsat histograms (corrected) for the total area of the 300- × 300-pixel area located near Allagash, Maine.***

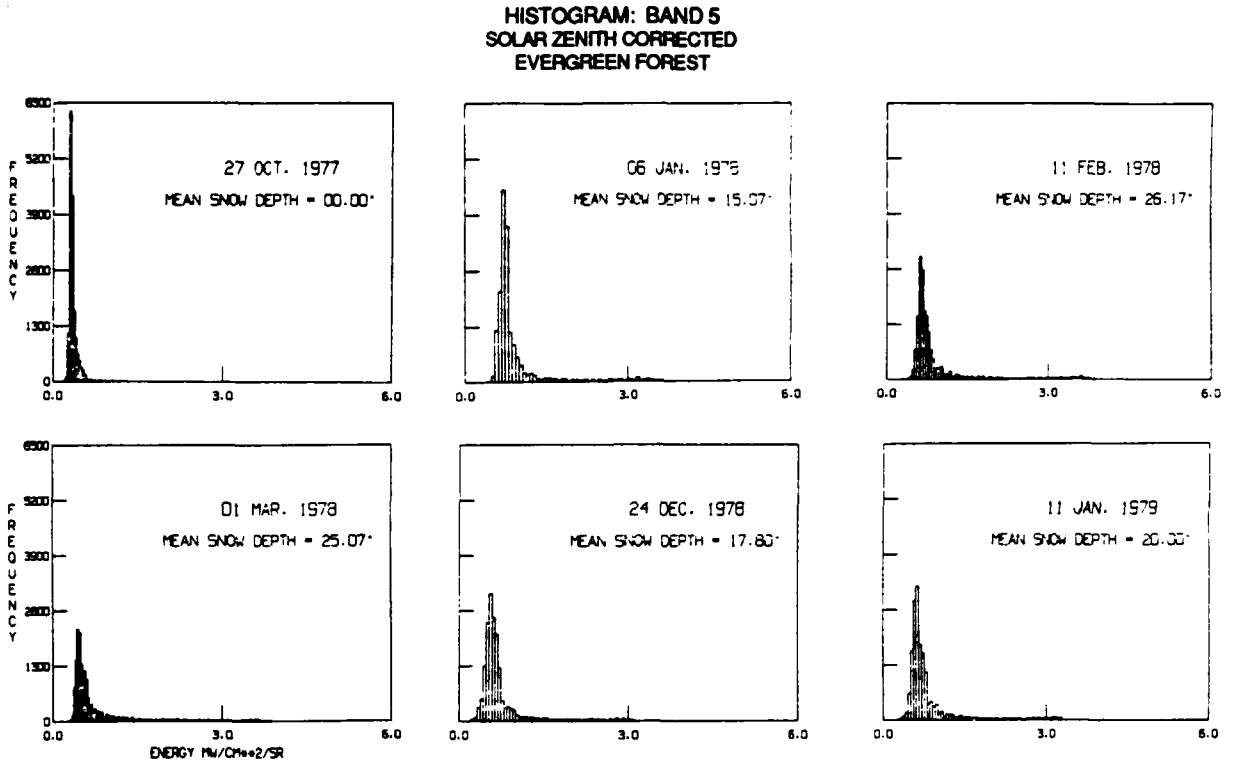


*a. MSS band 5.*

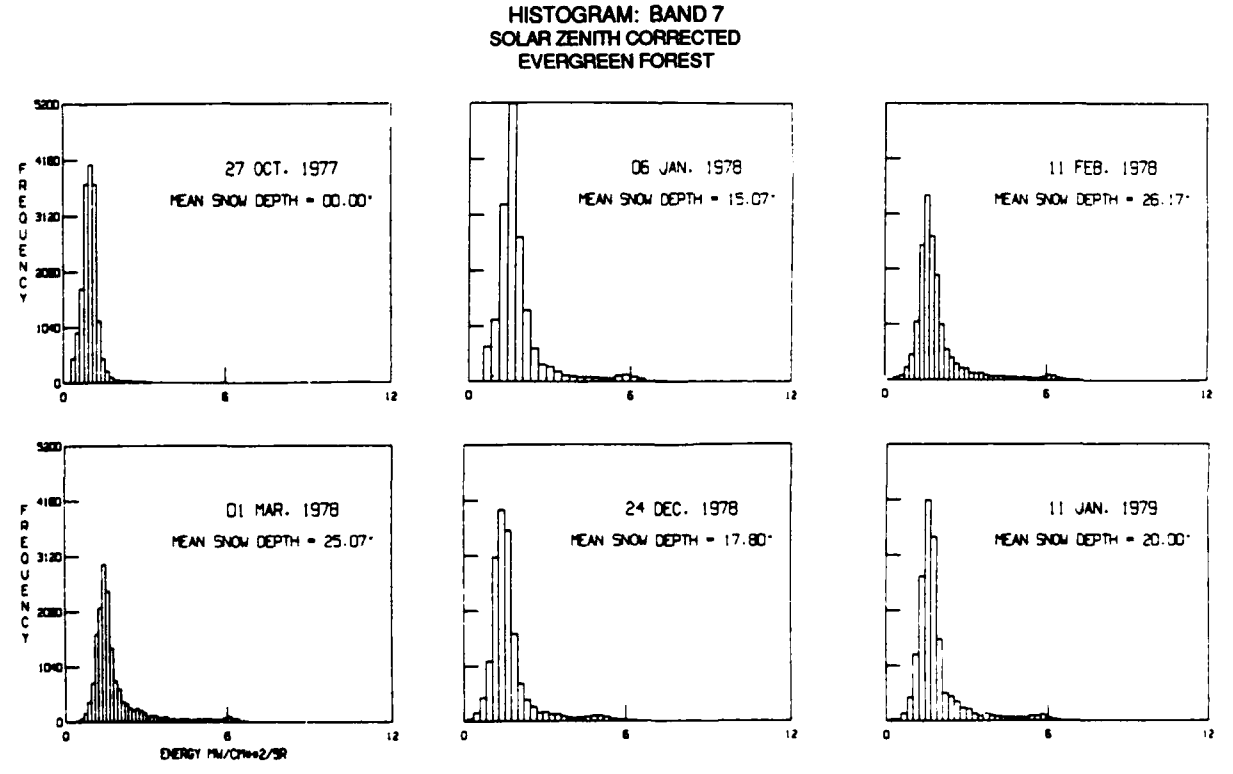


*b. MSS band 7.*

*Figure 17. Landsat histograms (corrected) for the softwoods class.*

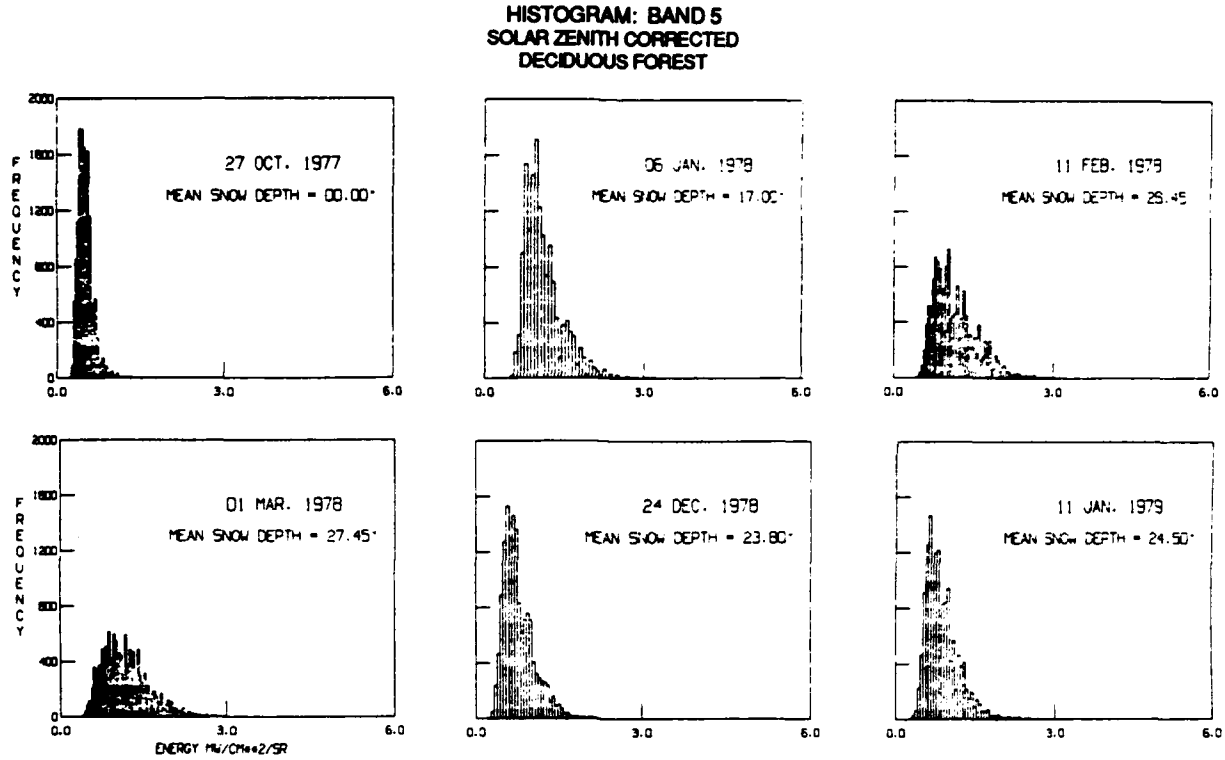


*a. MSS band 5.*

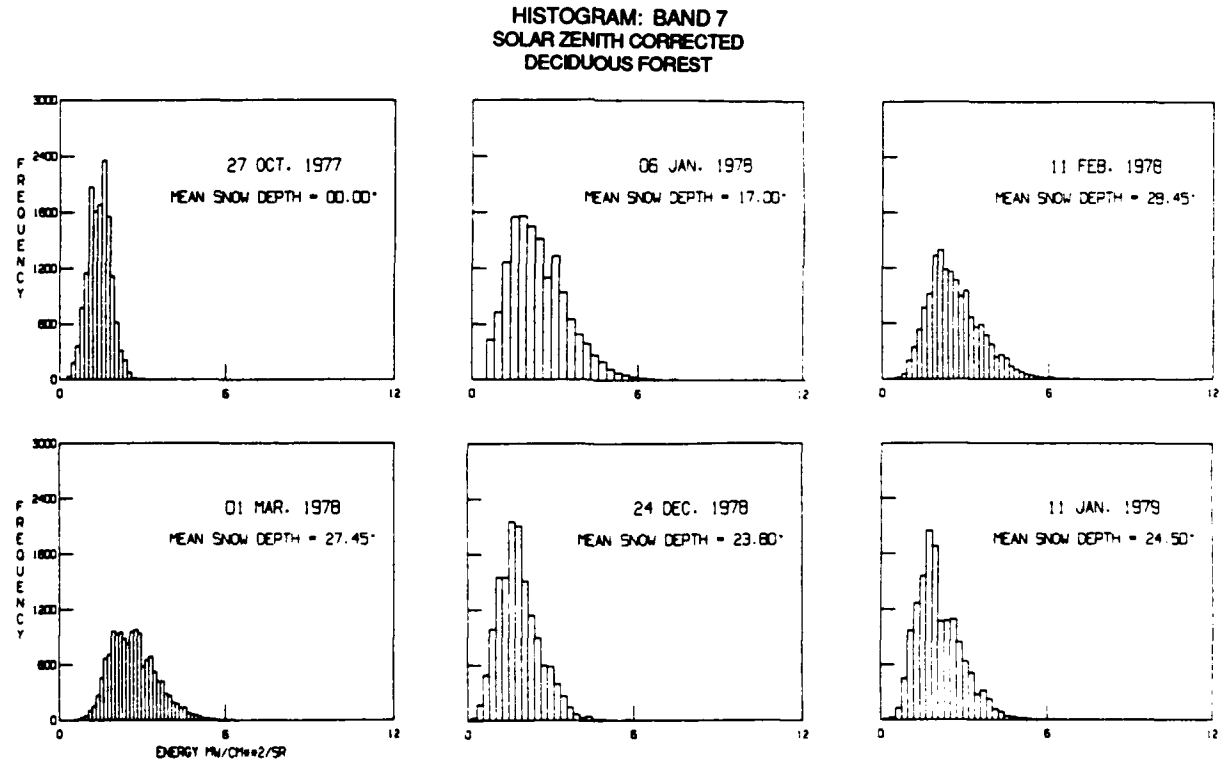


*b. MSS band 7.*

*Figure 18. Landsat histograms (corrected) for the hardwoods class.*

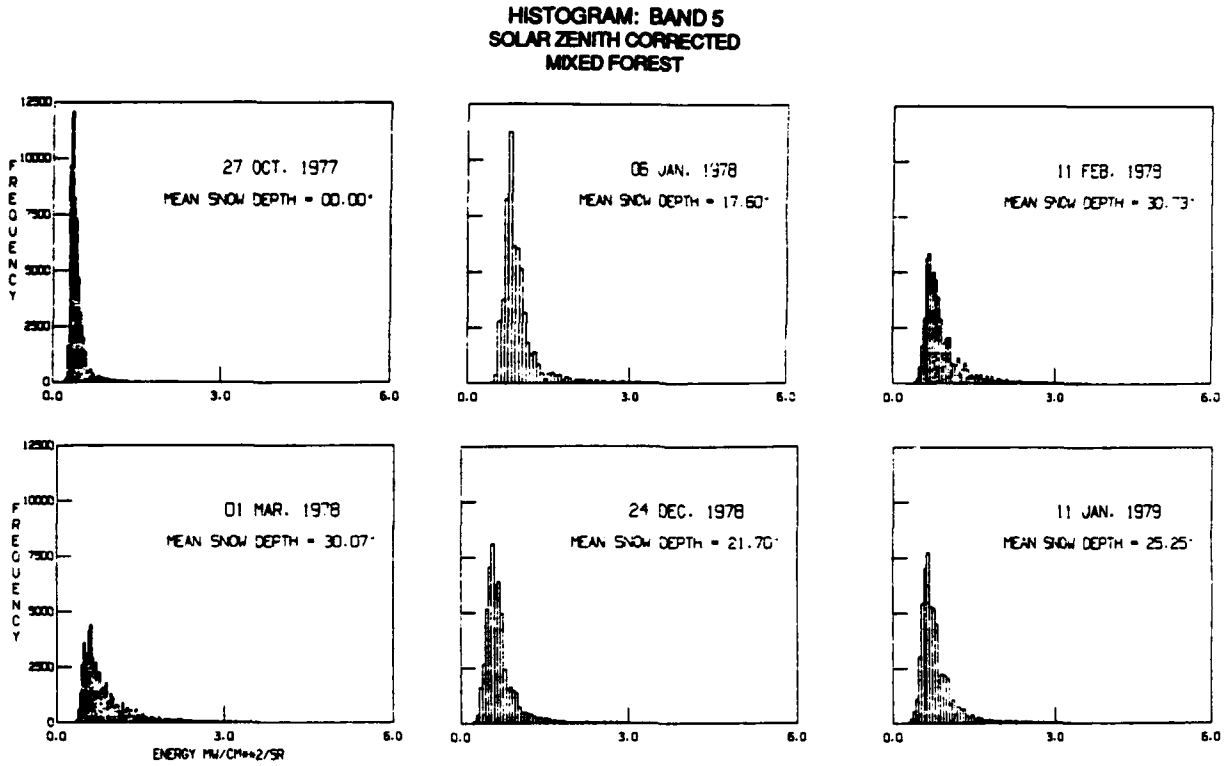


*a. MSS band 5.*

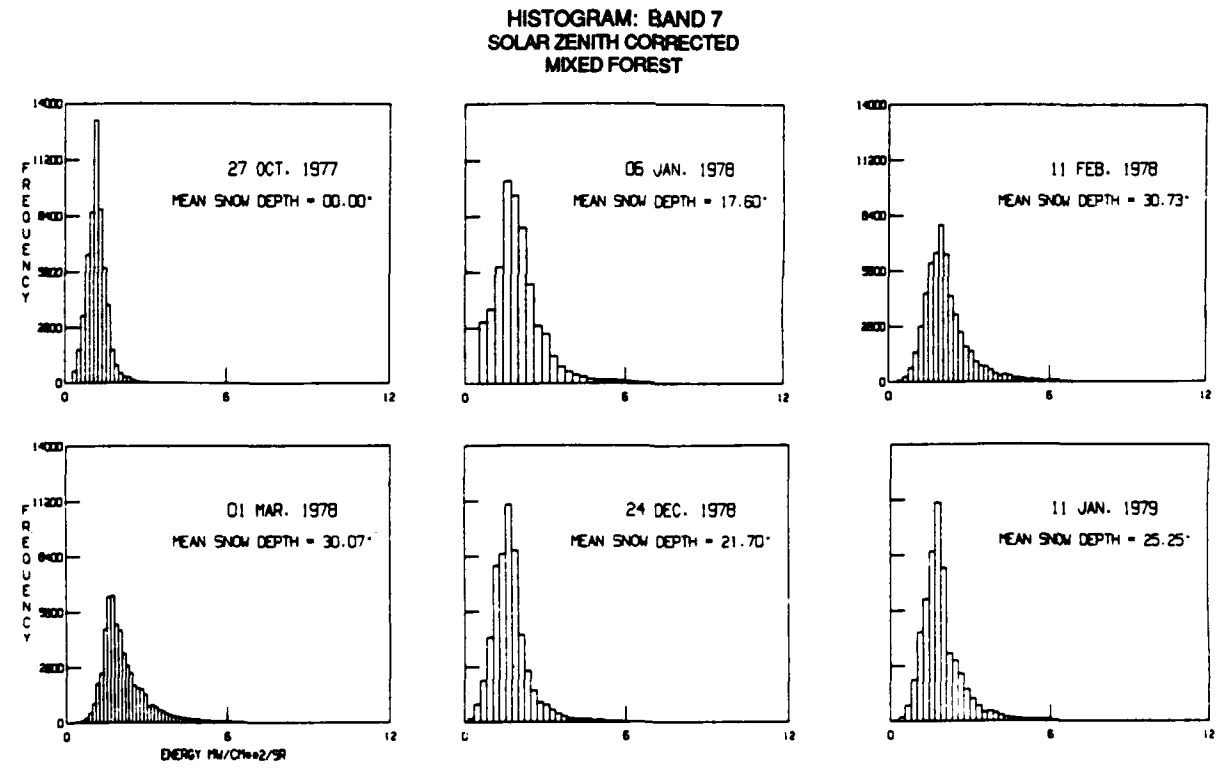


*b. MSS band 7.*

*Figure 19. Landsat histograms (corrected) for the mixed forest class.*

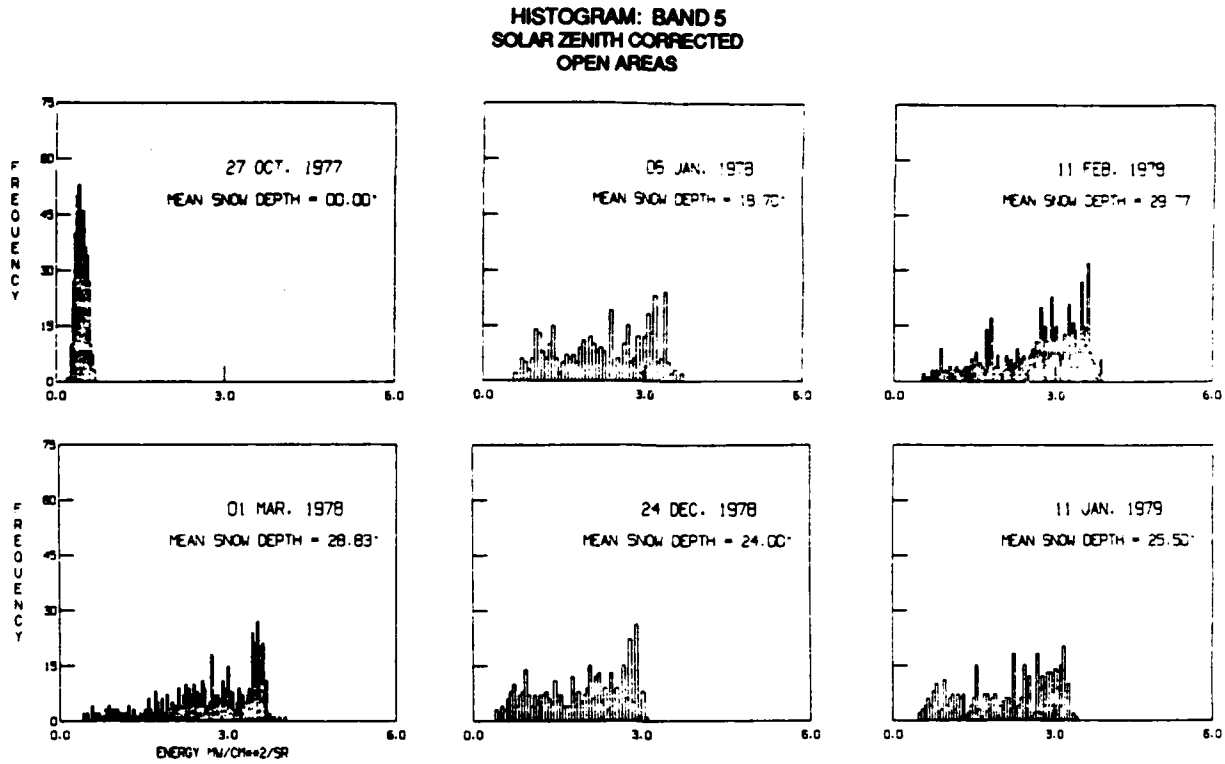


*a. MSS band 5.*

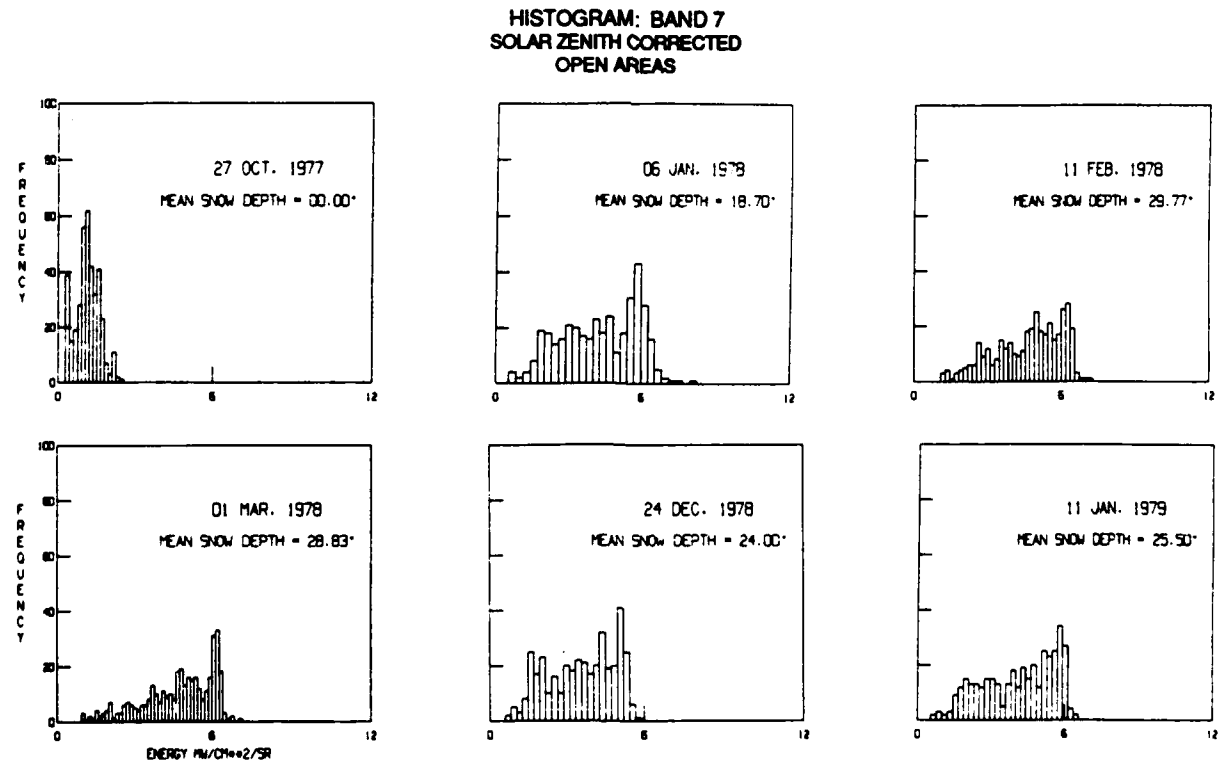


*b. MSS band 7.*

***Figure 20. Landsat histograms (corrected) for the open areas class.***

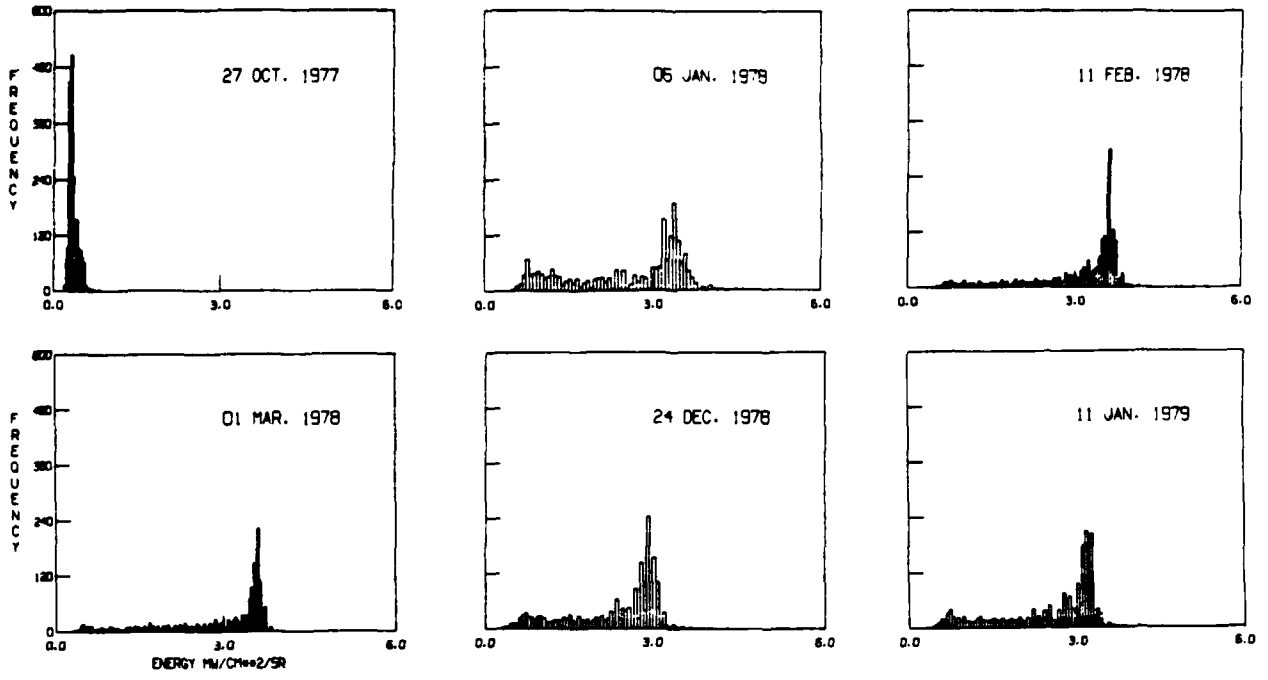


*a. MSS band 5.*

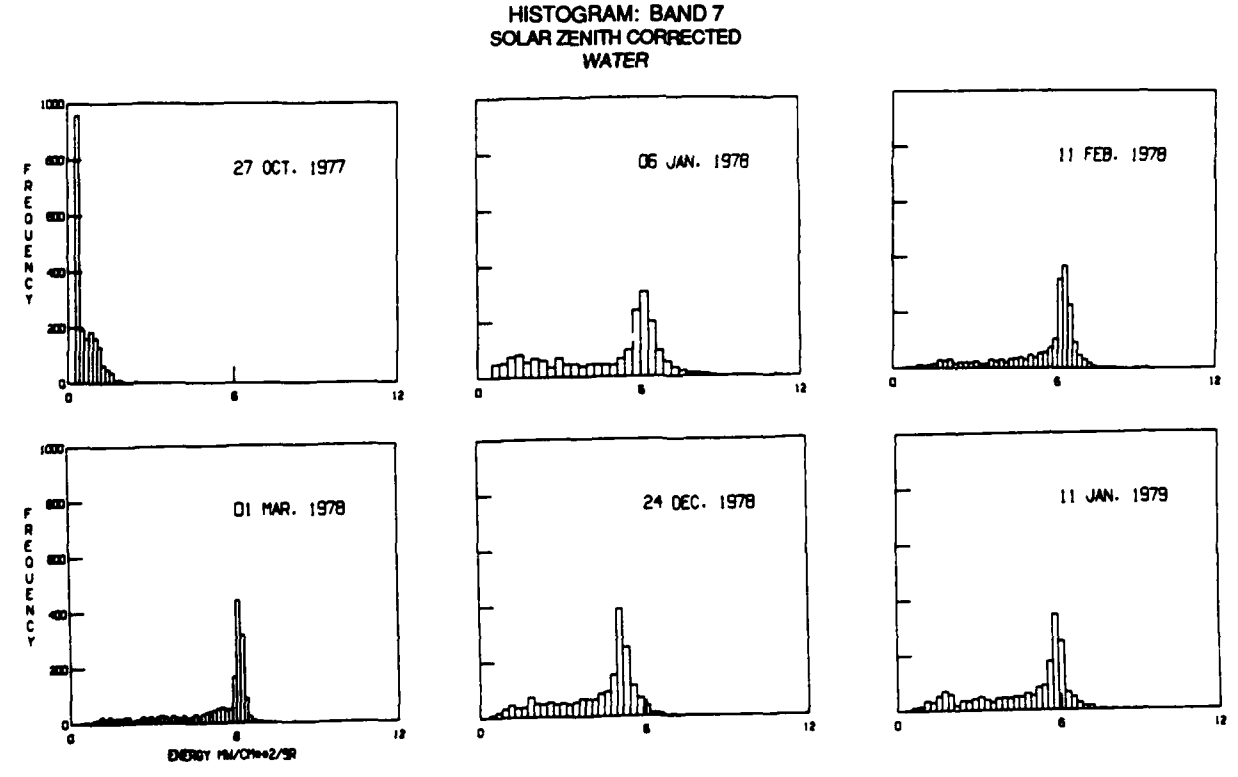


*b. MSS band 7.*

***Figure 21. Landsat histograms (corrected) for the water class.***

**Table 5. Satellite parameters used in the correction of Landsat data.**

| Date | Gain | | Offset | | Cosine of solar zenith angle |
|---|---|---|---|---|---|
| | MSS 5 | MSS 7 | MSS 5 | MSS 7 | |
| 27 Oct 77 | 0.0134 | 0.0603 | 0.06 | 0.11 | 0.3907 |
| 6 Jan 78 | 0.0134 | 0.0603 | 0.06 | 0.11 | 0.2079 |
| 11 Feb 78 | 0.0134 | 0.0603 | 0.06 | 0.11 | 0.3256 |
| 1 Mar 78 | 0.0134 | 0.0603 | 0.06 | 0.11 | 0.4384 |
| 31 May 78 | — | — | — | — | — |
| 24 Dec 78 | 0.0139 | 0.0603 | 0.03 | 0.03 | 0.2588 |
| 11 Jan 79 | 0.0139 | 0.0603 | 0.03 | 0.03 | 0.2756 |

angle of the various Landsat scenes resulted in unequal radiance levels between consecutive count values for each scene. For example, changes in one count value in the MSS 7 uncorrected data for 6 Jan 78 and 1 Mar 78 resulted in radiance changes of 0.29 and 0.138 mW $cm^{-2}$/sr, respectively.

A resampling scheme was applied to correct for this radiance interval variation. The histograms were resampled to the energy levels of 6 Jan 78, the Landsat date with the lowest solar elevation angle. For 6 Jan 78 the following energy values correspond to the MSS 7 count levels:

MSS 7 count level:

| 0 | 1 | 2 | 3 | 4 | ... | 63 |
|---|---|---|---|---|---|---|

Radiance (mW $cm^{-2}$/sr):

| 0.53 | 0.82 | 1.11 | 1.40 | 1.69 | ... | 18.80 |
|---|---|---|---|---|---|---|

For example, for the 1 Mar 78 scene, count level 5 corresponds to a radiance value of 0.94 and has a pixel population of 1750. Count level 5 is then resampled by weighting between levels 0.82 and 1.11 mW $cm^{-2}$/sr and the pixel population is calculated using the following two equations:

$$pop_{0.82} = 1750 * \frac{1.11-0.94}{1.11-0.82} = 1026 \quad (12)$$

$$pop_{1.11} = 1750 * \frac{0.94-0.82}{1.11-0.82} = 724. \quad (13)$$

This procedure is repeated for each count level of the corrected histogram to derive the resampled histogram.

Figures 22 through 27 show the corrected and resampled histograms for MSS bands 5 and 7 for the total study area and the individual land cover classes. Within each land cover class for both bands there is a strong similarity in the histograms on all snow-covered days.

Histograms for the corrected and resampled MSS 7 data for the total area and the forested classes did not change significantly with changes in the accumulated snow depth (Fig. 22–25). A quantitative evaluation of the histograms was made and the results are shown in Tables 6 and 7. Statistics on the mean, median, mode, standard deviation, first and third quartile, 10th and 90th percentile, five indices of skewness, and three indices of kurtosis are presented. The radiance intervals between histogram levels are equal to 0.064 and 0.29 mW $cm^{-2}$/sr for MSS bands 5 and 7, respectively. For the five snow days shown, three were observed with Landsat-2 (6 Jan 78, 11 Feb 78, and 1 Mar 78), while two days were observed with the Landsat-3 satellite (24 Dec 78 and 11 Jan 79). Although differences in sensor gain and offset were taken into consideration during the correction process, the Landsat-3 observations show larger energy values.

Table 8 shows the average snow depth for each land cover class and the total. These values were determined from the snow course measurements taken during the time of the Landsat overpasses.

The 31 May land cover classification was used to provide a mask with which the histograms of Landsat data could be evaluated for each of the land cover classes. Histograms for the forested landscapes, which predominate in the region, display characteristics similar to the total areas (Fig. 22–25).

The histogram statistics for the three forest types and the total area are similar for the three winter Landsat-2 dates (Tables 6, 7). The measures of central tendency (mode) and the standard deviation ($s$) are similar. Means, quartiles, and percentiles show differences between scenes less than the radiance intervals between histogram

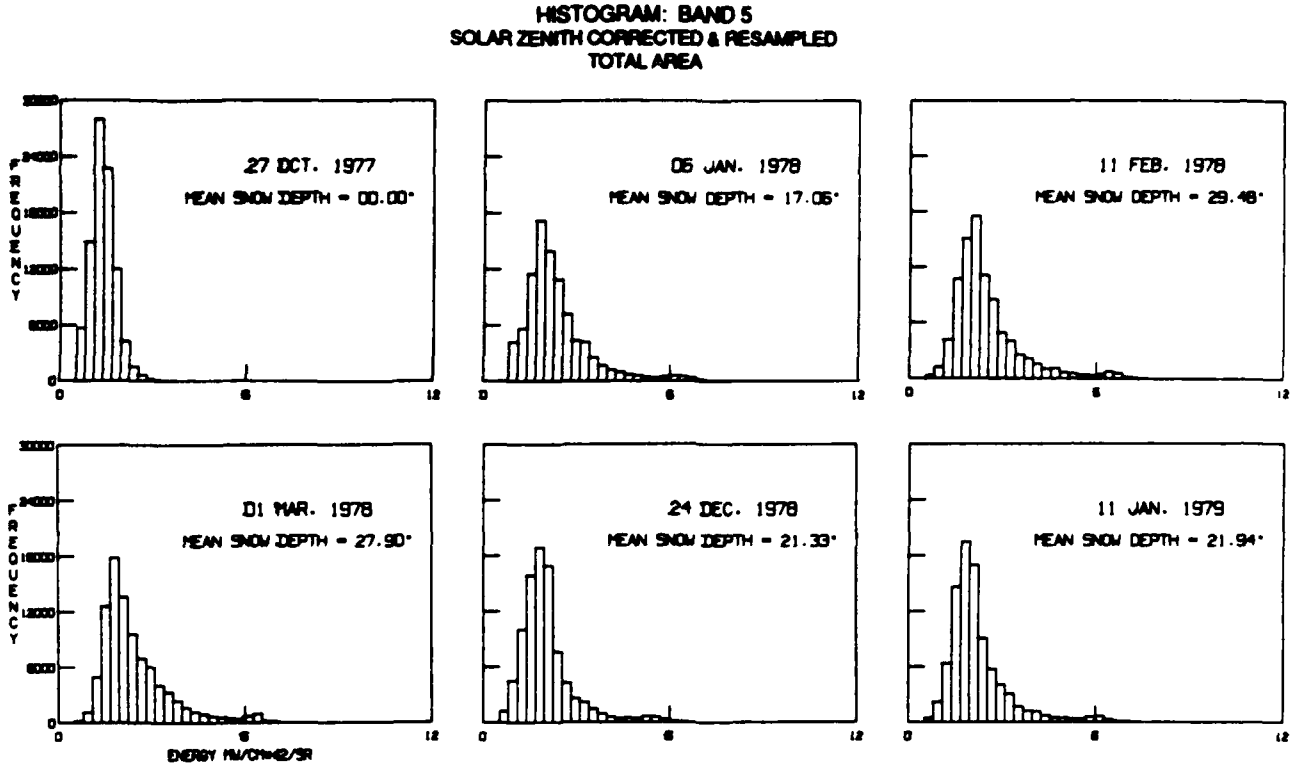


*a. MSS band 5.*

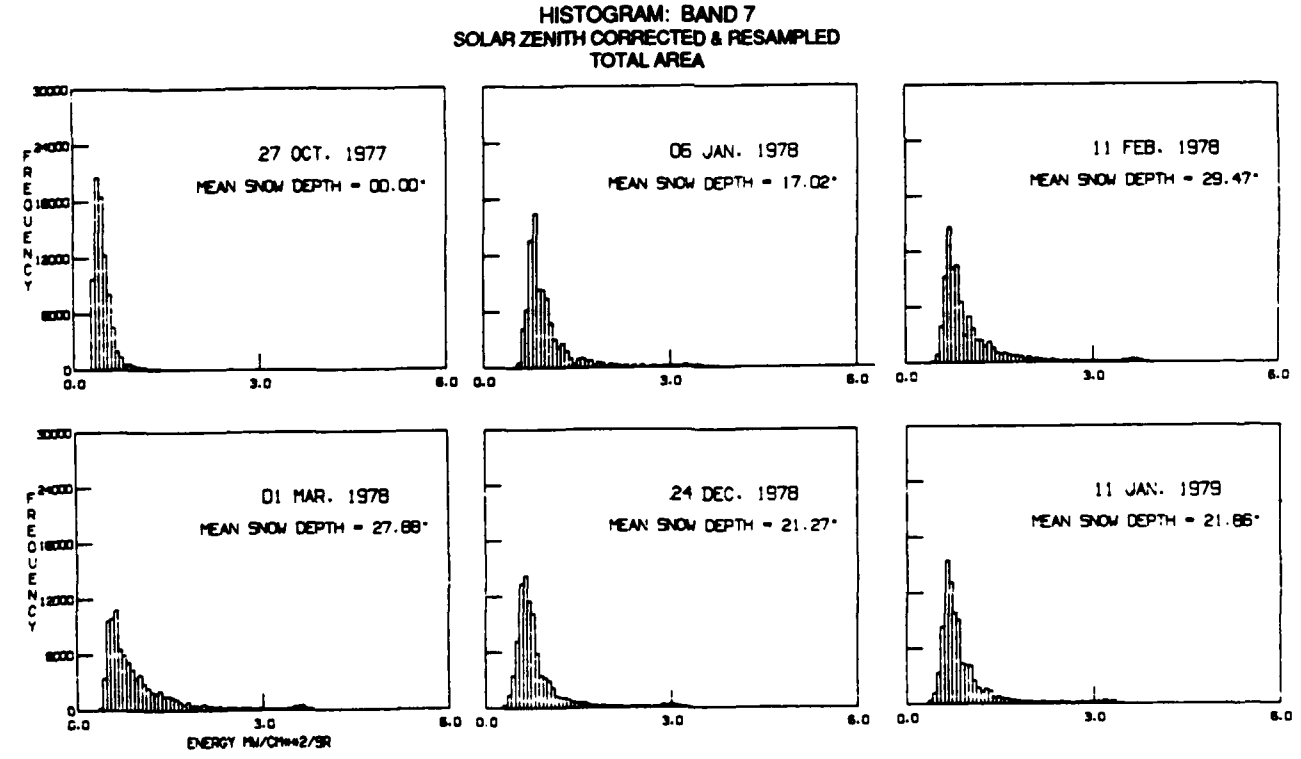


*b. MSS band 7.*

***Figure 22. Landsat histograms (corrected and resampled) for the total 300- × 300-pixel area located near Allagash, Maine.***

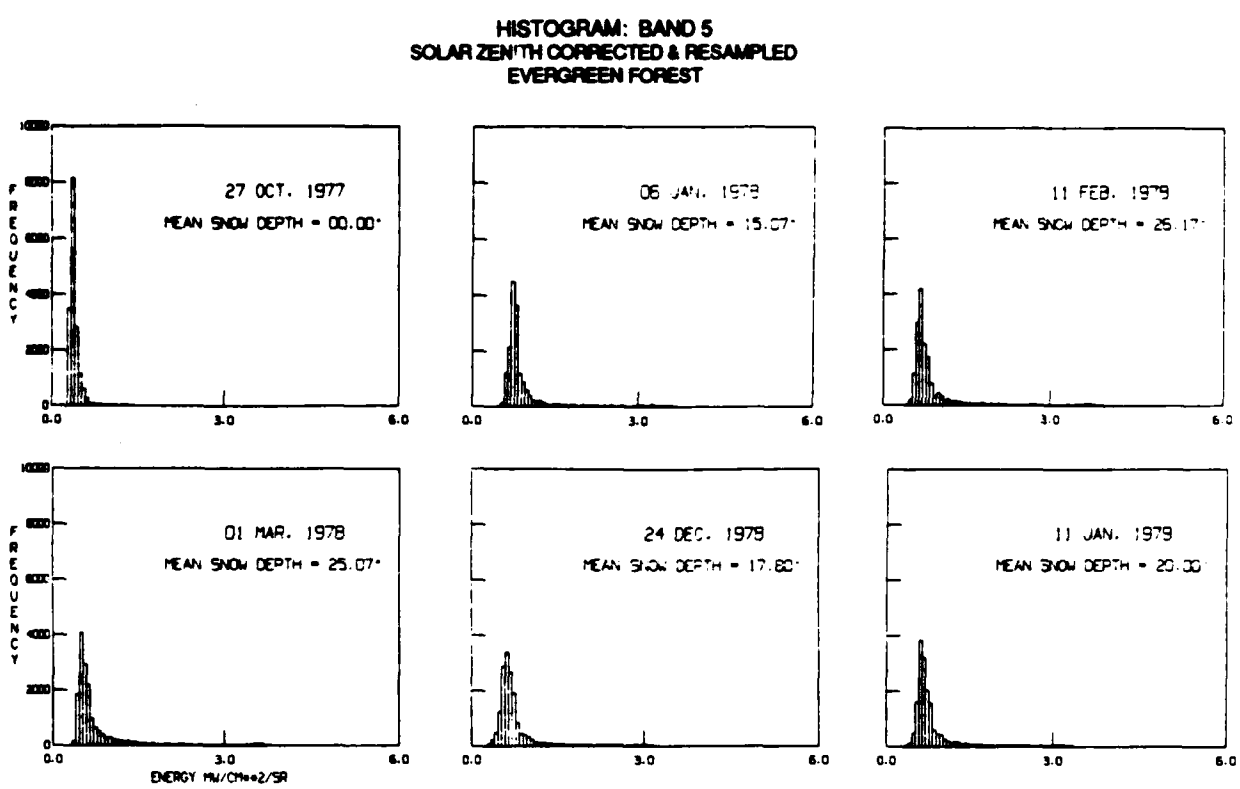


*a. MSS band 5.*

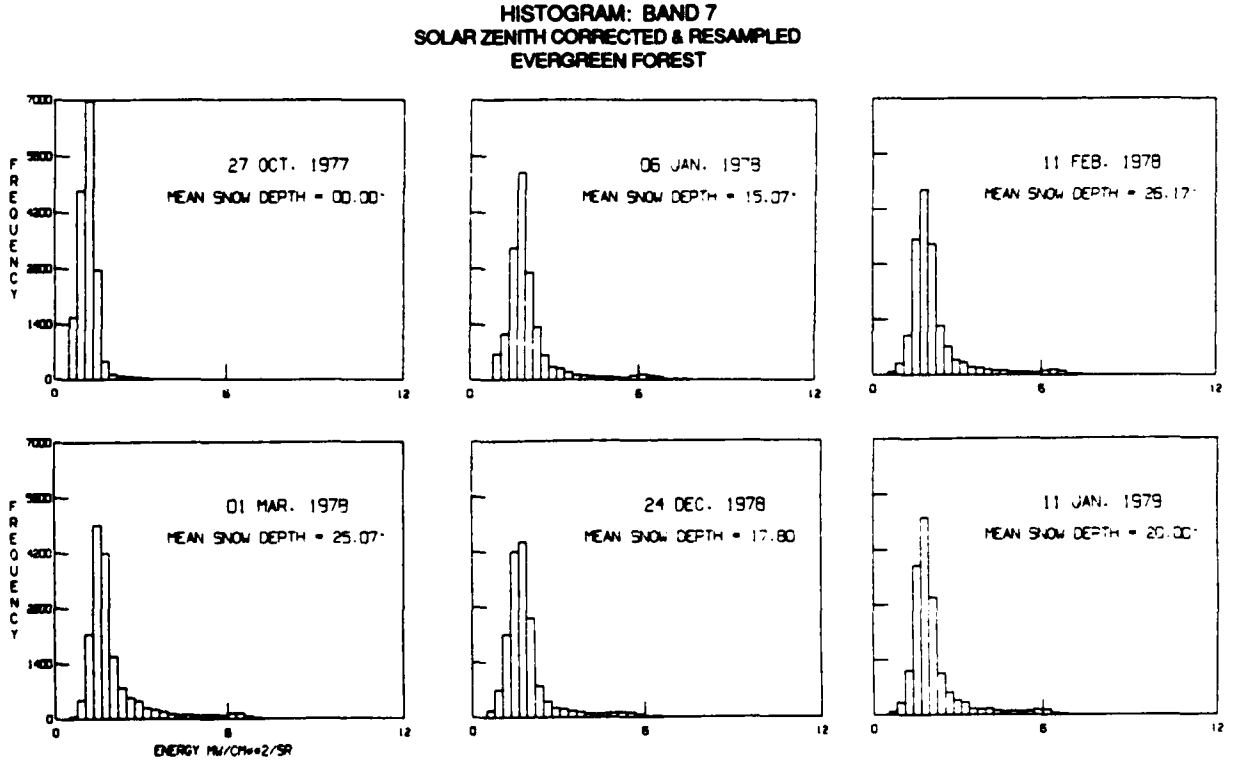


*b. MSS band 7.*

***Figure 23. Landsat histograms (corrected and resampled) for the softwoods class.***

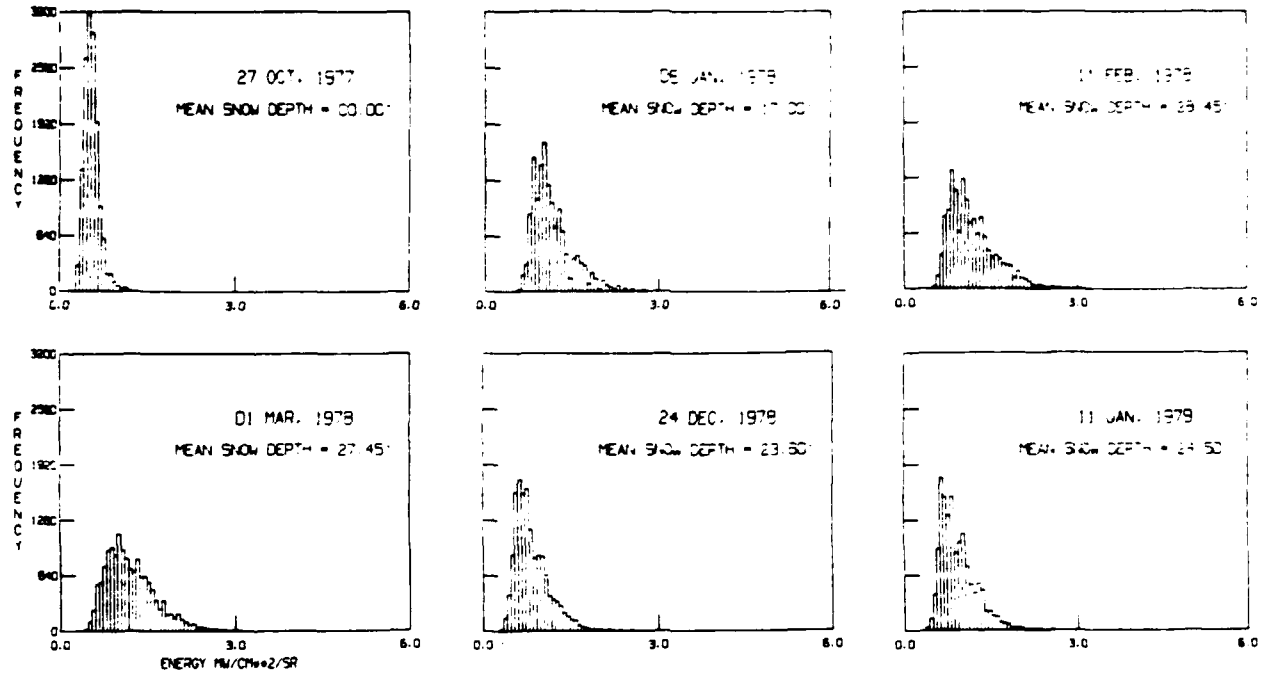


*a. MSS band 5.*

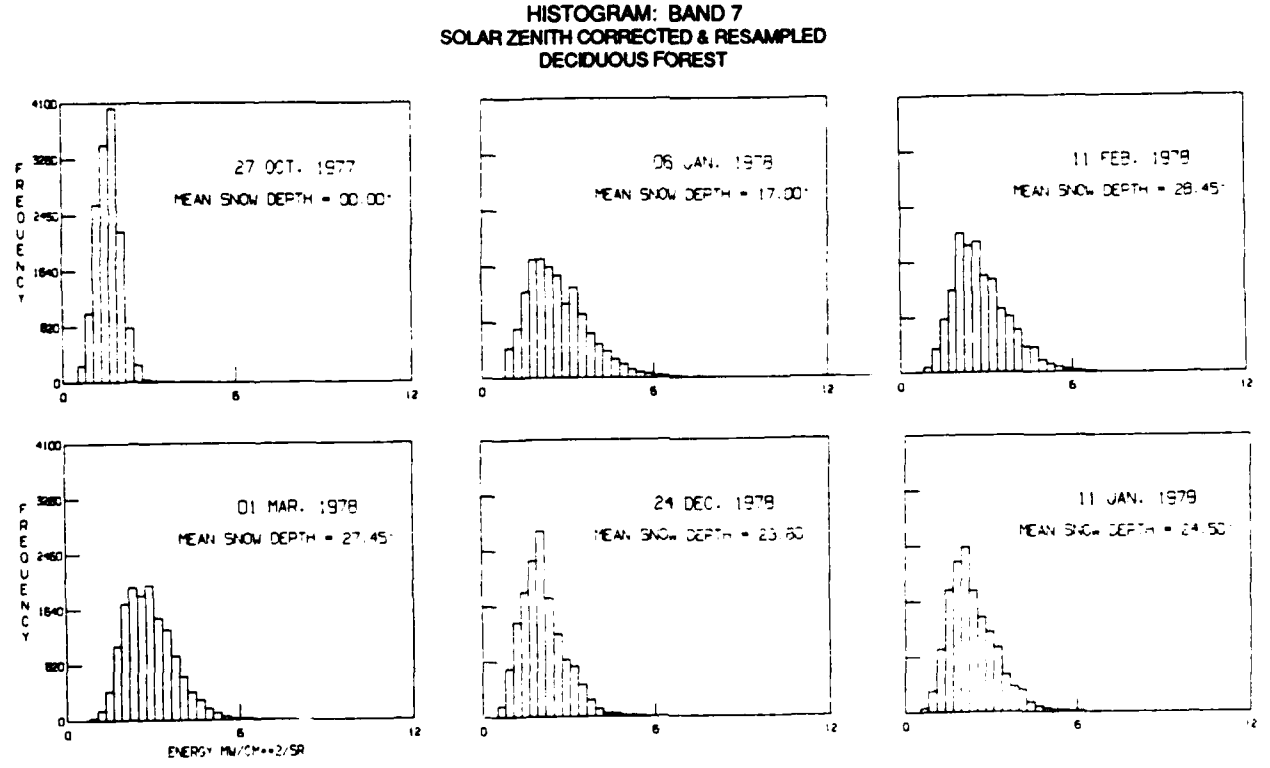


*b. MSS band 7.*

***Figure 24. Landsat histograms (corrected and resampled) for the hardwoods class.***

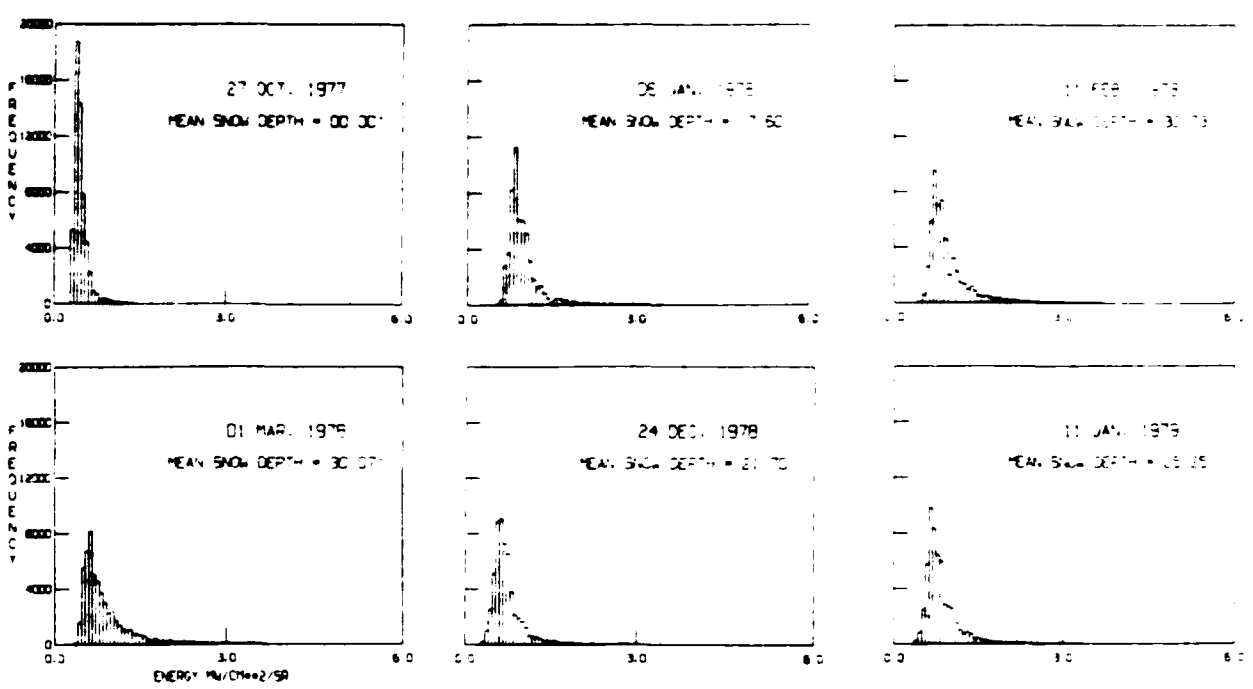


*a. MSS band 5.*

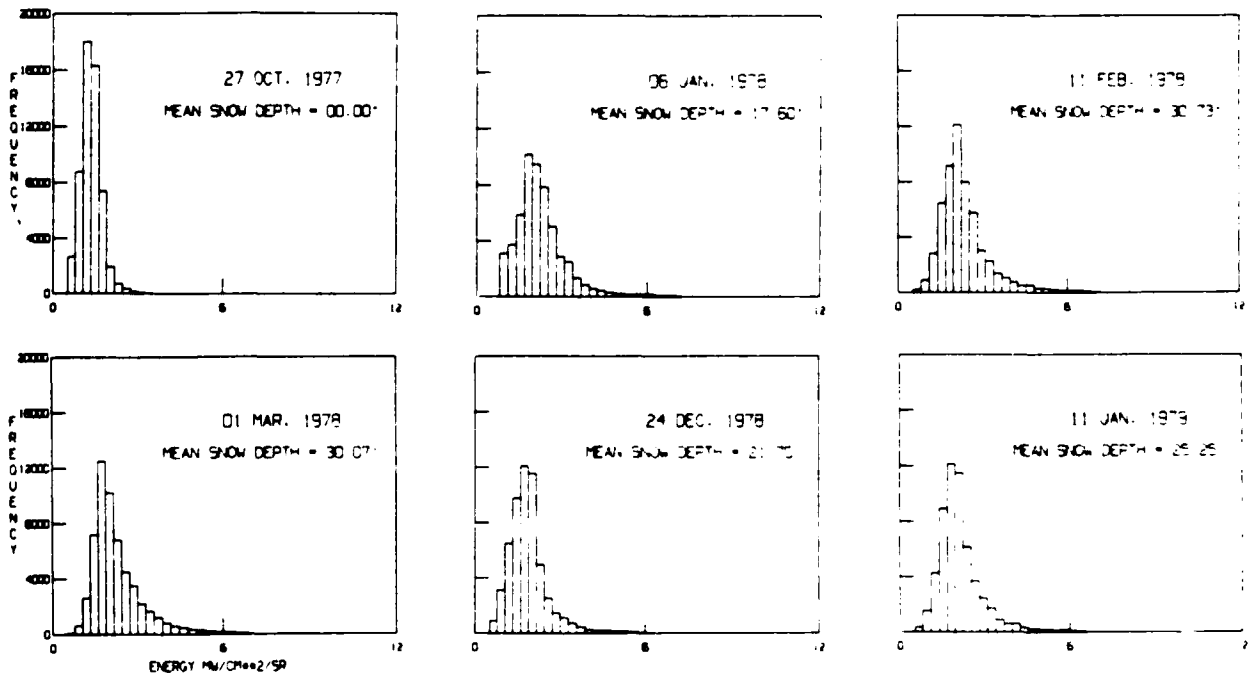


*b. MSS band 7.*

***Figure 25. Landsat histograms (corrected and resampled) for the mixed forest class.***

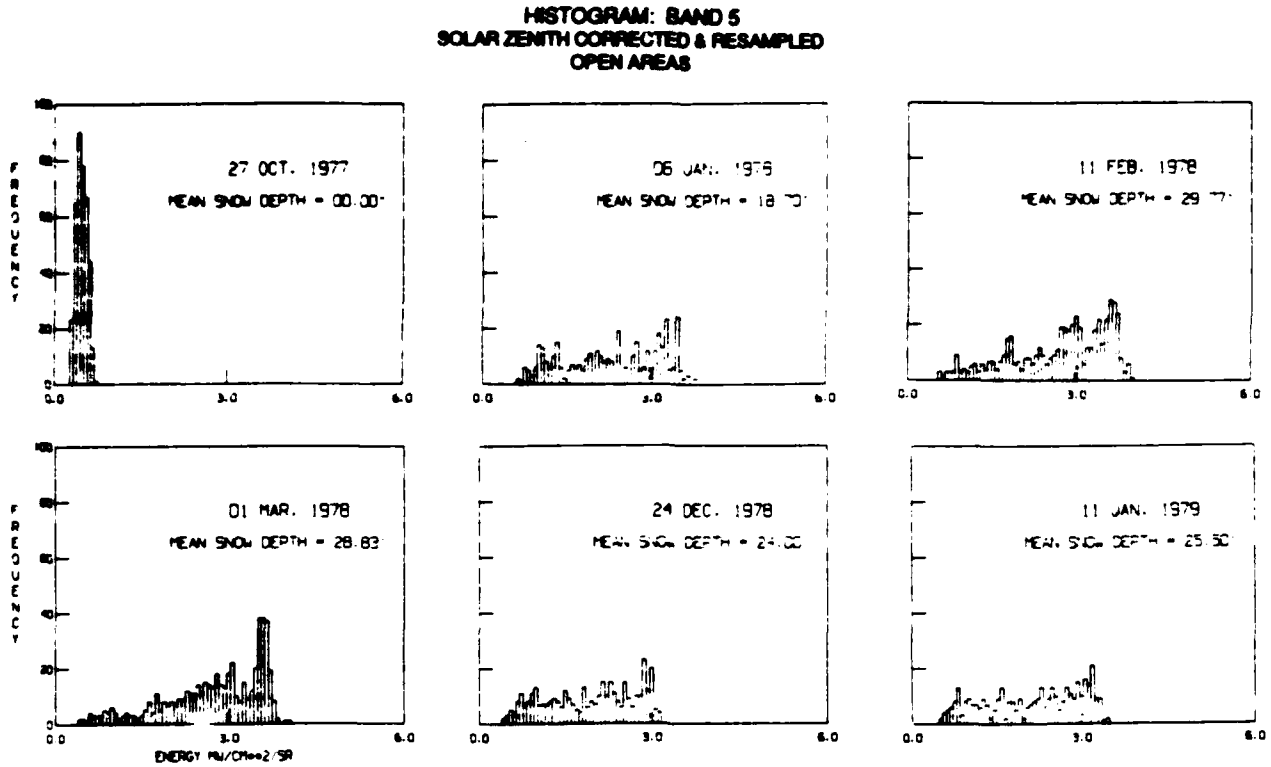


*a. MSS band 5.*

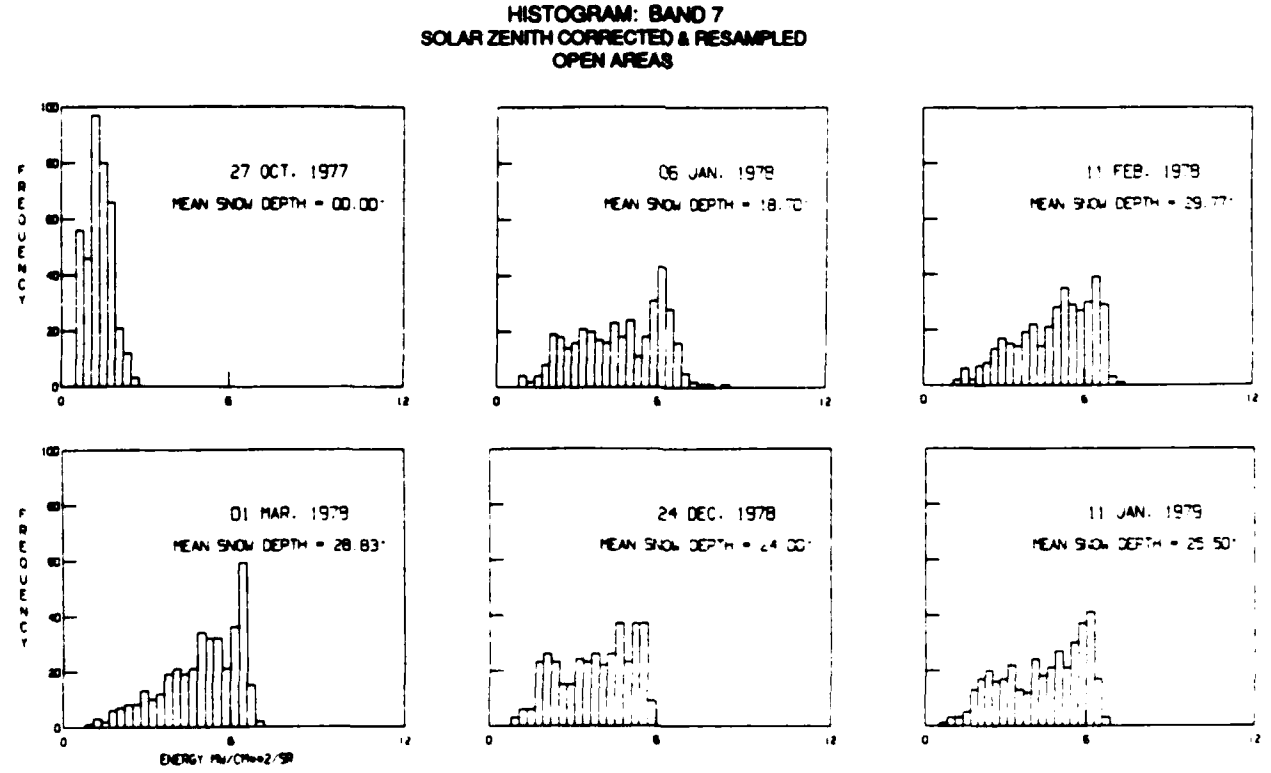


*b. MSS band 7.*

***Figure 26. Landsat histograms (corrected and resampled) for the open areas class.***

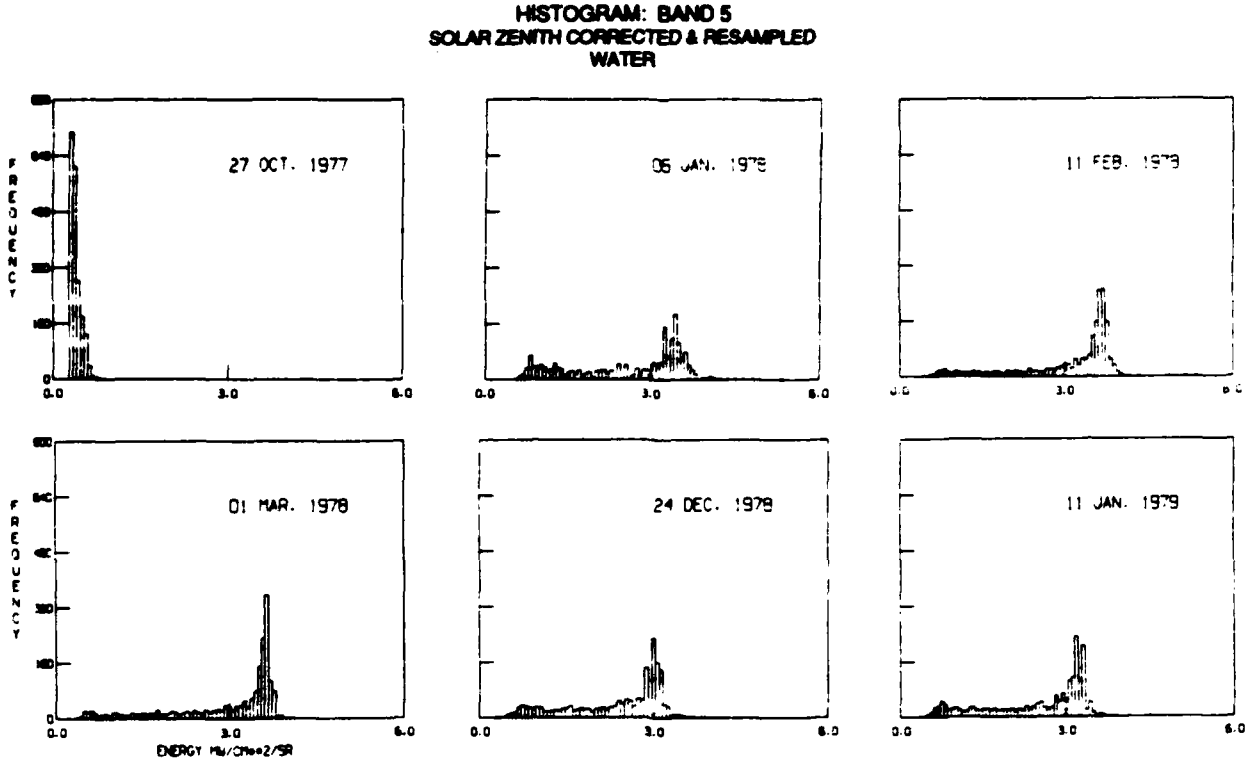


*a. MSS band 5.*

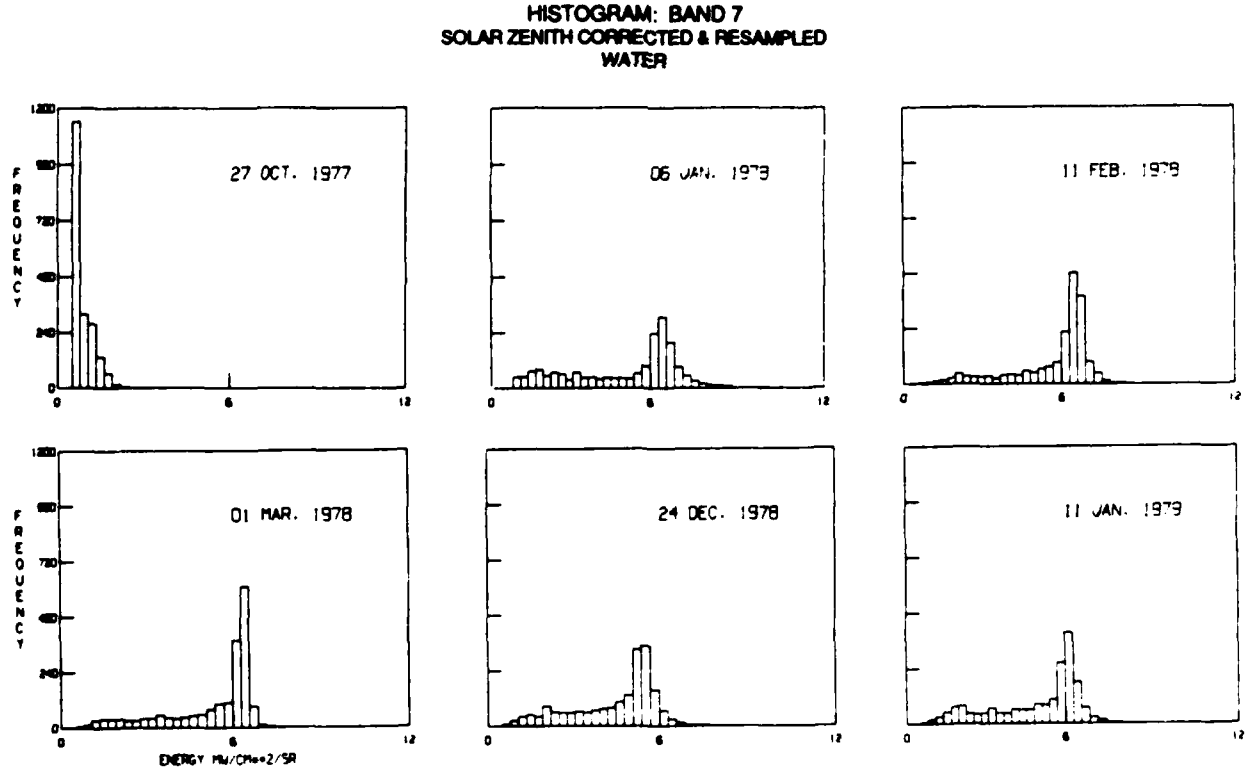


*b. MSS band 7.*

***Figure 27. Landsat histograms (corrected and resampled) for the water class.***

**Table 6. Statistics of MSS band 5 histograms. Data have been converted to radiance values (mW cm$^{-2}$/sr), corrected for sun angle effects, and resampled to equal intervals.**

| Statistic | Landsat-2 | | | | | Landsat-3 | |
|---|---|---|---|---|---|---|---|
| | 27 Oct 77 | 6 Jan 78 | 11 Feb 78 | 1 Mar 78 | 31 May 78 | 24 Dec 78 | 11 Jan 79 |
| **a. Total area** | | | | | | | |
| $\bar{X}$ | 0.43 | 1.01 | 1.00 | 0.96 | 0.35 | 0.79 | 0.86 |
| $Q2$ | 0.37 | 0.83 | 0.77 | 0.71 | 0.32 | 0.63 | 0.69 |
| Mode | 0.35 | 0.80 | 0.67 | 0.60 | 0.35 | 0.60 | 0.60 |
| $s$ | 0.14 | 0.48 | 0.58 | 0.62 | 0.04 | 0.44 | 0.47 |
| $Q1$ | 0.31 | 0.72 | 0.64 | 0.54 | 0.30 | 0.53 | 0.58 |
| $Q3$ | 0.46 | 1.02 | 1.06 | 1.08 | 0.34 | 0.80 | 0.90 |
| $P10$ | 0.28 | 0.65 | 0.57 | 0.45 | 0.28 | 0.45 | 0.51 |
| $P90$ | 0.56 | 1.43 | 1.59 | 1.63 | 0.36 | 1.15 | 1.26 |
| Skew$^1$ | 0.63 | 0.43 | 0.58 | 0.57 | 0.04 | 0.42 | 0.55 |
| Skew$^2$ | 1.45 | 1.11 | 1.21 | 1.19 | 2.80 | 1.06 | 1.11 |
| Skew$^3$ | 0.23 | 0.30 | 0.38 | 0.35 | 0.00 | 0.21 | 0.31 |
| Skew$^4$ | 0.37 | 0.55 | 0.61 | 0.55 | 0.03 | 0.47 | 0.52 |
| Skew (Moment) | 2.30 | 3.15 | 2.71 | 2.29 | 1.52 | 3.08 | 3.02 |
| Kurtosis$^1$ | 0.26 | 0.19 | 0.20 | 0.23 | 0.25 | 0.19 | 0.21 |
| Kurtosis (Moment) | 11.78 | 14.72 | 11.23 | 8.91 | 12.80 | 14.19 | 13.56 |
| Kurtosis (Mode) | 0.32 | 0.18 | 0.16 | 0.12 | 0.77 | 0.16 | 0.17 |
| **b. Softwoods** | | | | | | | |
| $\bar{X}$ | 0.38 | 0.92 | 0.89 | 0.78 | 0.35 | 0.77 | 0.83 |
| $Q2$ | 0.32 | 0.74 | 0.67 | 0.53 | 0.32 | 0.61 | 0.65 |
| Mode | 0.35 | 0.73 | 0.67 | 0.48 | 0.35 | 0.60 | 0.60 |
| $s$ | 0.11 | 0.49 | 0.56 | 0.62 | 0.04 | 0.45 | 0.48 |
| $Q1$ | 0.29 | 0.68 | 0.60 | 0.45 | 0.29 | 0.53 | 0.57 |
| $Q3$ | 0.37 | 0.85 | 0.80 | 0.71 | 0.34 | 0.72 | 0.78 |
| $P10$ | 0.25 | 0.61 | 0.55 | 0.40 | 0.26 | 0.46 | 0.52 |
| $P90$ | 0.45 | 1.21 | 1.30 | 1.33 | 0.36 | 1.07 | 1.20 |
| Skew$^1$ | 0.26 | 0.38 | 0.39 | 0.49 | 0.00 | 0.36 | 0.47 |
| Skew$^2$ | 1.51 | 1.08 | 1.17 | 1.22 | 2.40 | 1.07 | 1.13 |
| Skew$^3$ | 0.18 | 0.28 | 0.35 | 0.40 | 0.00 | 0.18 | 0.26 |
| Skew$^4$ | 0.28 | 0.58 | 0.69 | 0.73 | -0.08 | 0.52 | 0.61 |
| Skew (Moment) | 4.15 | 3.51 | 3.31 | 3.00 | 1.98 | 3.22 | 3.21 |
| Kurtosis$^1$ | 0.20 | 0.14 | 0.13 | 0.14 | 0.22 | 0.16 | 0.15 |
| Kurtosis (Moment) | 30.92 | 15.84 | 14.41 | 12.08 | 15.68 | 14.17 | 13.90 |
| Kurtosis (Mode) | 0.49 | 0.27 | 0.25 | 0.24 | 0.73 | 0.20 | 0.23 |

Explanation:

$$\text{Skew}^1 = \frac{(\bar{X}\text{-mode})}{s} \qquad \text{Skew}^2 = \frac{3(\bar{X}-Q2)}{s} \qquad \text{Skew}^3 = \frac{Q3-2Q2+Q1}{Q3-Q1}$$

$$\text{Skew}^4 = \frac{P90-2Q2+P10}{P90-P10} \qquad \text{Skew (Moment)} = \frac{(\bar{X}_j-X)^3}{N(s^3)}$$

$$\text{Kurtosis}^1 = \frac{0.5(Q3-Q1)}{P90-P10} \qquad \text{Kurtosis (Moment)} = \frac{(\bar{X}_j-X)^4}{N(s^4)}$$

$$\text{Kurtosis (Mode)} = \frac{\text{Population (mode)}}{\text{Population (total)}}$$

where $X$ = mean, $s$ = standard deviation, $Q2$ = median, $Q1$ = first quartile, $Q3$ = third quartile, $P10$ = 10th percentile, $P90$ = 90th percentile.

**Table 6 (cont'd). Statistics of MSS band 5 histograms.**

| Statistic | Landsat-2 | | | | | Landsat-3 | |
|---|---|---|---|---|---|---|---|
| | 27 Oct 77 | 6 Jan 78 | 11 Feb 78 | 1 Mar 78 | 31 May 78 | 24 Dec 78 | 11 Jan 79 |
| **c. Hardwoods** | | | | | | | |
| $\overline{X}$ | 0.52 | 1.12 | 1.15 | 1.19 | 0.36 | 0.81 | 0.89 |
| $Q2$ | 0.47 | 1.00 | 1.03 | 1.08 | 0.32 | 0.71 | 0.78 |
| Mode | 0.48 | 0.99 | 0.80 | 0.99 | 0.35 | 0.60 | 0.60 |
| $s$ | 0.14 | 0.35 | 0.42 | 0.43 | 0.04 | 0.29 | 0.32 |
| $Q1$ | 0.40 | 0.84 | 0.80 | 0.83 | 0.30 | 0.56 | 0.62 |
| $Q3$ | 0.56 | 1.24 | 1.34 | 1.40 | 0.34 | 0.93 | 1.01 |
| $P10$ | 0.34 | 0.73 | 0.67 | 0.67 | 0.29 | 0.48 | 0.54 |
| $P90$ | 0.66 | 1.57 | 1.71 | 1.74 | 0.36 | 1.18 | 1.27 |
| Skew$^1$ | 0.33 | 0.37 | 0.85 | 0.47 | 0.15 | 0.69 | 0.89 |
| Skew$^2$ | 1.08 | 1.03 | 0.90 | 0.77 | 2.88 | 1.04 | 1.02 |
| Skew$^3$ | 0.05 | 0.21 | 0.15 | 0.14 | 0.00 | 0.23 | 0.18 |
| Skew$^4$ | 0.16 | 0.38 | 0.32 | 0.24 | 0.16 | 0.35 | 0.34 |
| Skew (Moment) | 1.37 | 1.64 | 1.17 | 0.91 | 9.63 | 1.36 | 1.51 |
| Kurtosis$^1$ | 0.25 | 0.24 | 0.26 | 0.27 | 0.26 | 0.26 | 0.27 |
| Kurtosis (Moment) | 7.28 | 9.79 | 4.82 | 3.98 | 11.91 | 6.35 | 7.80 |
| Kurtosis (Mode) | 0.22 | 0.12 | 0.09 | 0.08 | 0.81 | 0.12 | 0.12 |
| **d. Mixed forest** | | | | | | | |
| $\overline{X}$ | 0.43 | 0.94 | 0.92 | 0.87 | 0.35 | 0.72 | 0.80 |
| $Q2$ | 0.37 | 0.81 | 0.75 | 0.68 | 0.32 | 0.62 | 0.67 |
| Mode | 0.35 | 0.80 | 0.67 | 0.60 | 0.35 | 0.60 | 0.60 |
| $s$ | 0.13 | 0.35 | 0.43 | 0.48 | 0.03 | 0.31 | 0.35 |
| $Q1$ | 0.32 | 0.72 | 0.64 | 0.54 | 0.30 | 0.51 | 0.57 |
| $Q3$ | 0.44 | 0.97 | 0.97 | 0.96 | 0.34 | 0.76 | 0.85 |
| $P10$ | 0.29 | 0.65 | 0.57 | 0.46 | 0.28 | 0.44 | 0.50 |
| $P90$ | 0.54 | 1.21 | 1.35 | 1.42 | 0.35 | 1.01 | 1.13 |
| Skew$^1$ | 0.61 | 0.41 | 0.58 | 0.56 | 0.01 | 0.38 | 0.57 |
| Skew$^2$ | 1.43 | 1.08 | 1.16 | 1.19 | 3.06 | 1.02 | 1.09 |
| Skew$^3$ | 0.19 | 0.26 | 0.31 | 0.33 | 0.00 | 0.17 | 0.25 |
| Skew$^4$ | 0.36 | 0.41 | 0.52 | 0.53 | -0.03 | 0.37 | 0.44 |
| Skew (Moment) | 2.61 | 3.39 | 2.80 | 2.39 | 0.55 | 2.93 | 2.98 |
| Kurtosis$^1$ | 0.25 | 0.22 | 0.22 | 0.22 | 0.27 | 0.21 | 0.22 |
| Kurtosis (Moment) | 13.70 | 19.10 | 13.34 | 10.26 | 6.56 | 15.84 | 15.44 |
| Kurtosis (Mode) | 0.03 | 0.20 | 0.17 | 0.15 | 0.78 | 0.16 | 0.18 |
| **e. Open areas** | | | | | | | |
| $\overline{X}$ | 0.46 | 2.25 | 3.80 | 3.85 | 0.47 | 1.92 | 2.11 |
| $Q2$ | 0.42 | 2.24 | 2.40 | 2.48 | 0.45 | 1.97 | 2.22 |
| Mode | 0.41 | 3.41 | 3.54 | 3.54 | 0.48 | 2.84 | 3.16 |
| $s$ | 0.10 | 0.86 | 1.71 | 1.69 | 0.07 | 0.77 | 0.84 |
| $Q1$ | 0.35 | 1.41 | 1.71 | 1.86 | 0.40 | 1.20 | 1.35 |
| $Q3$ | 0.51 | 3.05 | 2.86 | 2.91 | 0.51 | 2.52 | 2.85 |
| $P10$ | 0.30 | 1.00 | 1.13 | 1.09 | 0.37 | 0.78 | 0.80 |
| $P90$ | 0.57 | 3.33 | 3.04 | 3.16 | 0.58 | 2.84 | 3.11 |
| Skew$^1$ | 0.49 | -1.34 | 0.16 | 0.18 | -0.15 | -1.20 | -1.25 |
| Skew$^2$ | 1.17 | 0.03 | 2.47 | 2.43 | 0.55 | -0.19 | -0.39 |
| Skew$^3$ | 0.09 | -0.02 | -0.20 | -0.19 | 0.09 | -0.16 | -0.16 |
| Skew$^4$ | 0.09 | -0.07 | -0.33 | -0.35 | 0.18 | -0.16 | -0.23 |
| Skew (Moment) | 0.19 | -0.17 | -1.26 | -1.29 | 1.10 | -0.25 | -0.30 |
| Kurtosis$^1$ | 0.28 | 0.35 | 0.30 | 0.25 | 0.27 | 0.32 | 0.33 |
| Kurtosis (Moment) | 2.30 | 1.69 | 1.76 | 1.88 | 3.20 | 1.77 | 1.79 |
| Kurtosis (Mode) | 0.24 | 0.06 | 0.08 | 0.10 | 0.33 | 0.06 | 0.06 |

**Table 6 (cont'd). Statistics of MSS band 5 histograms. Data have been converted to radiance values (mW cm$^{-2}$/sr), corrected for sun angle effects, and resampled to equal intervals.**

| | *Landsat-2* | | | | | *Landsat-3* | |
|---|---|---|---|---|---|---|---|
| *Statistic* | *27 Oct 77* | *6 Jan 78* | *11 Feb 78* | *1 Mar 78* | *31 May 78* | *24 Dec 78* | *11 Jan 79* |
| | | | | **f. Water** | | | |
| $\bar{X}$ | 0.37 | 2.57 | 3.07 | 2.92 | 0.35 | 2.33 | 2.46 |
| *Q*2 | 0.31 | 3.03 | 3.45 | 3.38 | 0.31 | 2.66 | 2.83 |
| Mode | 0.29 | 3.41 | 3.67 | 3.60 | 0.35 | 2.97 | 3.16 |
| *s* | 0.09 | 1.02 | 0.87 | 0.93 | 0.06 | 0.81 | 0.89 |
| *Q*1 | 0.27 | 1.55 | 2.74 | 2.46 | 0.28 | 1.70 | 1.76 |
| *Q*3 | 0.38 | 3.37 | 3.61 | 3.55 | 0.34 | 2.94 | 3.13 |
| *P*10 | 0.24 | 0.92 | 1.52 | 1.27 | 0.25 | 0.92 | 0.91 |
| *P*90 | 0.47 | 3.54 | 3.70 | 3.61 | 0.39 | 3.05 | 3.25 |
| Skew$^1$ | 0.92 | -0.33 | -0.69 | -0.73 | 0.03 | -0.78 | -0.78 |
| Skew$^2$ | 1.80 | -1.38 | -1.32 | -1.48 | 1.90 | -1.22 | -1.24 |
| Skew$^3$ | 0.18 | -0.63 | -0.63 | -0.69 | -0.02 | -0.55 | -0.56 |
| Skew$^4$ | 0.36 | -0.61 | -0.77 | -0.81 | 0.08 | -0.64 | -0.64 |
| Skew (Moment) | 1.26 | -0.56 | -1.40 | -1.29 | 1.83 | -0.83 | -0.82 |
| Kurtosis$^1$ | 0.25 | 0.35 | 0.20 | 0.23 | 0.20 | 0.29 | 0.29 |
| Kurtosis (Moment) | 4.52 | 1.86 | 3.91 | 3.42 | 8.88 | 2.36 | 2.30 |
| Kurtosis (Mode) | 0.36 | 0.10 | 0.13 | 0.18 | 0.55 | 0.12 | 0.12 |

**Table 7. Statistics of MSS band 7 histograms. Data have been converted to radiance values (mW cm$^{-2}$/sr), corrected for sun angle effects, and resampled to equal intervals.**

| | *Landsat-2* | | | | | *Landsat-3* | |
|---|---|---|---|---|---|---|---|
| *Statistic* | *27 Oct 77* | *6 Jan 78* | *11 Feb 78* | *1 Mar 78* | *31 May 78* | *24 Dec 78* | *11 Jan 79* |
| | | | | **a. Total area** | | | |
| $\bar{X}$ | 1.24 | 2.29 | 2.32 | 2.30 | 1.90 | 1.88 | 2.07 |
| *Q*2 | 1.06 | 1.80 | 1.89 | 1.85 | 1.72 | 1.59 | 1.71 |
| Mode | 1.10 | 1.67 | 1.96 | 1.67 | 1.67 | 1.67 | 1.67 |
| *s* | 0.40 | 1.07 | 1.08 | 1.07 | 0.52 | 0.86 | 0.95 |
| *Q*1 | 0.83 | 1.40 | 1.50 | 1.45 | 1.37 | 1.22 | 1.36 |
| *Q*3 | 1.34 | 2.41 | 2.50 | 2.57 | 2.14 | 1.96 | 2.20 |
| *P*10 | 0.59 | 1.05 | 1.19 | 1.16 | 1.14 | 0.90 | 1.10 |
| *P*90 | 1.62 | 3.30 | 3.51 | 3.52 | 2.48 | 2.72 | 3.02 |
| Skew$^1$ | 0.35 | 0.49 | 0.33 | 0.58 | 0.44 | 0.25 | 0.42 |
| Skew$^2$ | 1.33 | 1.11 | 1.19 | 1.25 | 1.05 | 1.03 | 1.16 |
| Skew$^3$ | 0.09 | 0.20 | 0.21 | 0.28 | 0.10 | 0.01 | 0.18 |
| Skew$^4$ | 0.08 | 0.33 | 0.39 | 0.42 | 0.14 | 0.25 | 0.37 |
| Skew (Moment) | 0.60 | 1.91 | 1.84 | 1.65 | 0.09 | 1.93 | 2.03 |
| Kurtosis$^1$ | 0.25 | 0.22 | 0.21 | 0.24 | 0.29 | 0.20 | 0.22 |
| Kurtosis (Moment) | 3.88 | 8.05 | 7.14 | 6.12 | 2.73 | 8.33 | 8.39 |
| Kurtosis (Mode) | 0.31 | 0.19 | 0.20 | 0.20 | 0.21 | 0.21 | 0.22 |

Explanation:

$$\text{Skew}^1 = \frac{(\bar{X}\text{-mode})}{s} \qquad \text{Skew}^2 = \frac{3(\bar{X}-Q2)}{s} \qquad \text{Skew}^3 = \frac{Q3-2Q2+Q1}{Q3-Q1}$$

$$\text{Skew}^4 = \frac{P90-2Q2+P10}{P90-P10} \qquad \text{Skew (Moment)} = \frac{(\bar{X}_j-X)^3}{N(s^3)}$$

$$\text{Kurtosis}^1 = \frac{0.5(Q3-Q1)}{P90-P10} \qquad \text{Kurtosis (Moment)} = \frac{(\bar{X}_j-X)^4}{N(s^4)}$$

$$\text{Kurtosis (Mode)} = \frac{\text{Population (mode)}}{\text{Population (total)}}$$

where $X$ = mean, $s$ = standard deviation, $Q2$ = median, $Q1$ = first quartile, $Q3$ = third quartile, $P10$ = 10th percentile, $P90$ = 90th percentile.

**Table 7 (cont'd). Statistics of MSS band 7 histograms.**

| Statistic | Landsat-2 | | | | | Landsat-3 | |
|---|---|---|---|---|---|---|---|
| | *27 Oct 77* | *6 Jan 78* | *11 Feb 78* | *1 Mar 78* | *31 May 78* | *24 Dec 78* | *11 Jan 79* |
| **b. Softwoods** | | | | | | | |
| $\overline{X}$ | 1.04 | 1.94 | 2.00 | 1.88 | 1.32 | 1.77 | 1.93 |
| *Q*2 | 0.90 | 1.57 | 1.61 | 1.44 | 1.19 | 1.46 | 1.93 |
| Mode | 1.10 | 1.67 | 1.67 | 1.39 | 1.39 | 1.67 | 1.67 |
| *s* | 0.31 | 0.98 | 1.00 | 1.03 | 0.16 | 0.83 | 0.92 |
| *Q*1 | 0.68 | 1.31 | 1.34 | 1.19 | 1.07 | 1.18 | 1.30 |
| *Q*3 | 1.07 | 1.91 | 1.94 | 1.82 | 1.30 | 1.78 | 1.89 |
| *P*10 | 0.53 | 1.07 | 1.13 | 0.97 | 0.91 | 0.92 | 1.11 |
| *P*90 | 1.29 | 2.65 | 2.81 | 2.83 | 1.37 | 2.36 | 2.69 |
| Skew[1] | -0.17 | 0.27 | 0.33 | 0.48 | -0.41 | 0.12 | 0.28 |
| Skew[2] | 1.42 | 1.15 | 1.19 | 1.29 | 2.32 | 1.11 | 1.21 |
| Skew[3] | -0.11 | 0.14 | 0.11 | 0.20 | -0.08 | 0.06 | 0.12 |
| Skew[4] | 0.03 | 0.37 | 0.43 | 0.49 | -0.25 | 0.25 | 0.43 |
| Skew (Moment) | 1.12 | 2.82 | 2.68 | 2.53 | -0.23 | 2.52 | 2.60 |
| Kurtosis[1] | 0.26 | 0.19 | 0.18 | 0.17 | 0.26 | 0.21 | 0.19 |
| Kurtosis (Moment) | 7.57 | 12.44 | 11.22 | 9.82 | 3.66 | 10.83 | 10.73 |
| Kurtosis (Mode) | 0.42 | 0.31 | 0.28 | 0.29 | 0.66 | 0.27 | 0.30 |
| **c. Hardwoods** | | | | | | | |
| $\overline{X}$ | 1.52 | 2.52 | 2.68 | 2.78 | 2.70 | 1.99 | 2.20 |
| *Q*2 | 1.38 | 2.21 | 2.39 | 2.55 | 2.53 | 1.77 | 1.91 |
| Mode | 1.67 | 1.96 | 1.96 | 2.82 | 2.53 | 1.96 | 1.96 |
| *s* | 0.42 | 1.04 | 0.94 | 0.85 | 0.21 | 0.75 | 0.82 |
| *Q*1 | 1.08 | 1.59 | 1.85 | 2.00 | 2.38 | 1.32 | 1.46 |
| *Q*3 | 1.65 | 3.01 | 3.09 | 3.17 | 2.72 | 2.27 | 2.55 |
| *P*10 | 0.83 | 1.17 | 1.45 | 1.61 | 2.29 | 0.93 | 1.13 |
| *P*90 | 1.91 | 3.79 | 3.83 | 3.78 | 2.86 | 2.91 | 3.17 |
| Skew[1] | -0.37 | 0.53 | 0.76 | -0.05 | 0.77 | 0.04 | 0.29 |
| Skew[2] | 0.95 | 0.88 | 0.92 | 0.79 | 2.43 | 0.89 | 1.05 |
| Skew[3] | -0.08 | 0.13 | 0.12 | 0.06 | 0.13 | 0.05 | 0.17 |
| Skew[4] | -0.02 | 0.21 | 0.21 | 0.14 | 0.17 | 0.16 | 0.23 |
| Skew (Moment) | 0.10 | 0.87 | 0.74 | 0.58 | 0.46 | 0.75 | 0.89 |
| Kurtosis[1] | 0.27 | 0.27 | 0.26 | 0.27 | 0.30 | 0.24 | 0.27 |
| Kurtosis (Moment) | 2.96 | 4.62 | 3.61 | 3.29 | 2.76 | 4.20 | 4.47 |
| Kurtosis (Mode) | 0.27 | 0.12 | 0.14 | 0.14 | 0.48 | 0.19 | 0.17 |
| **d. Mixed forest** | | | | | | | |
| $\overline{X}$ | 1.24 | 2.06 | 2.19 | 2.18 | 1.91 | 1.79 | 1.98 |
| *Q*2 | 1.08 | 1.83 | 1.88 | 1.81 | 1.75 | 1.57 | 1.69 |
| Mode | 1.10 | 1.67 | 1.96 | 1.67 | 1.67 | 1.67 | 1.67 |
| *s* | 0.37 | 0.88 | 0.87 | 0.88 | 0.31 | 0.70 | 0.78 |
| *Q*1 | 0.85 | 1.42 | 1.50 | 1.47 | 1.52 | 1.20 | 1.35 |
| *Q*3 | 1.32 | 2.36 | 2.37 | 2.38 | 2.01 | 1.92 | 2.12 |
| *P*10 | 0.62 | 1.00 | 1.18 | 1.19 | 1.39 | 0.88 | 1.06 |
| *P*90 | 1.57 | 3.10 | 3.09 | 3.16 | 2.19 | 2.44 | 2.77 |
| Skew[1] | 0.39 | 0.44 | 0.27 | 0.58 | 0.78 | 0.17 | 0.39 |
| Skew[2] | 1.33 | 0.79 | 1.09 | 1.24 | 1.56 | 0.94 | 1.08 |
| Skew[3] | 0.05 | 0.13 | 0.14 | 0.24 | 0.05 | -0.03 | 0.11 |
| Skew[4] | 0.04 | 0.21 | 0.27 | 0.37 | 0.10 | 0.12 | 0.26 |
| Skew (Moment) | 0.62 | 1.79 | 1.72 | 1.68 | 0.15 | 1.57 | 1.75 |
| Kurtosis[1] | 0.25 | 0.22 | 0.23 | 0.23 | 0.30 | 0.28 | 0.23 |
| Kurtosis (Moment) | 4.42 | 8.53 | 7.83 | 6.98 | 2.26 | 7.96 | 8.16 |
| Kurtosis (Mode) | 0.32 | 0.18 | 0.22 | 0.22 | 0.32 | 0.22 | 0.22 |

**Table 7 (cont'd). Statistics of MSS band 7 histograms. Data have been converted to radiance values (mW $cm^{-2}/sr$), corrected for sun angle effects, and resampled to equal intervals.**

| | *Landsat-2* | | | | | *Landsat-3* | |
|---|---|---|---|---|---|---|---|
| *Statistic* | *27 Oct 77* | *6 Jan 78* | *11 Feb 78* | *1 Mar 78* | *31 May 78* | *24 Dec 78* | *11 Jan 79* |
| | | | **e. Open areas** | | | | |
| $\overline{X}$ | 1.23 | 4.40 | 4.72 | 4.79 | 1.96 | 3.69 | 4.22 |
| *Q2* | 1.07 | 4.39 | 4.85 | 4.89 | 1.82 | 3.69 | 4.35 |
| Mode | 1.10 | 5.98 | 6.27 | 6.27 | 1.96 | 5.41 | 5.98 |
| *s* | 0.46 | 1.59 | 1.39 | 1.36 | 0.16 | 1.30 | 1.50 |
| *Q1* | 0.77 | 2.96 | 3.57 | 3.77 | 1.72 | 2.40 | 2.82 |
| *Q3* | 1.41 | 5.70 | 5.76 | 5.83 | 1.91 | 4.68 | 5.43 |
| *P10* | 0.43 | 1.98 | 2.54 | 2.60 | 1.59 | 1.67 | 1.89 |
| *P90* | 1.66 | 6.14 | 5.23 | 6.16 | 2.04 | 5.18 | 5.85 |
| Skew[1] | 0.29 | -0.99 | -1.11 | -1.09 | 0.00 | -1.32 | -1.18 |
| Skew[2] | 1.05 | 0.02 | -0.28 | -0.22 | 2.66 | -0.00 | -0.25 |
| Skew[3] | 0.06 | -0.04 | -0.17 | -0.09 | 0.00 | -0.13 | -0.17 |
| Skew[4] | -0.04 | -0.16 | -0.25 | -0.28 | -0.01 | -0.15 | -0.24 |
| Skew (Moment) | 0.25 | -0.25 | -0.55 | -0.74 | 0.26 | -0.29 | -0.40 |
| Kurtosis[1] | 0.26 | 0.33 | 0.30 | 0.29 | 0.22 | 0.32 | 0.33 |
| Kurtosis (Moment) | 2.61 | 2.01 | 2.38 | 2.75 | 5.89 | 1.90 | 1.97 |
| Kurtosis (Mode) | 0.26 | 0.11 | 0.10 | 0.16 | 0.72 | 0.10 | 0.11 |
| | | | **f. Water** | | | | |
| $\overline{X}$ | 0.76 | 4.84 | 5.52 | 5.16 | 0.63 | 4.30 | 4.72 |
| *Q2* | 0.48 | 5.65 | 6.01 | 5.78 | 0.45 | 4.79 | 5.36 |
| Mode | 0.52 | 6.27 | 6.27 | 6.27 | 0.52 | 5.41 | 5.98 |
| *s* | 0.34 | 2.03 | 1.47 | 1.54 | 0.17 | 1.45 | 1.68 |
| *Q1* | 0.36 | 2.90 | 4.89 | 4.35 | 0.34 | 3.14 | 3.33 |
| *Q3* | 0.81 | 6.21 | 6.31 | 6.08 | 0.60 | 5.23 | 5.85 |
| *P10* | 0.29 | 1.47 | 2.80 | 2.32 | 0.28 | 1.79 | 1.74 |
| *P90* | 1.14 | 6.66 | 6.53 | 6.22 | 0.76 | 5.55 | 6.15 |
| Skew[1] | 0.69 | -0.71 | -0.51 | -0.72 | 0.64 | -0.76 | -0.75 |
| Skew[2] | 2.45 | -1.21 | -1.00 | -1.20 | 3.22 | -1.00 | -1.14 |
| Skew[3] | 0.46 | -0.67 | -0.58 | -0.65 | 0.18 | -0.58 | -0.62 |
| Skew[4] | 0.54 | -0.61 | -0.72 | -0.77 | 0.30 | -0.59 | -0.64 |
| Skew (Moment) | 1.43 | -0.54 | -1.42 | -1.33 | 1.39 | -0.82 | -0.80 |
| Kurtosis[1] | 0.27 | 0.32 | 0.19 | 0.22 | 0.27 | 0.28 | 0.29 |
| Kurtosis (Moment) | 4.47 | 2.08 | 4.13 | 3.56 | 4.30 | 2.59 | 2.40 |
| Kurtosis (Mode) | 0.59 | 0.16 | 0.25 | 0.31 | 0.68 | 0.18 | 0.20 |

**Table 8. Average snow depth (cm) for each land cover class and total area.**

| *Land cover class* | *6 Jan 78* | *11 Feb 78* | *1 Mar 78* | *24 Dec 78* | *11 Jan 79* |
|---|---|---|---|---|---|
| Softwoods | 38.1 | 66.0 | 63.5 | 45.7 | 50.8 |
| Hardwoods | 43.2 | 72.4 | 69.8 | 61.0 | 62.2 |
| Mixed forest | 44.4 | 77.5 | 76.2 | 54.6 | 63.5 |
| Open areas | 47.0 | 76.2 | 73.7 | 61.0 | 64.8 |
| Total area | 43.2 | 74.9 | 71.1 | 54.6 | 55.9 |

levels. For the total area histograms the means vary by less than 0.05 mW $cm^{-2}$ $sr^{-1}$ for the three Landsat-2 scenes and by 0.44 for all snow days (Fig. 24). Changes in skewness and kurtosis are irregular and do not relate well with increasing snow depth.

In MSS 5 the measures of central tendency and percentiles are often within 0.064 mW $cm^{-2}$/sr between days, particularly when those of one satellite's observations are considered. Where differences are greater than 0.064, most commonly they show decreases in magnitude for the days with greater snow depth. Th greater contribution of snow to the observed Landsat signal is not occurring with increasing snow depth because of the dominance of the forest canopy within the sensor's instantaneous field of view.

Within the nonforested cover classes, the corrected histograms show a relationship between increasing snow depth and the magnitude of reflected energy. As the snow accumulates throughout the snow season, the means and in particular the first quartile and 10th percentile increase in magnitude. The moment coefficients of skewness and kurtosis for the open areas and frozen water surfaces also show a consistent change in histogram shape as the snow depth increases. Snow depth measurements were not made over the water surfaces, but the lakes and rivers remained frozen throughout the winter season. Even with differences in accumulation caused by drifting, it may be assumed that as regional snow depth increased, the accumulation on the frozen water surfaces also increased.

In MSS 7, the water surfaces show consistent increases in magnitude (within each Landsat group) for the mean and particularly the first quartile and 10th percentile. These indicate a reduction in the low reflecting portions of the histogram. This is also shown in moment coefficients of skewness and kurtosis, both of which are dimensionless indices of data distribution. Thus, they allow for comparison between the two Landsat passes. The moment coefficient of skewness is negative because of the high mean values and the departure from symmetry to the left. It increases with snow depth largely because of the increasing value of the mean. The moment coefficient of kurtosis will increase as a distribution becomes more peaked. A normal distribution will have a kurtosis (moment) of 3. Thus, the water histograms show increasing kurtosis with snow depth.

For open areas, the histograms again show in both bands an increase in magnitude, skewness, and kurtosis. The trends in the skewness and kurtosis are less useful for open areas than for water areas because of the strong divergence from a Gaussian distribution for the open areas.

Although the differences between the snow scenes are variable in their suggestion of a snow depth/regional histogram relationship, this is not the case for comparing the snow scenes, considered as a group, with the non-snow scenes. The most striking differences occur for the water surfaces in MSS 5 and 7. Increases of greater than 500% are found for all measures of central tendency, quartiles, and percentiles. The water histograms under non-snow conditions display low radiance values with a tight cluster around the mean (Fig. 27). Subsequent freezing and covering by snow increases the histogram mode to higher energy values with a larger standard deviation. This is described by the change in magnitude of the mean, median, etc., the large increase in standard deviation, the reversal of skewness from positive to negative, and the decreased value of the moment coefficient of kurtosis.

Open areas are affected similarly to water by the addition of snow cover. The snow depths in all snow scenes are greater than 38 cm. Most low-lying vegetation is covered, providing a largely undisturbed, highly reflective snowpack. The percentage changes in MSS 7 are not as great as for water for two reasons: 1) irregularities in the vegetation canopy and possible anthropogenic structures in the agriculture areas contribute sections of lower reflectance, and 2) the non-snow reflectance of the open lands is higher than that of water. This is particularly true for the May scene when vegetation growth results in a higher near-infrared reflectance. Water absorbs radiation in the near-infrared wavelengths. Percentage changes for the measures in MSS 5 are similar to those for water. The absolute dimension of the snow values is not as high as for water in winter. Again, this is because of the presence of darker surfaces of dormant vegetation.

For forested sites, the contrast between snow and no-snow scenes will depend on species composition, season of the no-snow scene, and band wavelength. The softwood trees retain their leaves throughout the winter and display a high crown closure. In MSS 5, the histograms are almost identical for the October and May scenes. Increases of close to 100% are shown in these forests with the addition of snow. Radiance changes in MSS 7 are less pronounced, although they still occur. This is largely because of the infrared reflectance of the

conifer leaf structure, which remains the same throughout the autumn and winter.

The results of snow cover in the hardwoods and mixed forest are similar to the softwoods. In all seasons, the hardwoods display energy values several levels higher than do the evergreens in both MSS 5 and 7. Canopy structure and the loss of leaves in the winter are responsible for this increased reflectance. Percentage changes between no-snow and snow scenes are comparable for all forest types. The one exception occurs when the May scene and the winter scenes for MSS 7 are compared. In northern Maine, the hardwoods leaf out in late May. The leaf cellular structure and geometry result in high infrared reflectance. The magnitude of the energy in MSS 7 during May is equal to and often exceeds that for the snow-covered scene.

The forests display a smaller change between non-snow and snow conditions than either open areas or water. However, there is still a measureable, predictable displacement by several histogram levels for most statistical measures.

If Landsat bands 5 and 7 are considered together, the Landsat histograms—corrected to account for the solar angle and sensor calibration—could provide an automated evaluation of the presence and areal distribution of a snowpack, even in a heavily forested region such as northern New England. The MSS 7 statistics for the 27 Oct scene are significantly different from the other scenes (Table 7). Because of leaf emergence, the 31 May MSS 7 histogram statistics are similar to the snow scenes, although this similarity does not appear in MSS band 5.

### Landsat data as input to the SSARR model

The 31 May Landsat land cover classification provided a basis upon which the point measurements of water equivalent could be used in the SSARR model. The snow course measurements were selected to provide data for the various land cover classes present in the entire hydrologic basin. The ground measurements of water equivalent of snow were subsequently area-weighted to the May Landsat classification to derive mean regional water equivalent estimates for each of the five Landsat winter scenes (Table 9).

The 1 Mar 78 estimate of 19.46 cm of water equivalent was used as an input value to the SSARR model. This value was an estimate of snow water equivalent before the spring melt period had occurred. The time period of 1 March through 31 May 1978 was used for the simulation model run. Calibration of the Upper Saint John River Basin was accomplished by the New Brunswick Flood Forecast Centre. The parameters of soil moisture index and rain-freeze temperature were adjusted to optimize the prediction of runoff. The results of the SSARR run are shown in Figure 28.

**Table 9. Areal determination of snow depth and water equivalent for the basin.**

| *Landsat date* | *Snow depth (cm)* | *Water equivalent (cm)* |
|---|---|---|
| 6 Jan 78 | 42.27 | 7.42 |
| 11 Feb 78 | 73.58 | 20.24 |
| 1 Mar 78 | 70.94 | 19.46 |
| 24 Dec 78 | 51.92 | 6.10 |
| 11 Jan 79 | 58.95 | 14.30 |

The initial SSARR run showed that the magnitude of the first predicted runoff peak compared to the observed values for the Ninemile Bridge, Dickey, and Allagash subbasins was 58%, 70%, and 78%, respectively. The magnitude of the second predicted runoff peak for the Dickey and Allagash subbasins was 97% and 70%, respectively, of the recorded stream discharge values, whereas the second runoff peak for the Ninemile Bridge subbasin was overpredicted by 3%.

The time of the first predicted peak of runoff was earlier bb 8 days for the Ninemile Bridge and Allagash subbasins and by 9 days for the Dickey subbasin. The timing of the second predicted peak improved for Ninemile Bridge, Dickey, and Allagash, with a delay of 2, 3, and 5 days, respectively.

In summary, the initial baseflow period (1-27 March) predicted by the SSARR model was within 78% of the recorded stream discharge values. The spring melt recession (10–31 May 1978) predicted by the SSARR model was within 67% of the recorded stream discharge values. The timing of the six runoff peaks (Fig. 28) lagged by 2 to 9 days. The magnitude of the six predicted runoff peaks was within 75% of the recorded streamflow measurements. The error in the prediction of the initial storm peak for all three subbasins was attributed to the underprediction of snowmelt by the SSARR model caused by a rain-on-snow event that occurred on 28 March.

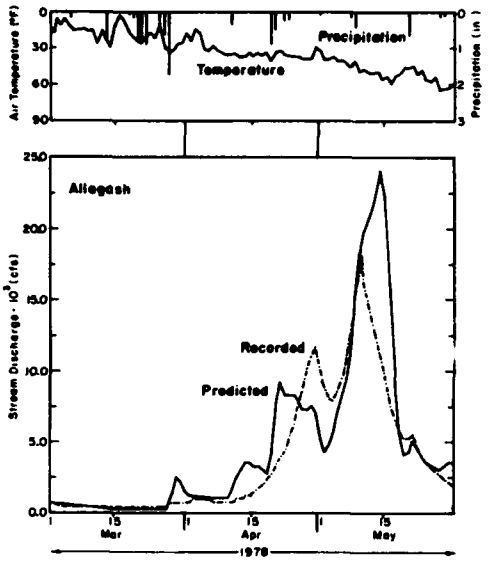


*a. Allagash subbasin.*

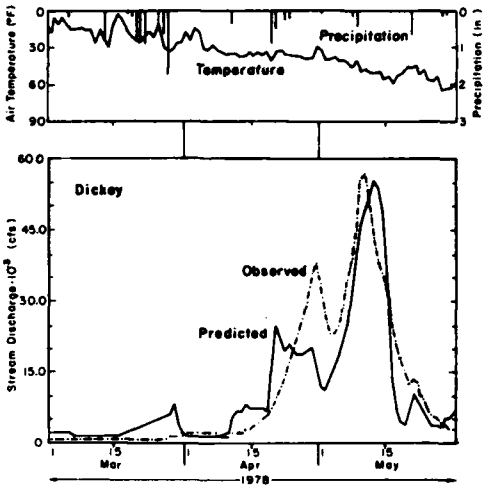


*b. Dickey subbasin.*

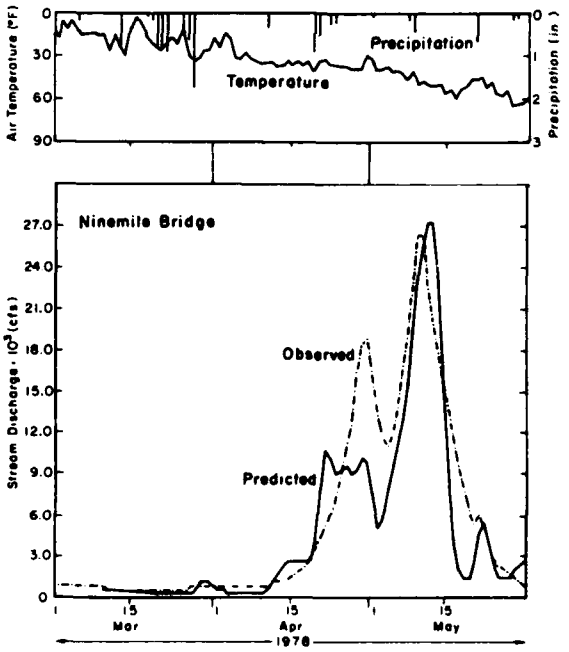


*c. Ninemile Bridge subbasin.*

*Figure 28. SSAR model run for the 1 March to 31 May 1978 time period.*

In temperate continental climatic zones, additional complications in spring melt arise when rain-on-snow events occur. The rainfall coupled with above-freezing temperatures can cause the snowpack to melt very rapidly. This type of occurrence may have to be modeled as a separate subroutine with SSARR. Additional work on recalibrating the basin peak timing and melt rate factors is also required.

## CONCLUSIONS

Initial histogram analysis presented in this study indicated that a good correlation existed between the satellite radiometric measurements and mean snow depth in the 420-km² area. Using Landsat uncorrected data an equation was developed to predict snow depth with a standard error of estimate of ±5 cm.

However, when subsequent corrections for sensor calibrations and solar elevation were taken into consideration, this correlation was eliminated for forested land cover. For open clearings and frozen water surfaces, definite increases in histogram means, quartiles, percentiles, kurtosis, and skewness were observed as regional snow depth increased. Some of our correlations would compare better with western snowpack satellite relationships if the models for western snowpacks had to contend with freeze–thaw cycles and rain-on-snow events. These two factors will definitely change the reflectance and brightness characteristics of the snowpack.

The ground measurements of water equivalent were area-weighted by the May land cover classification to derive a mean regional water equivalent estimate for input to the SSARR model. For the time period of 1 March through 31 May 1978, the SSARR model prediction was within 78% of the measured runoff for the initial baseflow period and within 67% for the spring melt recession period. The timing and magnitude of the runoff peaks requires additional work on recalibrating the basin peak timing factors and melt rate factors.

A technique was developed for using minimal ground truth snow course measurements coupled with a Landsat land cover classification to derive a mean areal average of water equivalent. This technique could be demonstrated for other watersheds by selecting an appropriate number of snow courses representative of land cover types. In forested basins where land cover can change within a few years' time, the Landsat data can be used periodically to develop a current land cover inventory of the basin.

## LITERATURE CITED


**Adams, W.P.** (1976) Areal differentiation of snow cover in east central Ontario. *Water Resources Research,* **12**(*6*): 1226–1234.

**Adams, W.P. and D.R. Barr** (1979) Vegetation-snow relationships in Labrador. In *Proceedings of the 36th Annual Meeting of the Eastern Snow Conference. Alexandria Bay, New York,* pp. 1–25.

**Adams, W.P. and N.T. Roulet** (1982) Areal differentiation of land and lake snowcover in a small subarctic drainage basin. *Nordic Hydrology,* **13**: 139–156.

**Alföldi, T.T.** (1976) Digital analysis of Landsat MSS imagery for snow mapping applications. Canada Centre for Remote Sensing, Energy, Mines and Resources, Technical Report, 21 pp.

**Anderson, D.M., H.L. McKim, L.W. Gatto, R.K. Haugen, W.K. Crowder, C.W. Slaughter and T.L. Marlar** (1974) Arctic and subarctic environmental analyses utilizing ERTS-1 imagery. Type III Final Report to NASA for the period June 1972–February 1974, Contract No. S-70253-AG, 112 pp.

**Anderson, H.W.** (1969) Storage and delivery of rainfall and snowmelt water as related to forest environments. In *Proceedings of the Third Forest Microclimate Symposium, Canadian Forestry Service* (J.M. Powell and C.F. Nolasco, Ed.), Calgary, Alberta, pp. 51–67.

**Anderson, H.W. and T.H. Pagenhart** (1957) Snow on forest slopes. In *Proceedings of the 25th Annual Meeting Western Snow Conference, Santa Barbara, California, 17–19 April,* pp. 19–23.

**Barnes, J.C. and C.J. Bowley** (1973) Use of ERTS data for mapping snow cover in the the western United States. *Symposium on Significant Results from ERTS-1, 5–9 March, New Carrollton, Maryland,* pp. 855–862.

**Barnes, J.C. and C.J. Bowley** (1974) Handbook of techniques for satellite snow mapping. Concord, Massachusetts: Environmental Research and Technology, Inc., Document No. 0407-F, 95 pp.

**Barnes, J.C. and M.D. Smallwood** (1975) Synopsis of current satellite snow mapping techniques, with emphasis on the application of near-infrared

data. *Operational Applications of Satellite Snowcover Observations, Workshop held at South Lake Tahoe, California, 18-20 August,* NASA SP-391, pp. 199-213.

**Barry, R.G.** (1983) Research on snow and ice. *Reviews of Geophysics and Space Physics,* **21**(*3*): 765-776.

**Bartolucci, L.A., R.M. Hoffer and S.G. Luther** (1975) Snowcover mapping by machine processing of Skylab and Landsat data. *Operational Applications of Satellite Snowcover Observations, Workshop held at South Lake Tahoe, California, 18-20 August,* NASA SP-391, pp. 295-311.

**Bates, R.** (1983) Snow cover and meteorology at Allagash, Maine, 1977-1980. USA Cold Regions Research and Engineering Laboratory, Special Report 83-20, 53 pp.

**Bauer, K.G. and J.A. Dutton** (1962) Albedo variations measured from an airplane over several types of surface. *Journal of Geophysical Research,* **67**(*6*): 2367-2376.

**Bergen, J.D.** (1975) A possible relation of albedo to the density and grainsize of natural snow cover. *Water Resources Research,* **11**(*5*): 745-746.

**Blyth, K., M.A.R. Cooper, N.E. Lindsey and R.B. Painter** (1974) Snow depth measurements with terrestrial photos. *Photogrammetric Engineering,* **40**(*8*): 937-942.

**Bohren, C.F. and R.L. Beschta** (1979) Snowpack albedo and snow density. *Cold Regions Science and Technology,* **1**(*1*): 47-50.

**Bowley, C.J., J.C. Barnes and A. Rango** (1981) Satellite snow mapping and runoff prediction handbook. *Applications Systems Verification and Transfer Project,* vol. III. NASA Technical Paper 1829, 87 pp.

**Budyko, M.I.** (1974) *Climate and Life* (Translated by D.H. Miller). New York: Academic Press, International Geophysical Series, vol. 18.

**Castruccio, P., H. Loats, D. Lloyd and P. Newman** (1981) Cost/benefit analysis for the ASVT on operational applications of satellite snow-cover observations. *Applications Systems Verification and Transfer Project,* vol. III. NASA Technical Paper 1828, 240 pp.

**Choudhury, B.** (1982) Spectral albedos of mid-latitude snowpacks. *Cold Regions Science and Technology,* **6**(*2*): 123-139.

**Cooper, S., P. Bock, J. Horowitz and D. Foran** (1975) The use of ERTS imagery in reservoir management and operation. Final Report for NASA, 105 pp.

**Dallam, W.C. and J. Foster** (1975) Digital snow mapping technique using Landsat data and General Electric IMAGE 100 system. *Operational Applications of Satellite Snowcover Observations, Workshop held at South Lake Tahoe, California, 18-20 August.* NASA SP-391, pp. 259-278.

**Dey, B., D.C. Goswami and A. Rango** (1983) Utilization of satellite snow-cover observations for seasonal streamflow estimates in the Western Himalayas. *Nordic Hydrology,* pp. 257-266.

**Dirmhirn, I. and F.D. Eaton** (1975) Some characteristics of the albedo of snow. *Journal of Applied Meteorology,* **14**(*3*): 375-379.

**Dozier, J., S.R. Schneider and D.F. McGinnis, Jr.** (1981) Effect of grain size and snowpack water equivalence on visible and near-infrared satellite observations of snow. *Water Resources Research,* **17**(*4*): 1213-1221.

**Draeger, W.C. and D.T. Lauer** (1974) Areal extent of snow in forested regions, a practical estimation technique using ERTS-1 data. In *Proceedings of the 9th Symposium on Remote Sensing of Environment, Ann Arbor, Michigan, 15-19 April,* vol. 1, pp. 333-339.

**Dunkle, R.V. and J.T. Bevans** (1956) An approximate analysis of the solar reflectance and transmittance of a snow cover. *Journal of Meteorology,* **13**: 212-216.

**Dutton, J.A.** (1962) An addition to the paper 'Albedo variations measured from an airplane over several types of surface.' *Journal of Geophysical Research,* **67**(*13*): 5365-5366.

**Environmental Research and Technology, Inc.** (1977) Terrestrial ecosystem analysis, Dickey-Lincoln School Lakes Project, Maine, Document P-2037 prepared for the U.S. Army Corps of Engineers, New England Division, 236 pp.

**Federer, C.A.** (1971) Radiation absorption by leafless hardwood forests. *Agricultural Meteorology,* **9**: 3-20.

**Ferguson, H.L. and S. Lapczak** (1977a) Analysis of snow cover over the Saint John and Souris River Basins. Progress Report for WMO Snow Studies by Satellite Project. Downsview, Ontario: Atmospheric Environment Service.

**Ferguson, H.L. and S. Lapczak** (1977b) Satellite imagery analysis of snow cover in the Saint John and Souris River basins. In *Proceedings of the 4th Canadian Symposium on Remote Sensing, Quebec, 16-18 May.* Ottawa, Ontario: Canadian Aeronautics and Space Institute, pp. 126-142.

**FitzGibbon, J.E. and T. Dunne** (1979) Characteristics of subarctic snowcover. *Hydrological Sciences Bulletin,* **24**(*4*): 465–476.

**Giddings, J.C. and E. La Chapelle** (1961) Diffusion theory applied to radiant energy distribution and albedo of snow. *Journal of Geophysical Research,* **66**(*1*): 181–189.

**Golding, D.L.** (1974) Snow cover and melting snow from ERTS imagery. *Canadian Surveyor,* **29(2):128-134.**

**Granberg, H.B.** (1972) Snow depth variations in a forest-tundra environment, Schefferville, P.Q. Winter 1968–1969. M.Sc. Thesis (unpub.), McGill University, 134 pp.

**Granberg, H.B.** (1975) Snow in different roughness zones at Schefferville: its character and hydrologic significance. In *Proceedings of the 32nd Eastern Snow Conference,* pp. 108–123.

**Hansen, P.L.** (1975) Experiences in snow cover mapping in the Saint John River Basin. In *Proceedings of the 3rd Canadian Symposium on Remote Sensing, Edmonton, Alberta, 22–24 September* (G.E. Thompson, Ed.). Ottawa, Ontario: Canadian Aeronautics and Space Institute, pp. 315–322.

**Itten, K.I.** (1975) Approaches to digital snow mapping with Landsat-1 data. *Operational Applications of Satellite Snowcover Observations, Workshop held at South Lake Tahoe, California, 18–20 August,* NASA SP-391, pp. 235–247.

**Katibah, E.F.** (1975a) Areal extent of snow estimation in the northern Sierra Nevada mountains using Landsat-1 imagery. In *Proceedings of the NASA Earth Resources Survey Symposium, Houston, Texas, June.* NASA TM X-58168, pp. 2621–2641.

**Katibah, E.F.** (1975b) Operational use of Landsat imagery for the estimation of snow areal extent. *Operational Applications of Satellite Snowcover Observations, Workshop held at South Lake Tahoe, California, 18–20 August,* NASA SP-391, pp. 129–142.

**Kondratyev, K.Ya.** (1969) *Radiation in the Atmosphere.* International Geophysical Series, vol. 12. New York: Academic Press.

**Kung, E.C., R.A. Bryson and D.H. Lenschow** (1964) Study of a continental surface albedo on the basis of flight measurements and structure of the Earth's surface cover over North America. *Monthly Weather Review,* **92**(*2*): 543–564.

**Kunzi, K.F., S. Patil and H. Rott** (1982) Snowcover parameters retrieved from Nimbus-7 Scanning Multichannel Microwave Radiometer (SMMR) data. *IEEE Transactions on Geoscience and Remote Sensing,* **GE-20**(*4*): 452–467.

**Kurilova, Yu.V.** (1975) Investigations of the snow cover from satellite data. Institute of Water Problems, Academy of Sciences of the USSR (translated from Vodnye Resursy), **2**: 50–60.

**Kurilova, Yu.V., P.A. Kolosov, L.K. Poplavskaya and Yu.S. Sokolov** (1976) Investigation of the dynamics of snow-cover melting from meteorological-satellite data. *Transactions of the State Hydrologic Institute (Trudy GGI),* **237**: 22–31. Also in *Soviet Hydrology: Selected papers,* **15**(21).

**Langham, E.J. and J.M. Power** (1977) Remote sensing of snow by satellite. In *Proceedings of the 2nd Conference on Hydrometeorology, Toronto, Ontario, Canada, 25–27 October.* Boston: American Meteorological Society, pp. 268–271.

**Leonard, R.E. and A.R. Eschner** (1968) Albedo of intercepted snow. *Water Resources Research,* **4**(25): 931–935.

**Lichtenegger, J., K. Seidel, M. Keller and H. Haefner** (1981) Snow surface measurements from digital Landsat MSS data. *Nordic Hydrology,* **12**: 275–288.

**Lillesand, T.M., D.E. Meisner, A.L. Downs and R.L. Deuell** (1982) Use of GOES and TIROS/NOAA satellite data for snow-cover mapping. *Photogrammetric Engineering and Remote Sensing,* **48**(*2*): 251–259.

**Luther, S.G., L.A. Bartolucci and R.M. Hoffer** (1975) Snow cover monitoring by machine processing of multitemporal Landsat MSS data. *Operational Applications of Satellite Snowcover Observations, Workshop held at South Lake Tahoe, California, 18–20 August.* NASA SP-391, pp. 279–311.

**Martinec, J.** (1975) Snowmelt-runoff model for stream flow forecasts. *Nordic Hydrology,* **6**: 145–154.

**Martinec, J.** (1982) Runoff modeling from snow-covered area. *IEEE Transactions on Geoscience and Remote Sensing,* **GE-20**(*3*): 259–262.

**Martinec, J. and A. Rango** (1981) Areal distribution of snow water equivalent evaluated by snow cover monitoring. *Water Resources Research,* **17**(*5*): 1480–1488.

**Martinec, J., A. Rango and E. Major** (1983) The snowmelt-runoff model (SRM) user's manual. NASA Ref. Pub. 1100. Greenbelt, Maryland: NASA Goddard Space Flight Center, 118 pp.

**Mathers, T.J.** (1980) The role of vegetation on the disposition of snowfall on a mixed forested watershed in the Kawatha Lakes region of east central Ontario. Studies in Snow and Ice (N.T. Roulet, Ed.). *Trent Student Geographer,* vol. 8. Peterborough, Ontario: Trent University, pp. 36–50.

**Matson, M. and D.R. Wiesnet** (1981) New data base for climate studies. *Nature,* **289**(*5797*): 451–456.

**McFadden, J.D. and R.A. Ragotzkie** (1967) Climatological significance of albedo in central Canada. *Journal of Geophysical Research,* **72**(*4*): 1135–1143.

**McGinnis, D.F., Jr.** (1975) A progress report on estimating snow depth using VHRR data from NOAA environmental satellites. *Operational Applications of Satellite Snowcover Observations, Workshop held at South Lake Tahoe, California, 18–20 August,* NASA SP-391, pp. 313–324.

**McGinnis, D.F., Jr., J.A. Pritchard and D. Wiesnet** (1975) Determination of snow depth and snow extent from NOAA-2 satellite Very High Resolution Radiometer data. *Water Resources Research,* **11**(*6*): 897–902.

**McGinnis, D.F., Jr., R.A. Scofield, S.R. Schneider and C.P. Berg** (1979) Satellites as an aid to water resource managers. *ASCE Convention, Boston, Massachusetts, 2–6 April.*

**McKim, H.L.** (1975) Vegetation analysis of the Dickey–Lincoln area, Maine. Map overlays provided to the New England Division, Corps of Engineers, showing vegetation types.

**McKim, H.L. and C.J. Merry** (1975) Use of remote sensing to quantify construction material and to define geologic lineations—Dickey–Lincoln School Lakes Project, Maine. USA Cold Regions Research and Engineering Laboratory, Special Report 242, parts 1 and 2, 26 pp.

**McMillan, M.C. and D.F. McGinnis** (1975) The possibility of determining snowpack surface conditions using remote multispectral techniques. In *Workshop for Environmental Applications of Multispectral Imagery, Ft. Belvoir, Virginia, 11–13 November.* U.S. Army Engineer Topographic Laboratories and American Society of Photogrammetry, pp. 304–313.

**McMillan, M.C. and J.L. Smith** (1975) Remote sensing of snowpack density using shortwave radiation. *Operational Applications of Satellite Snowcover Observations, Workshop held at South Lake Tahoe, California, 18–20 August,* NASA SP-391, pp. 361–373.

**Meier, M.F.** (1973) Evaluation of ERTS imagery for mapping and detection of changes of snowcover on land and on glaciers. *Symposium on Significant Results Obtained from ERTS-1, New Carrollton, Maryland, 5–9 March,* pp. 863–875.

**Meier, M.F.** (1974) New ways to monitor the mass and areal extent of snowcover. *COSPAR, Approaches to Earth Survey Problems through use of Space Techniques, F.R.G., 23–25 May 1973.* Berlin: Akademie-Verlag, pp. 241–250.

**Meier, M.F.** (1975a) Application of remote-sensing techniques to the study of seasonal snow cover. *Journal of Glaciology,* **15**(*73*): 251–265.

**Meier, M.F.** (1975b) Satellite measurement of snowcover for runoff prediction. Presented at 11th American Water Resources Conference, Baton Rouge, Louisiana, 24 pp.

**Meier, M.F. and W.E. Evans** (1975) Comparison of different methods for estimating snowcover in forested, mountainous basins using Landsat (ERTS) images. *Operational Applications of Satellite Snowcover Observations, Workshop held at South Lake Tahoe, California, 18–20 August,* NASA SP-391, pp. 215–234.

**Meiman, J.R.** (1970) Snow accumulation related to elevation, aspect and forest canopy. In *Proceedings of the Workshop Seminar on Snow Hydrology.* Queen's Printer, pp. 35–47.

**Mellor, M.** (1965) Optical measurements on snow. USA Cold Regions Research and Engineering Laboratory, Research Report 169, 19 pp.

**Mellor, M.** (1977) Engineering properties of snow. *Journal of Glaciology,* **19**(*81*): 15–66.

**Merry, C.J. and H.L. McKim** (1978) Computer processing of Landsat digital data and sensor interface development for use in New England reservoir management. USA Cold Regions Research and Engineering Laboratory, Special Report 78-6, 66 pp.

**Merry, C.J., H.L. McKim, S. Cooper and S.G. Ungar** (1977) Preliminary analysis of water equivalent/snow characteristics using Landsat digital processing techniques. In *Proceedings of the Eastern Snow Conference, Belleville, Ontario, 3–4 February,* pp. 39–54.

**NASA** (1982) Plan of research for snowpack properties remote sensing—$(PRS)^2$, Recommendations of the snowpack properties working group. Greenbelt, Maryland: NASA Goddard Space Flight Center, 38 pp.

**New England Division, Corps of Engineers** (1967) Saint John River Basin, Dickey–Lincoln School Project, Maine, U.S.A., and Quebec, Canada.

Department of the Army, New England Division, Corps of Engineers: Waltham, Massachusetts, Design Memorandum No. 4.

**Nicholson, F.H.** (1975) Snow depth mapping from aerial photographs for use in permafrost predictions. In *Proceedings of the 32nd Eastern Snow Conference*, pp. 124–136.

**O'Brien, H.W. and G. Koh** (1981) Near-infrared reflectance of snow-covered substrates. USA Cold Regions Research and Engineering Laboratory, CRREL Report 81-21.

**O'Brien, H.W. and R.H. Munis** (1975) Red and near-infrared spectral reflectance of snow. USA Cold Regions Research and Engineering Laboratory, Research Report 332.

**O'Neill, A.D.J. and D.M. Gray** (1973) Solar radiation penetration through snow. In *The Role of Snow and Ice in Hydrology, Proceedings of the Banff Symposia, September 1972.* Published jointly by WMO (Geneva), IAHS (Budapest), and UNESCO (Paris), pp. 227–241.

**Parry, J.T. and B.J. Grey** (1975) The mapping and interpretation of snow conditions in Quebec–Labrador using ESSA-9 composite minimum brightness (CMB) charts. *Photogrammetria*, **30**(*2*): 41–66.

**Patch, J.R.** (1981) Effects of forest cover on snow cover distribution in the Nashwaak Experimental Watershed Project. In *Proceedings of the 38th Annual Eastern Snow Conference, 4–5 June, Syracuse, New York*, pp. 76–87.

**Power, J.M., C.J. Merry, N.B.A. Trivett and S.E. Waterman** (1980) Snowpack estimation in the St. John River Basin. In *Proceedings of the 14th International Symposium on Remote Sensing of Environment, San Jose, Costa Rica, 23–30 April*, pp. 467–486.

**Rango, A.** (1975) Operational applications of satellite snowcover observations project. In *Proceedings of the 10th International Symposium on Remote Sensing of Environment, 6–10 October, Ann Arbor, Michigan.* Ann Arbor: Environmental Research Institute of Michigan, pp. 1367–1376.

**Rango, A.** (1978) Pilot tests of satellite snowcover/runoff forecasting systems. NASA Technical Memorandum 78109, 13 pp.

**Rango, A.** (1980a) Remote sensing of snow-covered area for runoff modelling. In *Hydrological Forecasting, Proceedings of the Oxford Symposium, April.* IAHS Publ. no. 129, pp. 291–297.

**Rango, A.** (1980b) Operational applications of satellite snow cover observations. *Water Resources Bulletin*, **16**(*6*): 1066–1073.

**Rango, A.** (1981) Application systems verification and transfer project. Vol. I. Operational applications of satellite snow cover observations—executive summary. NASA Technical Paper 1822, 81 pp.

**Rango, A.** (1983) Application of a simple snowmelt-runoff model to large river basins. In *Proceedings of the 1983 Western Snow Conference*, pp. 89-99.

**Rango, A. and K.I. Itten** (1976) Satellite potentials in snow cover monitoring and runoff prediction. *Nordic Hydrology*, **7**: 209–230.

**Rango, A. and J. Martinec** (1979) Application of a snowmelt-runoff model using Landsat data. *Nordic Hydrology*, **10**(*4*): 225–238.

**Rango, A. and J. Martinec** (1981) Accuracy of snowmelt runoff simulation. *Nordic Hydrology*, **12**: 265–274.

**Rango, A. and J. Martinec** (1982) Snow accumulation derived from modified depletion curves of snow coverage. In *Hydrological Aspects of Alpine and High-Mountain Areas, Proceedings of the Exeter Symposium* (J.W. Glen, Ed.). IAHS Publ. no. 138, pp. 83–90.

**Rango, A. and V.V. Salomonson** (1976) Satellite snow observations and seasonal streamflow forecasts. Final Report under NOAA Contract No. NA-776-74, 19 pp.

**Rango, A., J.F. Hannaford, R.L. Hall, M. Rosenzweig and A.J. Brown** (1979) Snow-covered area utilization in runoff forecasts. *Journal of the Hydraulics Division, Proceedings of the American Society of Civil Engineers.* Proc. Paper 14326, **105**(*HY1*): 53–66.

**Rango, A., V.V. Salomonson and J.L. Foster** (1975) Operational water management applications of snowcovered area observations. In *Proceedings of the NASA ERTS Symposium, Houston, Texas, June.* NASA TM X-58168, pp. 2669-2685.

**Rasmussen, W.O. and P.F. Ffolliott** (1979) Prediction of water yield using satellite imagery and a snowmelt simulation model. Unpublished report.

**Seidel, K., F. Ade and J. Lichtenegger** (1983) Augmenting Landsat MSS data with topographic information for enhanced registration and classification. *IEEE Transactions on Geoscience and Remote Sensing*, **GE-21**(*3*): 252–258.

**Shafer, B.A., C.F. Leaf, J.A. Danielson and G.F. Moravec** (1981) Operational applications of satellite snow-cover observations—Colorado Field Test Center. *Applications Systems Verification and Transfer Project*, vol. IV. NASA Technical Paper 1825, 101 pp.

**Sharp, J.M.** (1975) A comparison of operational and Landsat-aided snow water content estimation systems. *Operational Applications of Satellite Snowcover Observations, Workshop held at South Lake Tahoe, California, 18–20 August.* NASA SP-391, pp. 325–344.

**Sharp, J.M. and R.W. Thomas** (1975) A cost-effectiveness comparison of existing and Landsat-aided snow water content estimation systems. In *Proceedings of the 10th International Symposium on Remote Sensing of Environment, 6–10 October, Ann Arbor, Michigan.* Ann Arbor: Environmental Research Institute of Michigan, pp. 1255–1262.

**Shunying, Z., Z. Qunzhu, C. Xianzhang and J. Dehong** (1980) Studies on snow depth and snow runoff with images from NOAA-5 satellite. *Kexue Tongbao,* **25**(*11*): 942–946.

**Smith, D.A.** (1980) Flood forecasting in the Saint John River Basin, Mathematical Modeling Activities. In *Modeling Activities Related to Flood Damage Reduction, Proceedings of the Technology Transfer Workshop, Technical Workshop Series No. 2, Hull, Quebec, Canada, 25–29 May 1979.* Halifax, Nova Scotia: Inland Waters Directorate, Environment Canada, pp. 277–311.

**Steinhoff, H.W. and A.H. Barnes** (1976) Determination of snow depth and water equivalent by remote sensing. Completion Report Series No. 76, Environmental Resources Center, Colorado State University, Fort Collins, 13 pp.

**Steppuhn, H.** (1976) Areal water equivalents for prairie snowcovers by centralized sampling. In *Proceedings of the 44th Annual Western Snow Conference, Calgary, Alberta, 20–22 April,* pp. 63–68.

**Steppuhn, H. and G.E. Dyck** (1974) Estimating true basin snowcover. In *Advanced Concepts and Techniques in the Study of Snow and Ice Resources.* Washington, D.C.: National Academy of Sciences, U.S. International Hydrological Decade, pp. 314–328.

**Strong, A.E., E.P. McClain and D.F. McGinnis** (1971) Detection of thawing snow and ice packs through the combined use of visible and near-infrared measurements from Earth satellites. *Monthly Weather Review,* **99**(*11*): 828–830.

**Thomas, V.L.** (1975) Generation and physical characteristics of the Landsat-1 and -2 MSS computer compatible tapes. NASA document X563-75-223. Greenbelt, Maryland: NASA Goddard Space Flight Center, 73 pp.

**Thompson, A.G.** (1975) Utilization of Landsat monitoring capabilities for snowcover depletion analysis. *Operational Applications of Satellite Snowcover Observations, Workshop held at South Lake Tahoe, California, 18–21 August.* NASA SP-391, pp. 113–127.

**Thomsen, A.G. and W.D. Striffler** (1980) Spatial simulation of snow processes. *Symposium on Watershed Management, Boise, Idaho, 21–23 July.* New York: American Society of Civil Engineers, vol. 1, pp. 326–334.

**Ungar, S.G.** (1977) Multispectral Image Analysis Package (MAP1), Version 1.1, User's Manual. Unpublished draft report, 75 pp.

**U.S. Army Engineer Division, North Pacific** (1975) Program description and user manual for SSARR (Streamflow Synthesis and Reservoir Regulation) Model. Program 724-K5-G0010, U.S. Army Engineer Division, North Pacific, Portland, Oregon.

**U.S. Geological Survey and NASA** (1979) Landsat Data Users Handbook.

**Warren, S.G.** (1982) Optical properties of snow. *Reviews of Geophysics and Space Physics,* **20**(*1*): 67–89.

**Warskow, W.L., T.T. Wilson, Jr. and K. Kirdar** (1975) The application of hydrometeorological data obtained by remote sensing techniques for multipurpose reservoir operations. *Operational Applications of Satellite Snowcover Observations, Workshop held at South Lake Tahoe, California, 18–20 August.* NASA SP-391, pp. 29–37.

**Wiegman, E.J., W.E. Evans and R. Hadfield** (1975) Measuring snow cover using satellite imagery during 1973 and 1974 melt season: North Santiam, Boise, and Upper Snake Basins, Phase 1 Final Report. SRI Project 4122. Menlo Park, California: Stanford Research Institute, 79 pp.

**Wiscombe, W.J. and S.G. Warren** (1980) A model for the spectral albedo of snow. I: Pure snow. *Journal of Atmospheric Sciences,* **37**(*12*): 2712–2733.

## Table A1. Snow property data for Allagash, 1977–78.

| Date | Site 1 | | | Site 3 | | | Site 4 | | | Site 5 | | | Site 7 | | | Site 9 | | | Site 10 | | | Site 11 | | | Site 12 | | | Site 13 | | | Site 15 | | |
|---|---|---|---|---|---|---|---|---|---|---|---|---|---|---|---|---|---|---|---|---|---|---|---|---|---|---|---|---|---|---|---|---|
| | Depth (cm) | WE (cm) | Den ($g/cm^3$) | Depth (cm) | WE (cm) | Den ($g/cm^3$) | Depth (cm) | WE (cm) | Den ($g/cm^3$) | Depth (cm) | WE (cm) | Den ($g/cm^3$) | Depth (cm) | WE (cm) | Den ($g/cm^3$) | Depth (cm) | WE (cm) | Den ($g/cm^3$) | Depth (cm) | WE (cm) | Den ($g/cm^3$) | Depth (cm) | WE (cm) | Den ($g/cm^3$) | Depth (cm) | WE (cm) | Den ($g/cm^3$) | Depth (cm) | WE (cm) | Den ($g/cm^3$) | Depth (cm) | WE (cm) | Den ($g/cm^3$) |
| 12/20/77–12/21/77 | 40.1 | 6.1 | 0.152 | 40.4 | 6.1 | 0.151 | 29.7 | 2.8 | 0.094 | 45.7 | 7.9 | 0.181 | 41.6 | 7.1 | 0.171 | 46.2 | 8.4 | 0.181 | | | | | | | | | | | | | 39.6 | 5.6 | 0.141 |
| Snow pit | | | 0.194 | | | | | | | | | | | | | | | 0.181 | | | | | | | | | | | | | | |
| 1/7/78–1/8/78 | 45.7 | 7.4 | 0.162 | 39.9 | 7.1 | 0.178 | 29.2 | 3.8 | 0.130 | 45.0 | 9.1 | 0.203 | 39.9 | 6.1 | 0.153 | 50.8 | 8.1 | 0.159 | 46.5 | 9.6 | 0.206 | 46.5 | 8.9 | 0.191 | 45.7 | 7.4 | 0.161 | 46.0 | 7.6 | 0.166 | 42.7 | 6.4 | 0.149 |
| Snow pit | | | 0.178 | | | | | | | | | | | | | | | 0.198 | | | | | | | | | | | | | | 0.202 |
| 1/25/78–1/26/78 | 76.2 | 15.7 | 0.206 | 65.5 | 14.0 | 0.220 | 50.8 | 6.4 | 0.125 | 66.0 | 15.7 | 0.238 | 75.7 | 16.5 | 0.224 | 75.7 | 14.7 | 0.195 | 69.1 | 17.3 | 0.250 | 65.5 | 18.0 | 0.275 | 67.8 | 18.3 | 0.270 | 68.1 | 18.5 | 0.268 | 68.1 | 12.9 | 0.190 |
| Snow pit | | | 0.185 | | | | | | | | | | | | | | | 0.233 | | | | | | | | | | | | | | 0.224 |
| 2/12/78–2/13/78 | 77.5 | 21.8 | 0.281 | 69.8 | 17.3 | 0.248 | 55.4 | 10.7 | 0.193 | 83.0 | 25.9 | 0.312 | 74.2 | 21.3 | 0.287 | 72.4 | 20.8 | 0.288 | 75.7 | 22.3 | 0.295 | 70.4 | 22.1 | 0.314 | 74.2 | 22.9 | 0.308 | 77.0 | 24.4 | 0.317 | 75.4 | 18.8 | 0.249 |
| Snow pit | | | 0.226 | | | | | | | | | | | | | | | 0.239 | | | | | | | | | | | | | | 0.232 |
| 3/2/78–3/3/78 | 74.4 | 21.8 | 0.293 | 67.8 | 17.5 | 0.258 | 51.6 | 11.4 | 0.221 | 80.8 | 25.6 | 0.318 | 72.9 | 21.8 | 0.300 | 69.8 | 19.3 | 0.277 | 74.2 | 20.5 | 0.274 | 66.5 | 18.0 | 0.271 | 71.6 | 20.3 | 0.284 | 75.4 | 23.6 | 0.313 | 74.2 | 18.5 | 0.250 |
| Snow pit | | | 0.306 | | | | | | | | | | | | | | | 0.320 | | | | | | | | | | | | | | 0.257 |
| 3/20/78–3/21/78 | 88.4 | 30.0 | 0.339 | 82.0 | 24.9 | 0.304 | 67.3 | 17.0 | 0.253 | 91.4 | 30.5 | 0.333 | 90.2 | 27.9 | 0.310 | 79.5 | 26.4 | 0.332 | 90.2 | 27.7 | 0.307 | 83.8 | 28.2 | 0.336 | 90.2 | 29.7 | 0.329 | 86.4 | 28.7 | 0.332 | 85.8 | 24.6 | 0.287 |
| Snow pit | | | 0.279 | | | | | | | | | | | | | | | 0.303 | | | | | | | | | | | | | | 0.328 |
| 4/7/78–4/8/78 | 111.8 | 34.5 | 0.309 | 94.5 | 29.2 | 0.309 | 78.0 | 18.5 | 0.234 | 106.7 | 36.1 | 0.338 | 100.3 | 34.0 | 0.339 | 99.6 | 35.0 | 0.351 | 102.4 | 32.2 | 0.315 | 95.2 | 34.5 | 0.360 | 102.1 | 33.5 | 0.328 | 100.8 | 32.5 | 0.322 | 98.3 | 30.0 | 0.305 |
| Snow pit | | | 0.326 | | | | | | | | | | | | | | | 0.366 | | | | | | | | | | | | | | 0.353 |
| 4/12/78–4/13/78 | 97.0 | 31.0 | 0.319 | 84.6 | 25.4 | 0.300 | 71.9 | 16.8 | 0.233 | 92.2 | 30.0 | 0.325 | 101.1 | 31.0 | 0.306 | 90.9 | 34.8 | 0.383 | 91.9 | 26.9 | 0.293 | 86.4 | 29.7 | 0.344 | 95.5 | 36.0 | 0.321 | 87.6 | 25.4 | 0.290 | 85.6 | 27.2 | 0.318 |
| Snow pit | | | 0.386 | | | | | | | | | | | | | | | 0.426 | | | | | | | | | | | | | | 0.392 |
| 4/19/78–4/20/78 | 74.9 | 24.6 | 0.329 | 72.9 | 21.6 | 0.296 | 65.5 | 14.5 | 0.221 | 88.4 | 27.2 | 0.307 | 85.1 | 27.2 | 0.319 | 78.0 | 27.4 | 0.352 | 80.5 | 25.9 | 0.322 | 82.0 | 25.9 | 0.316 | 80.8 | 24.9 | 0.308 | 79.2 | 21.6 | 0.273 | 75.1 | 22.4 | 0.306 |
| Snow pit | | | 0.480 | | | | | | | | | | | | | | | 0.444 | | | | | | | | | | | | | | 0.408 |
| 4/26/78–4/27/78 | 57.5 | 9.6 | 0.259 | 48.5 | 12.2 | 0.252 | 41.9 | 8.4 | 0.200 | 64.0 | 19.0 | 0.298 | 69.3 | 18.5 | 0.285 | 60.1 | 10.7 | 0.266 | 60.2 | 15.2 | 0.255 | 49.5 | 14.7 | 0.298 | 56.6 | 15.2 | 0.269 | 52.8 | 10.9 | 0.207 | 44.4 | 13.2 | 0.297 |
| Snow pit | | | 0.490 | | | | | | | | | | | | | | | 0.471 | | | | | | | | | | | | | | 0.480 |
| 5/3/78 | No snow | | | 55.0 | 10.7 | 0.304 | 31.3 | 5.6 | 0.180 | ----------Sites inaccessible due to muddy roads---------- | | | | | | | | | | | | | | | | | | | | 27.4 | 8.1 | 0.296 |
| Snow pit | | | | | | | | | | | | | | | | | | | | | | | | | | | | | | | | | 0.540 |

## Table A2. Snow property data for Allagash, 1978–79 data.

| Date | Site 1 | | | Site 3 | | | Site 4 | | | Site 5 | | | Site 7 | | | Site 9 | | | Site 10 | | | Site 11 | | | Site 12 | | | Site 13 | | | Site 15 | | |
|---|---|---|---|---|---|---|---|---|---|---|---|---|---|---|---|---|---|---|---|---|---|---|---|---|---|---|---|---|---|---|---|---|
| | Depth (cm) | WE (cm) | Den ($g/cm^3$) | Depth (cm) | WE (cm) | Den ($g/cm^3$) | Depth (cm) | WE (cm) | Den ($g/cm^3$) | Depth (cm) | WE (cm) | Den ($g/cm^3$) | Depth (cm) | WE (cm) | Den ($g/cm^3$) | Depth (cm) | WE (cm) | Den ($g/cm^3$) | Depth (cm) | WE (cm) | Den ($g/cm^3$) | Depth (cm) | WE (cm) | Den ($g/cm^3$) | Depth (cm) | WE (cm) | Den ($g/cm^3$) | Depth (cm) | WE (cm) | Den ($g/cm^3$) | Depth (cm) | WE (cm) | Den ($g/cm^3$) |
| 12/6/78 Snow Pit | | | | | | | | | | | | | | | | | | | 19.6 | 3.6 | 0.181 | 19.3 | 2.8 | 0.145 | 11.2 | 1.8 | 0.159 | 19.0 | 02.8 | 0.147 0.164 | | | |
| 12/15/78 Snow pit | 28.9 | 4.6 | 0.158 0.152 | 24.1 | 4.3 | 0.179 | 18.5 | 2.5 | 0.137 | 35.0 | 4.6 | 0.131 | 35.0 | 4.8 | 0.138 0.156 | 33.0 | 3.0 | 0.092 0.150 | | | | | | | | | | | | 33.5 | 3.8 | 0.114 |
| 12/24/78 Snow pit | 61.5 | 8.1 | 0.132 0.155 | | | | | | | | | | | | | | | | 55.1 | 7.4 | 0.134 | 59.7 | 8.1 | 0.136 | 45.2 | 5.8 | 0.084 | 60.4 | 7.6 | 0.125 0.192 | | | |
| 1/11/79 Snow pit | 64.3 | 15.7 | 0.245 0.218 | 57.9 | 14.7 | 0.254 | 43.7 | 12.7 | 0.291 | 67.8 | 16.0 | 0.236 | 62.2 | 13.5 | 0.216 | 69.3 | 16.0 | 0.245 0.202 | | | | | | | | | | | | 60.4 | 13.5 | 0.223 |
| 1/20/79 Snow pit | 71.1 | -- | -- 0.247 | | | | | | | | | | | | | | | | 70.4 | 17.3 | 0.245 | 72.4 | 19.6 | 0.270 | 55.1 | 10.2 | 0.184 | 69.1 | 16.5 | 0.239 0.231 | | | |
| 1/29/79 Snow pit | 72.4 | 20.1 | 0.277 0.246 | 59.2 | 15.2 | 0.225 | 58.4 | 17.3 | 0.296 | 66.8 | 17.8 | 0.266 | 65.5 | 17.8 | 0.271 | 72.9 | 21.6 | 0.296 0.381 | | | | | | | | | | | | | | |
| 2/7/79 Snow pit | 81.8 | 22.9 | 0.279 0.232 | | | | | | | | | | | | | | | | 93.2 | 25.6 | 0.253 | 85.1 | 23.6 | 0.277 | 58.9 | 13.7 | 0.232 | 90.2 | 22.3 | 0.248 0.230 | | | |
| 2/16/79 Snow pit | 74.9 | 25.6 | 0.315 0.246 | 69.3 | 21.1 | 0.304 | 56.4 | 19.1 | 0.338 | 76.7 | 25.9 | 0.338 | 69.3 | 22.1 | 0.319 | 74.2 | 23.4 | 0.315 0.253 | | | | | | | | | | | | 72.9 | 21.6 | 0.296 |
| 2/25/79 Snow pit | 77.0 | 20.5 | 0.264 0.263 | | | | | | | | | | | | | | | | 81.3 | 25.9 | 0.319 | 83.3 | 24.9 | 0.299 | 61.5 | 14.7 | 0.239 | 85.1 | 25.4 | 0.298 0.250 | | | |
| 3/6/79 Snow pit | | | | 62.2 | 17.8 | 0.286 | 50.3 | 19.6 | 0.389 | 72.4 | 21.6 | 0.298 | 66.8 | 18.3 | 0.274 | 69.3 | 19.6 | 0.282 0.294 | | | | | | | | | | | | 70.6 | 21.6 | 0.306 |
| 3/15/79 Snow pit | 87.8 | 17.0 | 0.251 0.296 | | | | | | | | | | | | | | | | 68.1 | 22.9 | 0.336 | 64.3 | 24.6 | 0.383 | 46.2 | 14.0 | 0.302 | 70.6 | 22.9 | 0.324 0.319 | | | |
| 3/28/79 Snow pit | 53.3 | 21.1 | 0.395 0.397 | 41.9 | 16.0 | 0.382 | 41.1 | 14.7 | 0.358 | 53.3 | 21.1 | 0.395 | 51.6 | 16.5 | 0.320 | 42.4 | 18.5 | 0.437 0.336 | | | | | | | | | | | | 57.9 | 19.0 | 0.329 |
| 4/2/79 Snow pit | 24.1 | 7.6 | 5.16 0.420 | | | | | | | | | | | | | | | | 27.9 | 11.9 | 0.428 | 27.2 | 10.7 | 0.392 | 14.7 | 5.6 | 0.380 | 33.5 | 12.2 | 0.364 0.380 | | | |
| 4/11/79 Snow pit | 67.3 | 17.0 | 0.253 0.350 | 71.1 | 21.6 | 0.304 | 46.2 | 9.4 | 0.203 | 71.6 | 20.8 | 0.290 | 71.6 | 18.5 | 0.259 | | | | | | | | | | | | | | | 73.1 | 22.1 | 0.302 |
| 4/20/79 Snow pit | 30.5 | 13.2 | 0.433 0.436 | | | | | | | | | | | | | | | | 17.3 | 8.9 | 0.514 | 26.7 | 12.2 | 0.457 | 13.5 | 6.9 | 0.511 | 22.3 | 10.7 | 0.478 0.496 | | | |

## Table A3. Snow property data for Allagash, 1979–80 data.

| Date | Site 1 | | | Site 3 | | | Site 4 | | | Site 5 | | | Site 7 | | | Site 9 | | | Site 10 | | | Site 11 | | | Site 12 | | | Site 13 | | | Site 15 | | |
|---|---|---|---|---|---|---|---|---|---|---|---|---|---|---|---|---|---|---|---|---|---|---|---|---|---|---|---|---|---|---|---|---|---|
| | Depth (cm) | WE (cm) | Den ($g/cm^3$) | Depth (cm) | WE (cm) | Den ($g/cm^3$) | Depth (cm) | WE (cm) | Den ($g/cm^3$) | Depth (cm) | WE (cm) | Den ($g/cm^3$) | Depth (cm) | WE (cm) | Den ($g/cm^3$) | Depth (cm) | WE (cm) | Den ($g/cm^3$) | Depth (cm) | WE (cm) | Den ($g/cm^3$) | Depth (cm) | WE (cm) | Den ($g/cm^3$) | Depth (cm) | WE (cm) | Den ($g/cm^3$) | Depth (cm) | WE (cm) | Den ($g/cm^3$) | Depth (cm) | WE (cm) | Den ($g/cm^3$) |
| 12/19/79–12/21/79 | 14.0 | 2.5 | 0.164 | 12.7 | 1.0 | 0.080 | 9.6 | 0.2 | 0.021 | 18.5 | 2.5 | 0.137 | 18.1 | 2.5 | 0.138 | 21.0 | 2.5 | 0.120 | 19.0 | 2.5 | 0.133 | 18.5 | 2.3 | 0.123 | 9.4 | 0.0 | — | 19.8 | 2.3 | 0.115 | 17.0 | 2.5 | 0.149 |
| | | | | | | | | | | | | | | | | | | | | | | | | | | | | | | 0.144 | | | |
| Snow pit | | | 0.140 | | | | | | | | | | | | | | | 0.128 | | | | | | | | | | | | | | | |
| 1/6/80–1/7/80 | 26.2 | 5.8 | 0.146 | 26.2 | 4.6 | 0.175 | 20.8 | 4.8 | 0.231 | 37.3 | 7.1 | 0.190 | 40.6 | 6.4 | 0.156 | 30.0 | 4.8 | 0.161 | 36.3 | 7.1 | 0.196 | 34.3 | 5.8 | 0.170 | 18.3 | 3.3 | 0.181 | 41.9 | 8.6 | 0.206 | 42.7 | 8.1 | 0.190 |
| | | | | | | | | | | | | | | | | | | | | | | | | | | | | | | 0.127 | | | |
| Snow pit | | | 0.179 | | | | | | | | | | | | | | | 0.152 | | | | | | | | | | | | | | | |
| 1/24/80–1/25/80 | 38.9 | 6.6 | 0.170 | 41.4 | 6.4 | 0.155 | 31.0 | 5.6 | 0.180 | 51.3 | 9.6 | 0.188 | 50.3 | 9.6 | 0.192 | 48.3 | 9.4 | 0.195 | 50.0 | 9.9 | 0.198 | 46.5 | 8.9 | 0.191 | 30.0 | 4.6 | 0.152 | 56.6 | 12.9 | 0.229 | 46.2 | 9.6 | 0.209 |
| | | | | | | | | | | | | | | | | | | | | | | | | | | | | | | 0.234 | | | |
| Snow pit | | | 0.162 | | | | | | | | | | | | | | | 0.181 | | | | | | | | | | | | | | | |
| 2/11/80–2/12/80 | 52.5 | 5.6 | 0.172 | 58.6 | 7.4 | 0.191 | 27.4 | 5.8 | 0.139 | 52.6 | 11.4 | 0.217 | 46.5 | 10.7 | 0.229 | 38.6 | 8.1 | 0.210 | 47.5 | 11.9 | 0.251 | 45.0 | 9.6 | 0.215 | 29.2 | 7.6 | 0.261 | 44.4 | 10.2 | 0.228 | 42.7 | 8.9 | 0.208 |
| | | | | | | | | | | | | | | | | | | | | | | | | | | | | | | 0.269 | | | |
| Snow pit | | | 0.257 | | | | | | | | | | | | | | | 0.207 | | | | | | | | | | | | | | | |
| 2/28/80–2/29/80 | 49.5 | 10.2 | 0.205 | 45.9 | 10.2 | 0.231 | 37.6 | 5.8 | 0.155 | 62.2 | 11.4 | 0.184 | 57.9 | 10.9 | 0.189 | 47.5 | 11.9 | 0.251 | 59.2 | 11.9 | 0.202 | 66.5 | 13.2 | 0.198 | 37.3 | 10.2 | 0.272 | 75.7 | 18.3 | 0.242 | 67.8 | 14.7 | 0.217 |
| | | | | | | | | | | | | | | | | | | | | | | | | | | | | | | 0.245 | | | |
| Snow pit | | | 0.248 | | | | | | | | | | | | | | | 0.209 | | | | | | | | | | | | | | | |
| 3/18/80–3/19/80 | 77.0 | 19.0 | 0.247 | 52.6 | 12.7 | 0.241 | 49.5 | 10.9 | 0.220 | 77.5 | 19.0 | 0.246 | 71.1 | 16.8 | 0.236 | 66.5 | 13.5 | 0.202 | 71.9 | 18.3 | 0.254 | 56.6 | 17.0 | 0.300 | 37.6 | 10.2 | 0.270 | 90.0 | 12.2 | 0.244 | 60.4 | 12.7 | 0.210 |
| | | | | | | | | | | | | | | | | | | | | | | | | | | | | | | 0.326 | | | |
| Snow pit | | | 0.248 | | | | | | | | | | | | | | | 0.225 | | | | | | | | | | | | | | | |
| 3/28/80–3/29/80 | 44.4 | 12.7 | 0.286 | 43.7 | 10.7 | 0.244 | 31.8 | 6.8 | 0.216 | 55.4 | 16.0 | 0.289 | 52.1 | 12.7 | 0.244 | 42.4 | 14.0 | 0.329 | 61.7 | 16.8 | 0.272 | | | | | | | | | | | | |
| Snow pit | | | 0.366 | | | | | | | | | | | | | | | 0.321 | | | | | | | | | | | | | | | |
| 4/5/80–4/6/80 | 23.4 | 8.9 | 0.380 | 39.9 | 11.9 | 0.299 | 24.6 | 5.1 | 0.206 | 46.2 | 14.5 | 0.313 | 34.8 | 9.6 | 0.277 | 19.6 | 5.1 | 0.260 | 29.2 | 11.4 | 0.390 | 40.1 | 15.2 | 0.380 | 19.8 | 6.9 | 0.346 | 32.2 | 13.2 | 0.409 | 46.5 | 11.4 | 0.246 |
| | | | | | | | | | | | | | | | | | | | | | | | | | | | | | | 0.420 | | | |
| Snow pit | | | 0.410 | | | | | | | | | | | | | | | 0.420 | | | | | | | | | | | | | | | |
| 4/14/80–4/15/80 | 13.2 | 5.3 | 0.250 | 27.2 | 9.6 | 0.355 | 17.5 | 5.8 | 0.221 | 36.8 | 12.7 | 0.345 | 17.8 | 4.3 | 0.243 | | | | 24.9 | 9.1 | 0.367 | 31.2 | 10.2 | 0.325 | 10.9 | 3.0 | 0.275 | 22.3 | 8.9 | 0.398 | 27.9 | 7.1 | 0.255 |
| | | | | | | | | | | | | | | | | | | | | | | | | | | | | | | 0.420 | | | |
| Snow pit | | | | | | | | | | | | | | | | | | | | | | | | | | | | | | | | | |

## Table A4. Snow property data for Allagash. Additional data from site 1.

| 1977-1978 | | | | | 1978-1979 | | | | | 1979-1980 | | | | |
|---|---|---|---|---|---|---|---|---|---|---|---|---|---|---|
| Date | Depth (cm) | WE (cm) | Density ($g/cm^3$) | Snow pit Density ($g/cm^3$) | Date | Depth (cm) | WE (cm) | Density ($g/cm^3$) | Snow pit density ($g/cm^3$) | Date | Depth (cm) | WE (cm) | Density ($g/cm^3$) | Snow pit density ($g/cm^3$) |
| 12-27 | 40.6 | 5.3 | 0.131 | -- | 12-04 | 19.6 | 3.6 | 0.184 | 0.180 | 12-24 | 12.7 | 2.5 | 0.197 | 0.144 |
| 01-12 | 38.1 | 7.9 | 0.207 | 0.220 | 12-11 | 18.0 | 2.5 | 0.141 | 0.180 | 12-31 | 28.4 | 4.6 | 0.161 | 0.140 |
| 01-17 | 54.1 | 9.9 | 0.183 | 0.197 | 12-18 | 55.1 | 7.1 | 0.129 | 0.138 | 01-14 | 20.3 | 9.6 | 0.473 | 0.240 |
| 01-23 | 78.2 | 19.0 | 0.244 | — | 01-01 | 64.0 | 13.2 | 0.206 | 0.244 | 01-21 | 22.1 | 5.3 | 0.241 | 0.180 |
| 01-31 | 74.4 | 14.5 | 0.195 | 0.208 | 01-08 | 61.5 | 18.3 | 0.297 | 0.251 | 01-28 | 34.8 | 6.6 | 0.190 | 0.186 |
| 02-06 | 66.5 | 14.5 | 0.218 | 0.214 | 01-15 | 71.1 | 19.8 | 0.279 | 0.231 | 02-04 | 34.8 | 6.9 | 0.197 | 0.242 |
| 02-20 | 75.7 | 21.1 | 0.278 | 0.235 | 01-22 | 90.9 | 22.4 | 0.246 | 0.232 | 02-18 | 36.3 | 6.4 | 0.175 | 0.235 |
| 02-27 | 73.7 | 21.6 | 0.293 | 0.264 | 02-05 | 86.4 | 22.1 | 0.256 | 0.291 | 02-25 | 52.1 | 11.4 | 0.219 | 0.246 |
| 03-06 | 78.2 | 23.6 | 0.302 | 0.296 | 02-12 | 77.5 | 20.8 | 0.269 | 0.245 | 03-03 | 48.8 | 9.6 | 0.198 | 0.246 |
| 03-13 | 78.0 | 23.9 | 0.306 | 0.269 | 02-19 | 74.4 | 21.1 | 0.283 | 0.238 | 03-10 | 63.0 | 12.4 | 0.198 | 0.228 |
| 03-27 | 115.6 | 36.3 | 0.314 | 0.257 | 03-05 | 78.2 | 24.6 | 0.315 | 0.331 | 03-17 | 71.1 | 17.3 | 0.243 | 0.261 |
| 04-03 | 111.0 | 36.1 | 0.325 | 0.312 | 03-12 | 67.8 | 17.8 | 0.262 | 0.274 | 03-24 | 69.1 | 14.7 | 0.213 | 0.264 |
| | | | | | 03-19 | 66.0 | 14.0 | 0.212 | 0.316 | 03-31 | 27.9 | 6.9 | 0.245 | 0.408 |
| | | | | | 03-26 | 51.8 | 14.7 | 0.464 | 0.460 | | | | | |
| | | | | | 04-01 | 53.3 | 14.0 | 0.262 | 0.256 | | | | | |
| | | | | | 04-16 | 53.8 | 19.8 | 0.368 | 0.400 | | | | | |
| | | | | | 04-25 | 16.5 | 8.1 | 0.493 | 0.460 | | | | | |

# APPENDIX B: METEOROLOGICAL AND HYDROLOGICAL DATA FOR THE UPPER SAINT JOHN RIVER BASIN, OCTOBER 1977 THROUGH MAY 1980

## Stream Flow

```
6D  01010000812017 2781  2800  2650  2500  2400  2250  2100  2000  1950
6D  01010000812017 2781  1850  1750  1680  1600  1550  1500  1450  1400
6D  01010000812017 2781  1350  1300  1250  1200  1150  1100  1070  1030
6D  01010000412025 2781  1000   990   970   940     0     0     0     0
6D  01010000812017 3781   920   890   870   860   825   820   800   780
6D  01010000812017 3781   765   750   735   725   710   690   680   675
6D  01010000812017 3781   670   660   650   640   630   630   640   665
6D  01010000712025 3781   700   740   790   830   880   925   970     0
6D  01010000812017 4781  1000   990   970   940   920   890   870   850
6D  01010000812017 4781   830   840   880   960  1100  1300  1500  1750
6D  01010000812017 4781  2100  2450  2900  3500  4250  5300  6600  7800
6D  01010000612025 4781  9400 11500 12700 16400 18400 18900     0     0
6D  01010000812017 5781 16500 13300 11700 11200 11900 13900 16700 19000
6D  01010000812017 5781 22100 26500 26400 23400 20200 18000 16100 14000
6D  01010000812017 5781 11800  9700  7740  6250  5410  6080  5110  3940
6D  01010000712025 5781  3100  2530  2130  1800  1500  1230  1030     0
6D  01010500812017 2781  4400  3900  3500  3050  2800  2600  2350  2200
6D  01010500812017 2781  2050  1950  1850  1760  1700  1650  1580  1520
6D  01010500812017 2781  1480  1420  1370  1310  1290  1260  1220  1190
6D  01010500412025 2781  1160  1130  1110  1100     0     0     0     0
6D  01010500812017 3781  1070  1040  1030  1010   990   980   970   965
6D  01010500812017 3781   945   935   920   910   900   895   885   880
6D  01010500812017 3781   875   870   865   860   855   850   860   880
6D  01010500712025 3781   940  1000  1100  1220  1480  1540  1700     0
6D  01010500812017 4781  1950  2050  2020  2000  1980  1920  1880  1830
6D  01010500812017 4781  1800  1800  1880  2050  2300  2750  3200  3850
6D  01010500812017 4781  4500  5200  6300  7500  9500 12000 14000 17000
6D  01010500612025 4781 20000 23100 26300 30000 36000 38200     0     0
6D  01010500812017 5781 33900 27500 23300 22900 24700 28900 34700 39300
6D  01010500812017 5781 44800 55700 57000 51000 43800 39300 35800 31500
6D  01010500812017 5781 26100 22000 18100 14900 12900 13500 12400  9820
6D  01010500712025 5781  7710  6200  5150  4340  3800  3270  2840     0
6D  01011000812017 2781  1610  1540  1480  1400  1330  1270  1220  1170
6D  01011000812017 2781  1120  1080  1030  1000   970   950   920   890
6D  01011000812017 2781   860   840   810   790   770   750   730   710
6D  01011000412025 2781   695   680   670   655     0     0     0     0
6D  01011000812017 3781   640   630   620   610   600   590   580   575
6D  01011000812017 3781   565   555   550   545   540   535   530   525
6D  01011000812017 3781   520   515   510   510   505   500   505   510
6D  01011000712025 3781   520   545   580   625   670   740   790     0
6D  01011000812017 4781   850   900   920   905   890   875   860   850
6D  01011000812017 4781   830   825   860   940  1050  1200  1350  1550
6D  01011000812017 4781  1800  2100  2450  2850  3400  4000  4600  5400
6D  01011000612025 4781  6300  7500  8520 10200 11000 11700     0     0
6D  01011000812017 5781 10600  9150  8220  8110  8530  9600 11000 12100
6D  01011000812017 5781 14000 16700 16400 14900 13300 12000 10800  9150
6D  01011000812017 5781  7500  6490  5810  5320  5170  5540  4760  4120
6D  01011000712025 5781  3670  3290  2940  2630  2420  2220  2040     0
6D  01010000812017 2791  1400  1900  2300  1950  1640  1420  1250  1110
6D  01010000812017 2791  1040   940   860   800   740   695   640   610
6D  01010000812017 2791   580   545   525   505   490   470   450   430
6D  01010000412025 2791   420   410   400   385     0     0     0     0
6D  01010000812017 3791   380   370   365   360   375   490   660  1200
6D  01010000812017 3791  2500  4700  5000  4500  4000  3650  3300  3100
```

St. John River at 9-Mile, 1978

St. John River at Dickey, 1978

St. John River Allagash River near Allagash, 1978 at 9-Mile, 1979

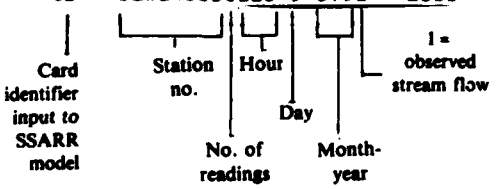

```
6D  01010000812017 3791   2900   2700   2550   2400   2330   2250   2200   2600
6D  01010000712025 3791   4500   9000  13000  15300  14000  12100  10400      0
6D  01010000812O 1 4791  10100  10300   9380   8470   7510   6350   5100   4420
6D  01010000812O 9 4791   3870   3470   3070   2860   2730   3300   4570   5490
6D  01010000812017 4791   6390   6560   6720   6550   7610   9750  10300  12400
6D  01010000612025 4791  14600  17400  23600  31500  34200  30300      0      0
6D  01010000812O 1 5791  23800  19100  15400  12700  10900   9030   7160   5760
6D  01010000812O 9 5791   4980   5180   5000   4120   3410   3080   2700   2320
6D  01010000812017 5791   2020   1770   1520   1300   1130   1220   1660   1460
6D  01010000712025 5791   1250   3020   7260   7100   6600   7650  10900      0
6D  01010500812O 1 2791   3050   3700   4490   4250   3700   3250   2850   2520
6D  01010500812O 9 2791   2270   2100   1990   1850   1750   1680   1580   1490
6D  01010500812017 2791   1400   1300   1250   1200   1150   1100   1040   1000
6D  01010500412025 2791    960    920    880    850      0      0      0      0
6D  01010500812O 1 3791    810    775    760    745    745    860   1180   1650
6D  01010500812O 9 3791   4100   8500  10000   9500   9000   8200   7500   7000
6D  01010500812017 3791   6500   5900   5600   5100   4800   4500   4500   6200
6D  01010540712025 3791  12000  21000  29300  32000  31200  25500  21300      0
6D  01010500812O 1 4791  19500  19500  18600  16500  15100  13000  10500   9230
6D  01010500812O 9 4791   8330   7570   6520   6310   5720   6310   8290  10300
6D  01010500812017 4791  11800  12400  12500  12400  13500  17000  19200  22700
6D  01010500612025 4791  28400  34700  48000  68200  86800  80900      0      0
6D  01010500812O 1 5791  60300  50030  38800  29900  24900  20600  16300  13100
6D  01010500812O 9 5791  11300  11500  11800   9990   8200   7360   6750   5840
6D  01010500812017 5791   5140   4430   3830   3330   2920   2720   2970   3350
6D  01010500712025 5791   2990   3380  10100  13900  13900  17000  23700      0
6D  01011000812O 1 2791   1820   1900   1900   1880   1790   1700   1630   1570
6D  01011000812O 9 2791   1500   1400   1350   1300   1250   1200   1150   1110
6D  01011000812017 2791   1080   1020   1000    960    940    910    880    840
6D  01011000412025 2791    820    795    775    750      0      0      0      0
6D  01011000812O 1 3791    740    720    705    700    710    760    945   1350
6D  01011000812O 9 3791   2380   3400   3950   3900   3750   3480   3200   3000
6D  01011000812017 3791   2850   2630   2500   2400   2300   2210   2280   2480
6D  01011000712025 3791   3250   5450  12000  11600   9980   8600   7690      0
6D  01011000812O 1 4791   7330   6940   6570   6170   5870   5540   5190   4780
6D  01011000812O 9 4791   4500   4310   3990   3760   3570   3750   4080   4230
6D  01011000612017 4791   4480   4460   4430   4290   4480   5020   5320   6230
6D  01011000612025 4791   7240   9130  14100  20200  26700  25800      0      0
6D  01011000812O 1 5791  21500  16600  12700  10200   8200   6800   5800   5200
6D  01011000812O 9 5791   4750   4800   4900   4700   4200   3590   3050   2650
6D  01011000812017 5791   2300   2000   1800   1650   1550   1500   1550   1640
6D  01011000712025 5791   1660   1650   2000   3400   4500   5600   8000      0
6D  01010000812O 1 2801    285    275    265    255    245    235    230    220
6D  01010000812O 9 2801    210    205    195    190    180    175    170    165
6D  01010000812017 2801    160    155    150    145    140    140    135    130
6D  01010000512025 2801    130    125    125    125    125      0      0      0
6D  01010000812O 1 3801    120    120    120    120    120    125    125    130
6D  01010000812O 9 3801    130    130    135    140    140    145    150    155
6D  01010000812017 3801    160    170    185    205    230    260    295    340
6D  01010000712025 3801    380    430    480    530    560    590    650      0
6D  01010000812O 1 4801    700    800    960   1300   1850   1860   1800   1750
6D  01010000812O 9 4801   1800   1950   2500   4500   6600  10400  14400  15200
6D  01010000812017 4801  11600   8740   6220   5190   5430   5020   4370   4250
6D  01010000612025 4801   4880   5490   6720   8660   8120   6950      0      0
6D  01010000812O 1 5801   6690   6180   5380   4560   3850   3260   2920   3170
6D  01010000812O 9 5801   3440   3380   3100   2770   2560   2570   2910   2820
6D  01010000812017 5801   2480   2160   2610   4170   3630   2870   2350   2020
6D  01010000712025 5801   1750   1520   1340   1220   1120   1010    885      0
```

St. John River at 9-Mile, 1980 | Allagash River near Allagash, 1979 | St. John River at Dickey, 1979

Card identifier input to SSARR model

Station no.

No. of readings

Hour

Day

Month-year

1 = observed stream flow

```
6D  01010500812012 1 2801   630   610   580   560   540   525   500   490
6D  01010500812012 9 2801   470   460   450   430   420   410   395   385
6D  01010500812017 2801     380   365   355   345   340   335   330   325
6D  01010500512025 2801     320   315   310   310   305     0     0     0
6D  01010500812012 1 3801   300   300   295   300   300   305   305   310
6D  01010500812012 9 3801   310   315   320   325   330   345   355   370
6D  01010500812017 3801     385   425   470   525   600   680   760   850
6D  01010500712025 3801     950  1000  1100  1200  1250  1300  1400     0
6D  01010500812012 1 4801  1500  1700  1900  2150  2750  3600  3750  3700
6D  01010500812012 9 4801  3700  4050  5300  9000 14000 22500 29400 33700
6D  01010500812017 4801    26700 19100 13800 11000 10600 10100  8870  8440
6D  01010500612025 4801     9760 11300 12800 15900 16200 14200     0     0
6D  01010500812012 1 5801  12700 12000 10700  9140  7730  6560  5870  6350
6D  01010500812012 9 5801   7190  6900  6230  5590  5050  5200  5940  5950
6D  01010500812017 5801     5200  4600  4360  6060  7070  6140  5090  4240
6D  01010500712025 5801     3660  3190  2840  2590  2380  2190  2020     0
6D  01011000812012 1 2801   380   360   375   370   365   365   360   360
6D  01011000812012 9 2801   355   350   350   350   345   345   340   340
6D  01011000812017 2801     340   335   330   330   325   325   325   320
6D  01011000512025 2801     320   320   315   315   310     0     0     0
6D  01011000812012 1 3801   310   305   305   300   300   305   305   305
6D  01011000812012 9 3801   305   305   310   310   310   310   310   315
6D  01011000812017 3801     315   320   325   330   335   345   360   385
6D  01011000712025 3801     410   440   475   520   570   630   690     0
6D  01011000812012 1 4801   760   850   950  1020  1120  1200  1300  1450
6D  01011000812012 9 4801  1700  2100  2700  3700  5000  6300  7200  8610
6D  01011000812017 4801    6860  5740  4780  4200  4320  3630  3430  3480
6D  01011000612025 4801    3700  3890  4280  4520  4290  4070     0     0
6D  01011000812012 1 5801  3910  3790  3610  3390  3130  2910  2790  2990
6D  01011000812012 9 5801  3250  3280  3040  2770  2590  2770  3130  2860
6D  01011000812017 5801    2550  2350  2500  2720  2650  2530  2380  2230
6D  01011000712025 5801    2030  1830  1730  1610  1490  1410  1340     0
```

Allagash River near Allagash, 1980 — St. John River at Dickey, 1980

Card identifier input to SSARR model

Station no.

Hour

Day

Month-year

No. of readings

1 = observed stream flow

## Wind Speed

```
4D          1 120 1 2798  34  34  47  34  58  69  34  22  58  34  47  11  34  58
4D          1 12015 2798  34  47  58  34  22  22  00  22  34  34  22  11  11
4D          1 120 1 3798  11  22  22  11  11  22  00  22  11  11  22  69  22  47
4D          1 12015 3798  58  22  34  34  22  34  11  11  11  34  22  34  69  22
4D          1312029 3798  11  22  11
4D          1 120 1 4798  34  22  11  22  22  11  58  22  00  34  69  58  34  22
4D          1 12015 4798  22  22  22  22  22  22  11  00  22  22  22  34  47  47
4D          1212029 4798  00  11
4D          1 120 1 5798  58  47  22  11  58 114  81  22  47  69  22  69  34  00
4D          1 12015 5798  47  11  22  45  45  45  45  67  45  22  67  67  45  22
4D          1312029 5798  45  45  22
4D          1 120 1 2808  47  34  34  22  34  11  11  11  11  22  11  11  47  47
4D          1 12015 2808  58  00  58  69  92  11  34  11  22  22  34  34  11  22
4D          1112029 2808  47
4D          1 120 1 3808  58  22  11  34  22  47  34  11  11  22  47  69  11  34
4D          1 12015 3808  58  47  22  34  47  11  34  58  34  11  22  22  22  22
4D          1312029 3808  22  22  22
4D          1 120 1 4808  11  22  22  34  22  22  69  47  34  58  11  47  34
4D          1 12015 4808          47  47  34  47  58  69  58  47  11  22  22  00
4D          1212029 4808  22  00
4D          1 120 1 5808  22  45  45  67  67  45  67  45  22  45  67  90  45  22
4D          1 12015 5808  22  47  22  47  34  22  58  47  22  34  34  47  47  22
4D          1312029 5808  34  22  22
```

- Card identifier input to SSARR model
- Station no.
- No. of readings/card default = 14
- Hour
- Day
- Month
- Year
- Code for wind speed (m/h xxx.x)
- Wind speed (m/h)

## Rain Fall

```
4P          14120 7 2783    622120 9     3212014     8912027     95
4P          15120 6 3783     9012014    47612019     5112020     9012021    546
4P          1412022 3783    52412023    59112026    26012027    1556
4P          1512011 4783    23512020    59712021    32412023    17112024   152
4P          15120 1 5783     44120 8     89120 9    28612021    43812028   108
4P          1212029 5783     8312031    235
4P          15120 1 2793    260120 2    121120 3     1312021     1312022    70
4P          1412024 2793     1912026    16512027    24112028    70
4P          15120 2 3793     38120 6    267120 7     6312011     1312012    25
4P          1512013 3793    11412025    22912026    36812027    1312029    19
4P          1112031 3793    190
4P          15120 1 4793     13120 2    140120 3    102120 5    190120 6    43
4P          15120 7 4793     46120 8     13120 9     7612010    40012011    19
4P          1512023 4793     1912026     0612027     7012028    37512029   292
4P          1112030 4793     13
4P          15120 1 5793    546120 2     13120 4     76120 5     3212013    25
4P          1512021 5793     5112025    42512026    26712027    1312028    292
4P          1312029 5793    36812030    56512031    70
4P          15120 5 2803     3212013     0612016    17812022    3812023    63
4P          1212024 2803     1912025    32
4P          15120 5 3803     63120 6    51120 7     06120 9    20312010    13
4P          1512011 3803    25412012     7612014    25412015    17812017   102
4P          1212018 3803    61012026    127
4P          15120 4 4803     6312010    25412011     3812013     7612014    25
4P          1512015 4803    30412020    14012022     3812023     6312024    13
4P          1212026 4803    19012027     63
4P          15120 7 5803    133120 8    133120 9     6312013    15912014   152
4P          1312018 5803     6312018     6312019    15912031    32
```

Card identifier input to SSARR model

Station no.

No. of readings/ card

Hour

Day

Month

Year

Code for rain (in., xx.xx)

1st reading of rain — Hour — Day

2nd reading of rain — Hour — Day

3rd reading of rain — Hour — Day

4th reading of rain — Hour — Day

5th reading of rain

## Air Temperature

```
4D          1 12( 1 2784  32 -40 -94 -58 -58 -31 158  86  59 -67 -31 122  68 -22
4D          1 12015 2784 248 131  86 185  68  50 104 194 167 158 122 266 257 140
4D          1 120 1 3784 122 176  59  95  50 122 158 149 140 158 158 266 158 248
4D          1 12015 3784 302 104  32  59 158 212 149 262 194 176 212 176 284 336
4D          1312029 3784 329 266 266  0   0   0   0   0   0   0   0   0   0   0
4D          1 120 1 4784 176 239 140 176 320 320 284 320 338 356 356 356 374 374
4D          1 12015 4784 347 374 347 363 337 411 344 337 352 363 374 374 392 392
4D          1212029 4784 392 292  0   0   0   0   0   0   0   0   0   0   0   0
4D          1 120 1 5784 320 401 392 383 410 410 428 464 410 500 482 509 516 509
4D          1 12015 5784 572 545 590 545 518 473 464 455 473 486 566 586 549 650
4D          1312029 5784 643 636 596  0   0   0   0   0   0   0   0   0   0   0
4D          1 120 1 2794 262 214 135 176  52  63  77 146 -63-149-140-142-130-103
4D          1 12015 2794-121-110-140 -85 -25 103 275 169 164 320 175 135 211 333
4D          1 120 1 3794 220 223 299 362 405 423 358 340 326 257 308 124 774 333
4D          1 12015 3794 149  70 103 283 310 351 409 421 463 446 380 353 221 225
4D          1312029 3794 297 362 356
4D          1 120 1 4794 306 301 364 360 301 324 290 225 243 324 324 351 416 403
4D          1 12015 4794 353 515 335 311 385 445 515 506 423 425 443 576 526 562
4D          1212029 4794 515 513
4D          1 120 1 5794 513 428 500 455 399 399 441 497 655 486 490 553 590 556
4D          1 12015 5794 610 596 704 576 652 635 655 488 526 569 493 463 576 529
4D          1312029 5794 540 560 569
4D          1 120 1 2804  18  38 178  47  95  88  18  76  16 -23  26  97  31  77
4D          1 12015 2804 -40  32  45  74 232 223 227  11 101  72 145 -56 -13  31
4D          1112029 2804 -25
4D          1 120 1 3804   7 -20  59 106 180 153 149  85 194 135 218  34  32 166
4D          1 12015 3804 135  88  90 245 250 124 230 295 360 279 326 346 333 300
4D          1312029 3804 382 326 290
4D          1 120 1 4804 275 346 371 360 362 299 214 355 446 446 391 387 432 401
4D          1 12015 4804 470 401 301 335 310 365 387 245 346 391 466 445 416 391
4D          1212029 4804 416 472
4D          1 120 1 5804 475 526 500 481 351 410 475 401 436 436 443 605 495 520
4D          1 12015 5804 430 475 466 515 605 481 517 590 490 486 500 455 452 461
4D          1312029 5804 446 486 590
```

- Card identifier input to SSARR model
- Station no.
- No. of readings/card, default = 14
- Hour
- Day
- Month
- Year
- Code for air temperature (°F, xxx.x)
- Air temperature readings

A facsimile catalog card in Library of Congress MARC format is reproduced below.

Merry, Carolyn J.

Use of Landsat digital data for snow cover mapping in the Upper Saint John River Basin, Maine / Carolyn J. Merry and Michael S. Miller. Hanover, N.H.: U.S. Army Cold Regions Research and Engineering Laboratory; Springfield, Va.: available from National Technical Information Service, 1987.

v, 74 p., illus.; 28 cm. (CRREL Report 87-8.)

Bibliography: p. 52.

1. Hydrolgic modeling. 2. Landsat. 3. Remote sensing. 4. Runoff. 5. Snow cover. 6. Snow water equivalent. I. Miller, Michael S. II. United States. Army. Corps of Engineers. III. Cold Regions Research and Engineering Laboratory, Hanover, N.H. IV. Series: CRREL Report 87-8.

END

9-87

DTIC